Microwave Laboratory

W. W. HANSEN LABORATORIES OF PHYSICS

STANFORD UNIVERSITY · STANFORD, CALIFORNIA

Reproduced by the
CLEARINGHOUSE
for Federal Scientific & Technical
Information Springfield Va. 22151

STUDIES OF MICROWAVE SHEAR WAVES IN SOLIDS

by

E. G. H. Lean

M. L. Report No. 1543

Internal Memorandum

Contract AF 49(638)-1429

and

NASA Grant NGR-05-020-165

May 1967

DDC
NOV 27 1968
A

Microwave Laboratory
W. W. Hansen Laboratories of Physics
Stanford University
Stanford, California

ERRATA SHEET

for

STUDIES OF MICROWAVE SHEAR WAVES IN SOLIDS

by

E. G. H. Lean

M. L. Report No. 1543

May 1967

Page	
4	Line 4, last word, change 200 to read "12"
43	Table II, conversion efficiencies column, measured value, change the 39 to read "30" (appears twice)
106	Eighth line from bottom, add right parenthesis to read $(p_{11}-p_{12})/2$
111	The expression between Eqs. (5.4) and (5.5), change the $\frac{W}{s}$ to "$\frac{W}{2}$"
115	Eq. (5.10), change n^o to n_0
115	Three lines below Eq. (5.10), change n^o to n_0
119	Eq. (5.13), add "A_1" to the coefficient to read $-\epsilon_1\epsilon_3 p_{55} S_0 A_1$
126	Expression at top of page, RHS, change "0.4" to read "0.3"
126	Fourth line of text, change "$2\Delta f$ = 625 Mc which is slightly larger" to read "$2\Delta f$ = 470 which is slightly smaller".

ABSTRACT

Due to the slower velocities and the transverse wave nature, microwave shear waves have interesting theoretical properties and important practical application. One of the difficulties for shear wave studies at microwave frequencies has been the problem of efficient generation of microwave shear waves. Because of the polarization effect of shear waves, the parametric interaction of light and microwave shear waves in both isotropic and anisotropic crystals provides potential for acoustic probing and device applications. Theoretical and experimental investigation of microwave shear waves in solids were conducted with emphasis on the efficient generation of microwave shear waves and on the theory and applications of the parametric interaction of microwave shear waves and light.

For the generation of efficient microwave shear waves two schemes were used: mode conversion in a YAG converter, and surface excitation from lithium niobate ($LiNbO_3$) rods and thin disk transducers. A parallelpiped YAG mode converter was used to demonstrate the scheme of efficient microwave shear wave generation, through which virtually the full efficiency available for longitudinal wave generation can be applied to shear waves. The generation and propagation of microwave acoustic waves in $LiNbO_3$ crystals, where the large piezoelectric effect has to be included, was studied theoretically and experimentally. Experimental results of the velocities, the direction of particle displacements and electromechanical coupling constants for each of the propagating modes along crystal axes were in good agreement with the calculated values based on published constants. The typical conversion loss from electromagnetic to acoustic energies for shear waves in an x-cut $LiNbO_3$ disk transducer is 10 dB at 1 GHz. These efficient shear wave transducers make possible the study of the interaction of light and microwave shear waves in solids.

In microwave frequencies, the interaction of light and microwave shear waves is in Bragg diffraction region. The theory of Bragg diffraction of light from shear waves predicts two important unique features.

The first is a 90° rotation of the polarization of the diffracted light with respect to that of the incident light. The second is that the intensity of the diffracted light is a function of the polarization of the acoustic waves. Utilizing the unique characteristics of shear wave diffraction, we have used a laser as an optical probe to map the energy distribution of shear waves, to measure the attenuation, to estimate the mode conversion efficiency of a YAG mode converter, and to determine the reflection and transmission coefficients of shear wave bonds. We have also demonstrated the second feature of shear wave diffraction in measuring quantitatively the acoustic birefringence in a [110] oriented YAG rod. This provided a technique to determine experimentally the orientation and ellipticity of shear waves generated from experimental transducers.

There are two types of Bragg diffraction of light by acoustic waves in optically anisotropic media. The first type is identical with that in optically isotropic crystals, when the polarizations of the diffracted and the incident lights are the same. The second type requires an extra phase matching condition for the lights in the optically anisotropic media when the polarization of the diffracted light differs from that of the incident light. Based on the second type of diffraction by a shear wave column of finite width in sapphire, we have demonstrated a scheme of continuous deflection of an optical beam through an angle of 4° by tuning the shear wave frequencies from 1.2 to 1.8 GHz. The system should be capable of resolving 1000 diffracted spots. The possible extension to two-dimensional deflection schemes will also be included.

ACKNOWLEDGEMENTS

I would like to express my deepest gratitude to Dr. H. J. Shaw for his guidance, stimulation and encouragement throughout the course of this study. I am also deeply grateful to Professor C. F. Quate for many helpful discussions, especially in the continuous beam deflection experiment which he initially suggested; to Dr. D. K. Winslow for his invaluable suggestions about many problems, both conceptual and experimental, which I encountered in this study; and to Professor M. Chodorow for his comments regarding the manuscript.

Special thanks go to W. R. Smith for his assistance in the theoretical and computer calculation on the study of shear wave bonds and his comments regarding the manuscript of Chapter II; and to H. R. Zapp for his critical reading of the manuscript.

The skillful assistance of R. F. Griffin, who cut, polished, and oriented the crystals, and A. D. Moody who built much of the experimental apparatus, and L. E. Yingst, W. O. Heintzen who designed and built the electronic equipment required for some of the experiments, and D. J. Walsh who helped in $LiNbO_3$ crystal poling is gratefully acknowledged.

I also want to express my appreciation to A. S. Braun for his useful editorial comments on the manuscript and his supervision on its speedy publication; to Mmes. I. L. Williams, P. R. Brady, S. Wise, and B. H. Dutton for typing the manuscript and to Messrs. A. Vacek and N. B. Bettini for drawing the figures.

Finally, I would like to thank my wife, Alice, for her understanding, her patience and her encouragement.

TABLE OF CONTENTS

LIST OF FIGURES

BLANK PAGE

CHAPTER I

INTRODUCTION

Physical acoustics at microwave frequencies have been shown to have cumulative interactions with carrier waves in semiconductors,[1] with spin waves in ferrimagnetic materials[2] and with light waves in transparent crystals.[3] Microwave acoustics include both longitudinal waves and shear waves. Longitudinal waves, also called compressive waves, have the particle motion along the direction of propagation; shear waves, also called transverse waves, have the particle motion normal to the direction of propagation. Beside these pure longitudinal or shear waves which propagate along certain pure mode axes in the crystals, there are quasi-longitudinal or quasi-shear waves where the particle motions are no longer parallel or normal to the directions of propagation. In this study we are concerned with the studies of microwave shear waves in solids. The emphasis will be on the generation of microwave shear waves, on the theory of Bragg diffraction of light by microwave shear waves, and on the applications of the shear wave diffraction on acoustic probing and laser beam deflection techniques.

The advantages of shear waves over longitudinal waves come from the slower velocities and the transverse-wave nature of shear waves. For example, shear waves are preferable for delay line applications.[4] The polarization effect of shear waves provides potential device applications.

Microwave shear waves, in spite of their interesting theoretical properties and important practical applications, have not received much attention. One of the difficulties of studying shear waves at microwave frequencies has been the problem of efficient generation. In Chapter II, several methods of generating efficient microwave shear waves will be discussed. The recently developed crystal in class (3m), lithium niobate ($LiNbO_3$) single domain crystals, has been found to have unusually large

piezoelectric constants, especially for shear wave generation.[5] Theoretical calculations of the velocities and the electromechanical coupling constants for three acoustic modes generated in the surfaces of $LiNbO_3$ crystals have been carried out (Section 2.3). Experimental results are shown to confirm the theoretical predictions. An interesting integral delay line application using $LiNbO_3$ resonators will be given in Section 2.4. The low conversion loss of the thin disk transducers (Section 2.5) is one reason why experiments of shear wave diffraction of light are possible. In Section 2.6 a scheme of efficient microwave shear wave generation by a YAG mode converter will be discussed.

In Chapter III the theory of Bragg diffraction of light by microwave shear waves will be given. Light diffraction by acoustic waves has been studied extensively since Brillouin first predicted the effect in 1922.[6] This phenomenon, Brillouin scattering, was originally used to determine the elastic constants[7] and to study thermal phonon distributions[8] in various materials. The early work was done at low frequencies where Raman-Nath type[9] of scattering dominates. In the range of acoustic wavelengths at microwave frequencies, the Brillouin scattering experiments are also called Bragg diffraction of light by microwave acoustic waves because the situation is similar to the Bragg diffraction of x-rays by crystal lattices. The criterion of Bragg diffraction has been given by Willard.[10] The condition for Bragg diffraction is $\lambda W > \Lambda^2$ (where λ is the optical wavelength, W is the acoustic beam width and Λ is the acoustic wavelength). Acoustic Bragg diffraction of light is a parametric interaction process.[11] The basic requirements are the conservation of energies (the frequencies) and the conservation of momenta (the wave vectors). Bragg diffraction of light by microwave longitudinal waves in solids has been studied extensively by Quate, et al.[3] A comprehensive review of the principles and history of light diffraction by acoustic waves is given in their paper.

In recent years with the invention of lasers as intense coherent light sources and the development of experimental techniques for generating coherent acoustic waves at microwave frequencies, Brillouin scattering has found application in modulating,[12] frequency shifting,[13]

and deflecting laser beams,[14] and in studying the acoustic and photoelastic properties of materials.[15,16] Most of the work has, so far, utilized longitudinal waves. In Chapter III the theory of shear wave diffraction in cubic crystals predicts two unique features. The first is a 90° rotation of the polarization of the diffracted light with respect to that of the incident light. The second is that the intensity of the diffracted light is a function of the polarization of the acoustic waves.

Utilizing the unique characteristics of shear wave diffraction, we have used a laser as an optical probe to map the energy distribution of shear waves, to measure the attenuation of shear waves, and to determine the reflection and transmission coefficients of shear wave bonds. The 90° rotation in the polarization of the diffracted light has experimental advantages in that the diffracted light can be easily separated from the transmitted light and from the light scattered off the crystal surfaces, thereby substantially increasing the signal-to-noise ratio. We have also demonstrated the second feature of shear wave diffraction in measuring quantitatively the acoustic birefringence in a [110] oriented YAG rod. This provided a technique to determine experimentally the orientation and ellipticity of shear waves generated from experimental transducers. The experimental results are shown in Chapter IV.

In Chapter V, a scheme of continuous deflection of laser beams based on the shear wave deflection in optically anisotropic media will be discussed and demonstrated. There are two types of Bragg diffraction of light by acoustic waves in optically anisotropic media. The first type is identical with that in optically isotropic crystals, when the polarizations of the diffracted and the incident lights are the same. The second type requires an extra phase matching condition for the lights in the optically anisotropic media when the polarization of the diffracted light differs from that of the incident light. Dixon[17] has reported on this type of diffraction in both quartz and sapphire. Based on the second type of diffraction by a shear wave column of finite width in sapphire, we have demonstrated a scheme of continuous deflection of an optical beam through an angle of 4° by tuning the shear wave frequencies

from 1.2 to 1.8 GHz. The system should be capable of resolving 1000 diffracted spots. Compared with the corresponding devices using acoustic Bragg diffracted in isotropic crystals, it is found that the present scheme has improved the bandwidth capacity by a factor greater than 200. The possible extension to two-dimensional deflection schemes will also be included in Chapter V.

CHAPTER II

GENERATION OF MICROWAVE SHEAR WAVES IN SOLIDS

2.1 INTRODUCTION

In all devices and applications of microwave acoustic waves at present, one of the largest practical difficulties is the design and fabrication of efficient transducers to convert microwave electromagnetic energy into microwave acoustic energy and vice versa. For longitudinal acoustic wave transducers, part of the difficulty has been solved by recent extensive studies of vacuum bonding and thin film deposition techniques. A zinc oxide (ZnO) disk transducer vacuum bonded by indium to a delay medium[18] can be excited in odd harmonics in a re-entrant cavity and have a conversion loss from electromagnetic energy to acoustic energy below 10 dB. Also thin film techniques of depositing single layer or multiple layers of cadmium sulphide (CdS)[19] or ZnO film[20] have been used satisfactorily in fabricating efficient wide band transducers for generating microwave longitudinal waves.

For transverse aves the difficulty of fabricating efficient transducers has always been severe. In this chapter we are concerned with schemes of fabricating efficient transverse acoustic wave transducers at microwave frequencies and the measurements and calculations of the conversion efficiencies from electromagnetic to acoustic energies of these transducers.

The recently developed piezoelectric crystals of class (3m) such as lithium niobate and lithium tantalate have been found to have unusually large piezoelectric constants.[21] These materials are very important for transducer applications. A theory for the generation and propagation of the acoustic waves along the crystal axes in these crystals is given in Section 2.2. The usual assumption for small piezoelectric effect as in quartz crystals is no longer valid for $LiNbO_3$ or $LiTaO_3$ crystals which

have larger piezoelectric constants. The effect of the large piezoelectric coupling on the velocities and the excitation are included in the theory. The expressions for the electromechanical coupling constants and the conversion efficiencies for the acoustic waves generated in the $LiNbO_3$ crystal will be derived. The numerical values calculated on the published constants[21] will be given to check the measured values. In Section 2.4 an integral delay line application of single surface excitation in $LiNbO_3$ resonators will be discussed. Preliminary measured values for the conversion efficiencies will be given to compare with the predicted values. In Section 2.5 experimental results on conversion efficiencies for the acoustic waves generated in $LiNbO_3$ disk transducer will be given. Finally in Section 2.6 a method of efficient conversion from longitudinal acoustic waves to shear waves in YAG by surface conversion at an inclined surface will be included. Using this process, existing efficient longitudinal wave transducers are applicable to shear wave generation.

2.2 GENERATION AND PROPAGATION OF MICROWAVE ACOUSTIC WAVES IN PIEZOELECTRIC CRYSTALS

Piezoelectric crystals and ceramics are among the principal generators and detectors of microwave acoustic waves. Jacobsen[22] has summarized the piezoelectric effects and examined the generation, detection and propagation of microwave acoustic waves in piezoelectric media, especially in quartz where the piezoelectric effect is small. In the transducer application of the piezoelectric crystals at microwave frequencies, the crystal is usually operating in a form of thin films,[19,20] thin plates[23] or single surfaces.[24] Tiersten[25] has rigorously calculated resonant frequencies of the steady-state thickness vibrations of a homogeneous anisotropic infinite plate with infinite plated electrodes on both surfaces. No restriction on the relative magnitudes of the piezoelectric, elastic, or dielectric constants is imposed in Tiersten's analysis. We are interested in the generation and propagation of the microwave acoustic waves in materials with high piezoelectric constants such as recently developed $LiNbO_3$ where the usual weak piezoelectricity assumption[26] may not be valid. In the following analysis, Tiersten's approach will be

extended to solve questions concerning the generation and propagation of acoustic waves in media with large piezoelectric constants.

The linear piezoelectric relations which describe the elastic and electric properties in a piezoelectric crystal are

$$T_{ij} = C^{E}_{ijgh} S_{gh} - e_{pij} E_p \tag{2.1a}$$

$$D_q = e_{qgh} S_{gh} + \epsilon^{S}_{qp} E_p \quad , \tag{2.1b}$$

where C^{E}_{ijgh} is the stiffness tensor component (elastic constants) for constant electric field, e_{pij} is the component of the piezoelectric stress tensor, ϵ^{S}_{qp} is the dielectric permittivity tensor components for constant strain condition and S_{gh} is the component of the strain tensor. In terms of particle displacement U_g, S_{gh} is defined as

$$S_{gh} = \frac{1}{2}\left(\frac{\partial U_g}{\partial x_h} + \frac{\partial U_h}{\partial x_g}\right) \quad . \tag{2.2}$$

The indices in (2.1) refer to an orthogonal coordinate system, the axes of which may be oriented arbitrarily relative to the crystal axes. The tensor index sum rule is implicit in writing Eq. (2.1) and $i, j, g, h, q, p = 1, 2, 3$. It should be noted that E_p is the total electric field in the piezoelectric medium including the external applied field $(E_a)_p$ and the internal induced field, $(E_{ind})_p$, while S_{gh} is the total strain in the crystal.

Since we are concerned with the elastic waves propagating in the medium, the system of equations governing the behavior of the piezoelectric crystal include the stress equation of motion

$$\frac{\partial T_{ij}}{\partial x_j} = \rho \frac{\partial^2 U_i}{\partial t^2} \tag{2.3}$$

and Maxwell's equations which describe electric fields in the medium, in addition to the linear piezoelectric relations as shown in (2.1).

In terms of matrix notation, in which the double subscript ij (i,j = 1, 2, 3) is represented by single subscript m (m = 1, 2 , ...6) for symmetrical tensors, Eqs. (2.1) become

$$T_m = C^E_{mn} S_n - e_{mp} E_p \qquad (2.4a)$$

$$D_q = e_{qn} S_n + \epsilon^S_{qp} E_p \qquad (2.4b)$$

$$(m,n = 1, 2, 3, \ldots 6)$$

$$(p, q = 1, 2, 3)$$

where T_m and S_n are elements of 1×6 matrices [T] and [S] for stress and strain; D_q and E_p are elements of 1×3 matrices $\underset{\sim}{D}$ and $\underset{\sim}{E}$ for electric displacement and electric field; C^E_{mn}, e_{qn} and ϵ^S_{qp} are elements of 6×6 matrices $[C^E]$, [e] and $[\epsilon^S]$ for elastic constant, piezoelectric constant and dielectric constant. The convenient matrix manipulation can then be adopted in the calculation. Eliminating E_p in Eqs. (2.4) we have

$$T_m = C_{mn} S_n - e_{mp} [\epsilon^S]^{-1}_{pq} D_q \quad , \qquad (2.5a)$$

with

$$C_{mn} = C^E_{mn} + e_{mp} [\epsilon^S]^{-1}_{pq} e_{qn} \qquad (2.5b)$$

$$(m,n = 1, 2, \ldots 6)$$

$$(p,q = 1, 2, 3)$$

where $[\epsilon^S]^{-1}$ is the inverse of matrix $[\epsilon^S]$. The notation $[A]^{-1}_{pq}$ denotes the scalar pq element of the tensor $[A]^{-1}$.

Now consider a special case where plane waves propagate along one of the crystal axes, for example the x-axis which coincides with the x_1 coordinate. There is no variation in the transverse plane under the plane wave assumption. The derivatives with respect to x_2 and x_3 are zero so that S_{gh} reduces to

$$S_{g1} = \frac{\partial U_g}{\partial x_1} \quad .$$

Equations (2.1) become

$$T_{i1} = C^E_{i1g1} \frac{\partial U_g}{\partial x_1} - e_{pi1} E_p \tag{2.6a}$$

$$D_q = e_{qg1} \frac{\partial U_g}{\partial x_1} + \epsilon^S_{qp} E_p \quad . \tag{2.6b}$$

Equations (2.4) remain valid for the plane waves propagating along the x_1-axis by letting $m,n = 1, 6, 5$ and $p,q = 1, 2, 3$.

By rewriting Eqs. (2.5) for the special case $(m,n = 1, 6, 5)$ in terms of tensor notation, we have

$$T_{i1} = C_{i1g1} \frac{\partial U_g}{\partial x_1} - e_{i1p} [\epsilon^S]^{-1}_{pq} D_q \tag{2.7a}$$

with

$$C_{i1g1} = C^E_{i1g1} + e_{i1p} [\epsilon^S]^{-1}_{pq} e_{qg1} \quad . \tag{2.7b}$$

Combining Eq. (2.7a) with the stress equation of motion, we obtain a wave equation for the particle displacement U_i propagating along the x_1-axis ,

$$\rho \frac{\partial^2 U_i}{\partial t^2} - C_{ilgl} \frac{\partial^2 U_g}{\partial x_1^2} = - \frac{\partial}{\partial x_l} [e_{ilp} (\epsilon^S)^{-1}_{pq} D_q] \quad . \quad (2.8)$$

The term in the right hand side of Eq. (2.8) is recognized as the source term for the wave equation.

In general, the electric displacement D_q in a piezoelectric medium can be written as

$$D_q = e_{qgl} S_{gl} + \epsilon^S_{qp} (E_a + E_{ind})_p \quad , \quad (2.9)$$

where E_a is the applied field and E_{ind} is the internal induced field. Let

$$D_q = (D_a)_q + (D_{ind})_q \quad , \quad (2.10a)$$

where

$$(D_a)_q = \epsilon^S_{qp} (E_a)_p \quad (2.10b)$$

is the electric displacement due to the applied electric fields in a dielectric medium with no piezoelectric effect;

$$(D_{ind})_q = e_{qgl} S_{gl} + \epsilon^S_{qp} (E_{ind})_p \quad (2.10c)$$

is the induced displacement due to the strain waves S_{gh} and the induced electric fields E_{ind} . Using Eq. (2.10a), the driving term in Eq. (2.8) becomes

$$-\frac{\partial}{\partial x_1}\left[e_{ilp}(E_a)_p + e_{ilp}(\epsilon^S)^{-1}_{pq}(D_{ind})_q\right] \quad .$$

A schematic variation of the above driving term as a function of x_1 for a half infinite piezoelectric crystal with the surface at $x_1 = 0$ under the influence of spatially constant applied electric field E_a is shown in Fig. 2.1(b). At the surface $x_1 = 0$ there is a delta function due to the discontinuity of the first term $e_{ilp}(E_a)_p$. This is the surface excitation term. Inside the crystal the second term due to $(D_{ind})_q$, which is sinusoidal function with the same acoustic wavelength, also contributes to the generation of the acoustic waves. This is the volume excitation term. In case there is no free charge inside the piezoelectric crystals, we have

$$\nabla \cdot (D_{ind}) = \frac{\partial (D_{ind})_1}{dx_1} = 0 \quad .$$

The volume excitation term comes from

$$\frac{\partial}{\partial x_1}(D_{ind})_2 \quad \text{or} \quad \frac{\partial}{\partial x_1}(D_{ind})_3$$

which need not be zero. Usually the surface excitation term is much stronger than the volume excitation term in the normal piezoelectric media. In the following calculation for the generation of acoustic waves in $LiNbO_3$ crystals, the contribution from the volume excitation

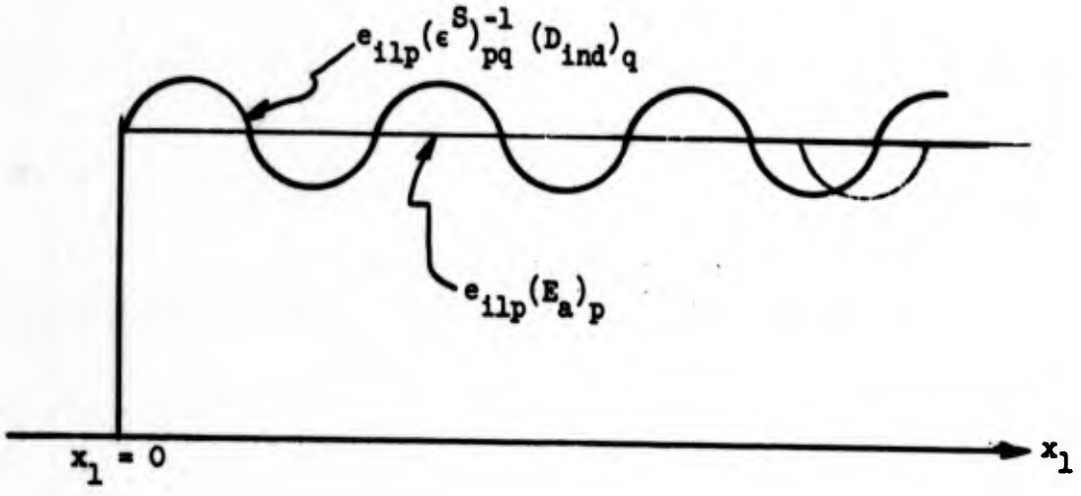

(a) $e_{ilp}(\epsilon^S)^{-1}_{pq}\ D_q$ vs x_1

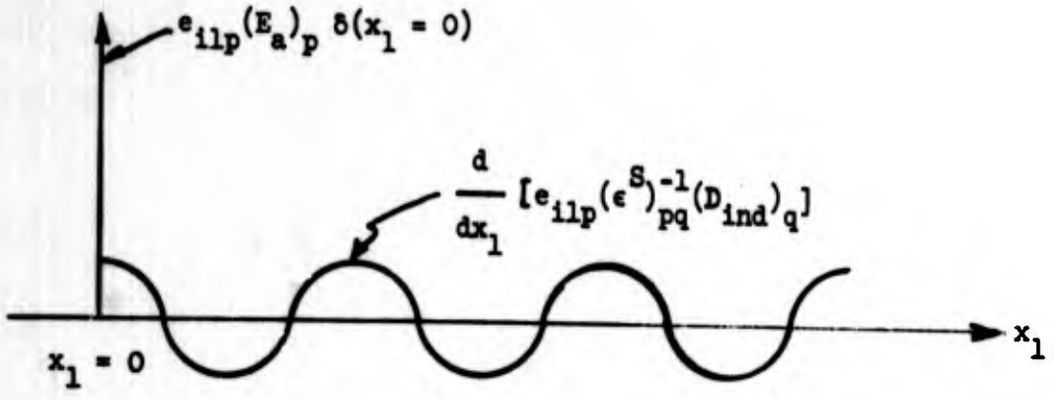

(b) $\frac{d}{dx_1}[e_{ilp}(\epsilon^S)^{-1}_{pq}\ D_q]$ vs x_1

FIG. 2.1--Spatial variation of source term in Eq. (2.8).

term will be neglected, i.e,

$$D_q \cong (D_a)_q \quad . \tag{2.10d}$$

The justification for the assumption will be discussed later.

The solution of the particle displacement U_i for acoustic waves propagating along the x_1-axis can be obtained from the following equation with proper boundary conditions:

$$\rho \frac{\partial^2 U_i}{\partial t^2} - C_{ilgl} \frac{\partial^2 U_g}{\partial x_1^2} = - \frac{\partial}{\partial x_l} [e_{ilp}(E_a)_p] \quad . \tag{2.11}$$

Let the plane wave solution of the particle displacement be

$$U_i = A_i e^{j(\omega_s t - k_s x_1)} \tag{2.12}$$

where ω_s is the frequency and k_s is the wave number. The dispersion relation and the velocities of the waves can be determined by substituting (2.12) into the homogeneous wave equation

$$\rho \frac{\partial^2 U_i}{\partial t^2} - C_{ilgl} \frac{\partial^2 U_g}{\partial x_1^2} = C \quad . \tag{2.13}$$

After the substitution, Eq. (2.13) becomes

$$(C_{ilgl} - C\,\delta_{ig})\, A_i = 0 \tag{2.14}$$

where

$$C = \rho \frac{\omega_s^2}{k_s^2}$$

and δ_{ig} is the Kronecker delta. For a nontrivial solution of (2.14), the determinant of the coefficients of A_i must vanish,

$$|C_{ilgl} - C\,\delta_{ig}| = 0 \quad . \tag{2.15}$$

Equation (2.15) is a cubic equation in C and gives three real positive roots which determine the velocities of the three waves propagating along the x_1-axis .

The determination of the amplitudes of A_i for each wave requires the knowledge of the source terms and the specification of the boundary conditions. The boundary conditions at the surface $x_1 = 0$ include both the mechanical and electrical conditions. Under the same assumption of Eq. (2.10d), the displacement vector at the surface $x_1 = 0$ is given by

$$D_q = \epsilon^S_{qp} (E_a)_p \quad \text{at} \quad x = 0 \tag{2.16}$$

where $(E_a)_p$ are the components of the applied electric fields. Then another boundary condition, that the surface at $x_1 = 0$ is traction free, requires that

$$T_{il} = C_{ilgl} \frac{\partial U_g}{\partial x_1} - e_{ilp}(E_a)_p = 0 \quad , \tag{2.17}$$

from Eqs. (2.7a) and (2.16). It is noted that C_{ilgl} is the stiffened elastic constants given by Eq. (2.7b).

The usual weak piezoelectric assumption in quartz is that the piezoelectric constants e_{pij} are so small that elastic constants in quartz are not stiffened by e_{pij}. The characteristics of the medium are not affected by the small piezoelectricity. The excitation of the acoustic waves in the weak piezoelectric medium is on the surface of the crystal only. The present theory is extended to include the effect of the medium (characterized by the elastic constants) stiffened by the large piezoelectric constants, while the excitation of the acoustic waves is still on the surface of the crystal. The bulk effect of excitation is assumed to be small and negligible. The assumption, that the volume excitation in $LiNbO_3$ crystals can be neglected, will be justified in the next section.

2.3 SURFACE GENERATION OF MICROWAVE ACOUSTIC WAVES IN CRYSTALS OF CLASS (3m)

The recently developed single domain crystals in class (3m) such as lithium niobate ($LiNbO_3$) and lithium tantalate have been found to have unusual elastic and optical properties.[27] The applications of these materials in studies of nonlinear optics[28] and of microwave acoustics[29] have become increasingly important. We are interested in the generation and propagation of microwave acoustic waves in these crystals. In Section 2.3.1 general expressions for the velocities and electromechanical coupling constants will be derived. Numerical values based on the measured values of elastic piezoelectric and dielectric constants by Warner and Ohoe[21] and experimental results will be given in Section 2.3.2.

2.3.1 Theory

In this section the generation and propagation of microwave acoustic waves propagating along the three principal crystal axes in half infinite piezoelectric crystals of class (3m) will be considered. The particle displacement for shear waves propagating along the x_1 or x_2 axes in an anisotropic crystal of class (3m) is found to be polarized with an angle with respect to the crystal axes. We will determine the velocities

and the particle displacement polarizations for the normal modes which propagate along crystal axes. Conversion efficiencies for the excitation of normal modes at a single surface in a half infinite crystal of class (3m), and the electromechanical coupling constants for the normal modes, will also be discussed. When the excitation occurs at a single surface, acoustic resonances are not involved. Both theoretical discussion and experimental results for the excitation at a single surface in $LiNbO_3$ crystals (class 3m) will be included in this section. Experiments involving acoustic generation in a thin disk transducer, in which acoustic resonance does take a part, will be treated in Section 2.5.

The single surface excitation and propagation of the normal modes in an x_1-cut $LiNbO_3$ rod will be discussed in detail as an example.

It is customary in this kind of application to mount the crystal in a re-entrant cavity as shown in Fig. 2.2. The re-entrant cavity provides a high Q resonant circuit at microwave frequencies so that relatively high electric fields can be achieved in the surface of the crystal with modest input power. The cross section of the crystal (5×5 mm) is much larger than the acoustic wavelength (in the order of 5μ) so that the situation can be approximated to be a half infinite piezoelectric crystal with a traction free surface at $x_1 = 0$.

The solution for the particle displacements and the velocities for the waves propagating along the x_1-axis in $LiNbO_3$ can be obtained from Eq. (2.11) with the boundary condition of (2.17). The source term in the right hand side of Eq. (2.11) contains only the surface excitation at $x_1 = 0$ under the assumption given in Eq. (2.10d), The internal source due to the nonzero values of $\partial D_2/\partial x_1$ and $\partial D_3/\partial x_1$ is assumpted to be negligible.

The justification of the assumption given in Eq. (2.10d) for $LiNbO_3$ crystals comes from the experimental results. Assuming that all the strain waves generated in the $LiNbO_3$ crystal contribute to the induced displacement D_{ind} in the crystal, it can be shown that the

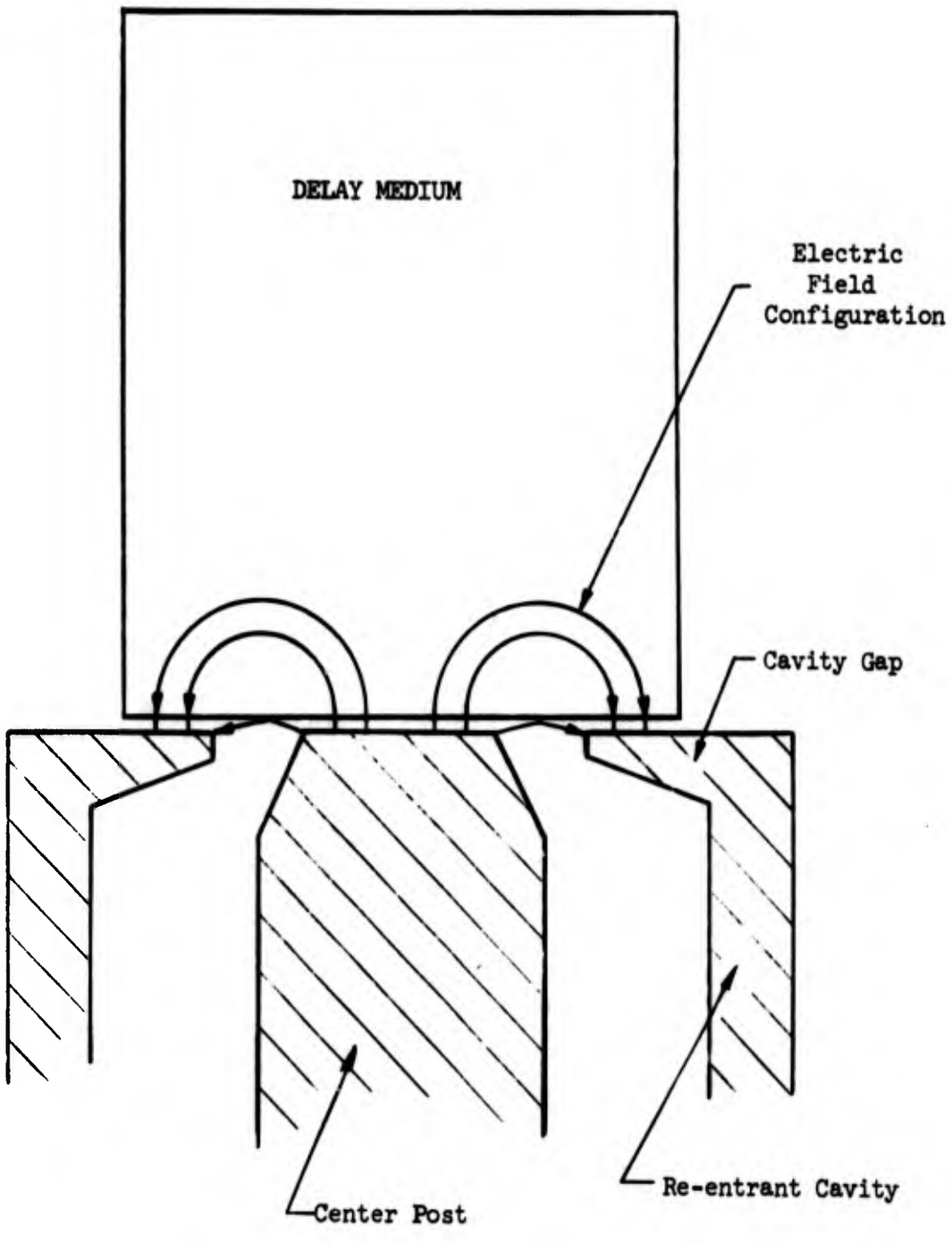

FIG. 2.2--Electric field configuration in the surface of a crystal mounted on a re-entrant cavity.

ratio of the maximum possible D_{ind} to D_a is given by [derived from Eq. (2.33)]

$$\left(\frac{D_{ind}}{D_a}\right)^2 = \left(\frac{e_{pgh}\, S_{gh}}{\epsilon^S_{pp} (E_a)_p}\right)^2 = \mu_{pgh}\, K^2_{pgh}\, \frac{t}{\Lambda_{gh}}\, \frac{\pi}{Q_0} \quad , \qquad (2.18a)$$

where μ_{pgh} is the conversion efficiency for S_{gh} excited by $(E_a)_p$; K^2_{pgh} is the electromechanical coupling constant for S_{gh} ; Λ_{gh} is the wavelength of S_{gh} ; Q_0 is the cavity Q_0 ; and t is the effective thickness of the crystal. As shown in Table I, which will be discussed later, the typical values for a 13 dB conversion loss transducer, $\mu_{pgh} = 0.05$, $K^2_{pgh} = 0.446$, $Q_0 = 1200$ and $\Lambda_{gh} = 5 \times 10^{-4}$, give

$$\left(\frac{D_{ind}}{D_a}\right)^2 = 0.125\, t \quad . \qquad (2.18b)$$

Usually the effective thickness t is less than 0.5 cm. Therefore, the maximum possible induced displacement D_{ind} is in order of $0.25\, D_a$. Actually the induced displacement inside the crystal will be much smaller than the maximum possible D_{ind} due to the balance of induced electric fields E_{ind} . Under the above assumption that the internal source is negligible, Eqs. (2.11) to (2.17) are directly applicable in the calculations for $LiNbO_3$ crystals. For x_1 - cut $LiNbO_3$ crystals, Eq. (2.14) becomes

$$\begin{pmatrix} C_{11} - C & 0 & 0 \\ 0 & C_{66} - C & C_{65} \\ 0 & C_{65} & C_{55} - C \end{pmatrix} \begin{pmatrix} A_1 \\ A_2 \\ A_3 \end{pmatrix} = 0 \qquad (2.19a)$$

where

$$C = \rho \frac{\omega_s^2}{k_s^2} \quad .$$

For a nontrivial solution of (2.19a), the determinant of the coefficients of the A_k must be zero:

$$\begin{vmatrix} C_{11} - C & 0 & 0 \\ 0 & C_{66} - C & C_{65} \\ 0 & C_{65} & C_{55} - C \end{vmatrix} = 0 \quad . \quad (2.19b)$$

The velocities of the three acoustic waves are determined by the three solutions of (2.19b).

The velocities of the three acoustic waves are given by

$$v^{(i)} = \sqrt{\frac{C^{(i)}}{\rho}} \quad (i = 1, 2, 3) \quad (2.19c)$$

where

$$C^{(1)} = C_{11} \quad (2.20a)$$

$$C^{(2)} = \frac{1}{2}\left\{(C_{55} + C_{66}) - \sqrt{(C_{55} - C_{66})^2 + 4\,C_{65}^2}\right\} \quad (2.20b)$$

$$C^{(3)} = \frac{1}{2}\left\{(C_{55} + C_{66}) + \sqrt{(C_{55} - C_{66})^2 + 4\,C_{65}^2}\right\} \quad , \quad (2.20c)$$

and ρ is the density of the crystal. The amplitude ratios of the acoustic waves can be found from Eq. (2.19a); for the wave with velocity

$v^{(1)}$, which is a longitudinal wave propagating along the x_1 - axis, we have

$$\left(A_1^{(1)} : A_2^{(1)} : A_3^{(1)}\right) = \left(1 : 0 : 0\right) \; ; \quad (2.21)$$

for the $v^{(2)}$ wave,

$$\left(A_1^{(2)} : A_2^{(2)} : A_3^{(2)}\right) = \left(0 : 1 : \beta^{(2)}\right) \quad (2.22a)$$

with

$$\beta^{(2)} = \frac{c^{(2)} - c_{66}}{c_{65}} \; ; \quad (2.22b)$$

and for the $v^{(3)}$ wave,

$$\left(A_1^{(3)} : A_2^{(3)} : A_3^{(3)}\right) = \left(0 : \beta^{(3)} : 1\right) \quad (2.23a)$$

with

$$\beta^{(3)} = \frac{c^{(3)} - c_{55}}{c_{65}} \; . \quad (2.23b)$$

In general, we need all three acoustic waves to satisfy the boundary conditions. The total particle displacements for all three acoustic waves (omit the $e^{j\omega_s t}$ term) are

$$U_1 = A_1^{(1)} e^{-jk_s^{(1)}x_1} \quad (2.24a)$$

and

$$U_2 = A_2^{(2)} e^{-jk_s^{(2)}x_1} + \beta^{(3)} A_3^{(3)} e^{-jk_s^{(3)}x_1} \qquad (2.24b)$$

$$U_3 = \beta^{(2)} A_2^{(2)} e^{-jk_s^{(2)}x_1} + A_3^{(3)} e^{-jk_s^{(3)}x_1} \quad . \qquad (2.24c)$$

Substituting Eqs. (2.24a), (2.24b), and (2.24c) into Eq. (2.17) gives the solutions for the amplitudes of the particle displacements:

$$A_1^{(1)} = \frac{j(E_a)_p e_{p11}}{k_s^{(1)} C_{11}} \qquad (2.25a)$$

$$A_2^{(2)} = \frac{j(E_a)_p}{k_s^{(2)}} F_p^{(2)} \qquad (2.25b)$$

$$A_3^{(3)} = \frac{j(E_a)_p}{k_s^{(3)}} F_p^{(3)} \quad , \qquad (2.25c)$$

where

$$F_p^{(2)} = \frac{\{e_{p6}[c_{56}\beta^{(3)} + c_{55}] - e_{p5}[c_{66}\beta^{(3)} + c_{56}]\}}{[c_{55} c_{66} - c_{56}^2][1 - \beta^{(2)}\beta^{(3)}]} \qquad (2.26a)$$

$$F_p^{(3)} = \frac{\{e_{p5}[c_{66} + \beta^{(2)}c_{56}] - e_{p6}[c_{55}\beta^{(2)} + c_{65}]\}}{[c_{55} c_{66} - c_{56}^2][1 - \beta^{(2)}\beta^{(3)}]} \qquad (2.26b)$$

and

$$\beta^{(2)} A_2^{(2)} = A_3^{(2)} \quad , \quad A_2^{(3)} = \beta^{(3)} A_3^{(3)} \quad . \qquad (2.27)$$

It should be noticed that the particle displacements of the two shear waves are coupled together. For the $v_{(2)}$ shear mode, the resultant particle displacement is

$$\underset{\sim}{u}^{(2)} = + A_2^{(2)} [\bar{x}_2 + \beta^{(2)} \bar{x}_3] \, e^{j[\omega_s t - k_s^{(2)} x_1]} \qquad (2.28)$$

and for the $v_{(3)}$ shear mode,

$$\underset{\sim}{u}^{(3)} = A_3^{(3)} [\beta^{(3)} \bar{x}_2 + \bar{x}_3] \, e^{j[\omega_s t - k_s^{(3)} x_1]} \qquad (2.29)$$

where $\bar{x}_2$ and $\bar{x}_3$ are unit vectors.

The acoustic power density for each acoustic wave generated in the interface at $x_1 = 0$ is given by

$$P_{AC}^{(i)} = \frac{1}{2} c^{(i)} v^{(i)} \left| \frac{d}{dx_1} \underset{\sim}{u}^{(i)} \right|^2 \qquad (2.30)$$

$$(i = 1, 2, 3) \quad ,$$

where $c^{(i)}$ is one of the solutions of Eq. (2.19a) and $v^{(i)}$ is the velocity of one of the three acoustic modes. The conversion efficiency from the electromagnetic to acoustic energies is defined as the ratio of the acoustic power of a particular acoustic mode generated in the

crystal to the input electromagnetic power P_{in} into the crystal. P_{in} is given by

$$P_{in} = \frac{\omega W}{Q_0} \tag{2.31}$$

where Q_0 is the unloaded Q of the cavity. Under the critical coupling condition, Q_0 is equal to Q_{ext} which determines the amount of input power to the crystal. The electric energy W is stored in the crystal within an effective volume V ,

$$W = \frac{1}{2} \epsilon_{pp} (E_a)_p^2 V \quad . \tag{2.32}$$

The acoustic power generated for the $v^{(i)}$ acoustic mode is given by Eq. (2.30). Therefore the conversion efficiency of the acoustic waves propagating along the crystal axis is found to be

$$\mu^{(i)} = K_i^2 \frac{Q_0 \Lambda^{(i)} A}{2\pi V} \quad , \tag{2.33}$$

where K_i^2 is the electromechanical coupling constant, $\Lambda^{(i)}$ is the wavelength of the acoustic wave and A is the cross section of the acoustic beam.

The electromechanical coupling constants K_i^2 for the three acoustic waves are found to be:

$$K_1^2 = \frac{(e_{p11})^2}{\epsilon_{pp}^s C_{11}} \tag{2.34}$$

and

$$K_2^2 = \frac{c^{(2)}}{\epsilon_{pp}^s} [F_p^{(2)}]^2 \left\{ [\beta^{(2)}]^2 + 1 \right\} \qquad (2.35)$$

$$K_3^2 = \frac{c^{(3)}}{\epsilon_{pp}^s} [F_p^{(3)}] \left\{ [\beta^{(3)}]^2 + 1 \right\} \quad , \qquad (2.36)$$

where the subscripts 1, 2, 3 for K_i^2 and (1), (2), (3) in above equations indicate the longitudinal wave with the velocity $v^{(1)}$, the shear wave with the velocity $v^{(2)}$ and the second shear wave $v^{(3)}$, respectively; $F_p^{(2)}$ and $F_p^{(3)}$ are given in Eqs. (2.26a,b); $\beta^{(2)}$ and $\beta^{(3)}$ are given in Eqs. (2.22b) and (2.23b); and p is the direction of the applied electric field at the interface $x_1 = 0$.

For the cases that plane acoustic waves propagate along the x_2-axis (y-axis) in y-cut crystals, similar arguments as those for the cases of a x-cut crystal hold. The velocities of the three acoustic modes for the particle displacement $u_i = A_i e^{j(\omega_s t - k_s x_2)}$ are given by

$$v^{(i)} = \sqrt{\frac{c^{(i)}}{\rho}} \quad , \qquad (2.37)$$

$$(i = 1, 2, 3)$$

where

$$c^{(1)} = c_{66} \qquad (2.38a)$$

and

$$c^{(2)} = \frac{1}{2}\left\{(c_{22} + c_{44}) + \sqrt{(c_{22} - c_{44})^2 + 4\,c_{24}^2}\right\} \qquad (2.38b)$$

$$c^{(3)} = \frac{1}{2}\left\{(c_{22} + c_{44}) - \sqrt{(c_{22} - c_{44})^2 + 4\,c_{24}^2}\right\} \quad . \qquad (2.38c)$$

The amplitude ratios of the particle displacement for each mode are found to be

$$\text{for } v^{(1)} \text{ mode: } \left(A_1^{(1)} : A_2^{(1)} : A_3^{(1)}\right) = \left(1 : 0 : 0\right) \qquad (2.39)$$

$$\text{for } v^{(2)} \text{ mode: } \left(A_1^{(2)} : A_2^{(2)} : A_3^{(2)}\right) = \left(0 : 1 : \beta^{(2)}\right) \qquad (2.40)$$

$$\text{for } v^{(3)} \text{ mode: } \left(A_1^{(3)} : A_2^{(3)} : A_3^{(3)}\right) = \left(0 : \beta^{(3)} : 1\right) \quad , \qquad (2.41)$$

where

$$\beta^{(2)} = \frac{c^{(2)} - c_{22}}{c_{24}} \qquad (2.42a)$$

$$\beta^{(3)} = \frac{c^{(3)} - c_{44}}{c_{24}} \quad . \qquad (2.42b)$$

It is noticed that, from Eqs. (2.39), (2.40), and (2.41), the $v^{(1)}$ mode is a pure shear mode with a particle motion along the x_1 - axis while propagating along the x_2 - axis; the $v^{(2)}$ mode is a quasi-longitudinal wave and the $v^{(3)}$ mode is a quasi shear wave mode.

The amplitudes of the A_j are found to be

$$A_1^{(1)} = \frac{j(E_a)_p \, e_{p6}}{k_s^{(1)} \, C_{66}} \tag{2.43}$$

$$A_2^{(2)} = \frac{j(E_a)_p}{k_s^{(2)}} F_p^{(2)} \tag{2.44}$$

$$A_3^{(3)} = \frac{j(E_a)_p}{k_s^{(3)}} F_p^{(3)} \tag{2.45}$$

where

$$F_p^{(2)} = \frac{\{e_{p2} [C_{24}\beta^{(3)} + C_{44}] - e_{p4} [C_{22}\beta^{(3)} + C_{24}]\}}{[C_{22} C_{44} - (C_{24})^2] [1 - \beta^{(2)}\beta^{(3)}]} \tag{2.46}$$

$$F_p^{(3)} = \frac{\{e_{p4} [C_{22} + \beta^{(2)}C_{24}] - e_{p2} [C_{44}\beta^{(1)} + C_{24}]\}}{[C_{22} C_{44} - (C_{24})^2] [1 - \beta^{(2)}\beta^{(3)}]} \tag{2.47}$$

The expression for the particle displacement, the acoustic power generated, the conversion efficiency and the electromechanical coupling constant for the acoustic mode propagating along the x_2 - axis are identical with the expressions in Eqs. (2.28), to (2.36) with $F_p^{(2)}$ and $F_p^{(3)}$ given by Eqs. (2.46) and (2.47).

For the case that the acoustic waves are generated at the surface at $x_3 = 0$ and propagate along the x_3 - axis of the crystal, it is easier to obtain the solutions for the particle displacements since the three acoustic waves are not coupled to each other in this case. It is

found that the velocities of the three waves are determined by the three solutions of

$$\begin{vmatrix} C_{55} - C & 0 & 0 \\ 0 & C_{44} - C & 0 \\ 0 & 0 & C_{33} - C \end{vmatrix} = 0 \quad . \quad (2.48)$$

The resultant particle displacements for these waves are

$$\text{for } v^{(1)}, \quad [A_1^{(1)} : 0 : 0] \quad (2.49)$$

$$\text{for } v^{(2)}, \quad [0 : A_2^{(2)} : 0] \quad (2.50)$$

$$\text{for } v^{(3)}, \quad [0 : 0 : A_3^{(3)}] \quad (2.51)$$

where

$$A_1^{(1)} = \frac{j(E_a)_p \, e_{p5}}{k_s^{(1)} \, C_{55}} \quad (2.52)$$

$$A_2^{(2)} = \frac{j(E_a)_p \, e_{p4}}{k_s^{(2)} \, C_{44}} \quad (2.53)$$

$$A_3^{(3)} = \frac{j(E_a)_p \, e_{p3}}{k_s^{(2)} \, C_{33}} \quad . \quad (2.54)$$

The electromechanical coupling constants are found to be

$$K_1^2 = \frac{(e_{p5})^2}{\epsilon_{pp}^s C_{55}} \tag{2.55}$$

$$K_2^2 = \frac{(e_{p4})^2}{\epsilon_{pp}^s C_{44}} \tag{2.56}$$

$$K_3^2 = \frac{(e_{p3})^2}{\epsilon_{pp}^s C_{33}} \tag{2.57}$$

2.3.2 Numerical and Experimental Results

The elastic, piezoelectric, and dielectric constants of $LiNbO_3$ have recently been measured by Warner and Onoe.[21] Based on these measured values (Table Ia), we calculated in Table Ib the values of velocities, the direction of particle displacement and the electromechanical coupling constants for the possible waves propagating along the crystal axes with all the configurations of the excitation electric fields as discussed in Section 2.3.1.

The calculated values for the velocities have two columns as shown in Table I. The velocities in the first column are calculated based on the stiffened elastic constants, given by Eq. (2.5b), while the velocities in the second column are calculated with the unstiffened constant, C_{mn}^E. The particle displacement direction given in direction cosines and electromechanical coupling constants K_i^2 are calculated using the equations derived in the previous section. Also shown in Table I are the measured values of velocities. The velocities are measured by the usual pulse echo technique[30] and Bragg diffraction technique.

In the pulse echo measurement the oriented $LiNbO_3$ crystals (x-cut, y-cut or z-cut) are mounted in a re-entrant cavity as shown in Fig. 2.2. The acoustic waves generated in the end surface of the crystal depend on the electric field configuration at the surface of the crystal. In Fig. 2.2, the electric field in the surface of the center post is normal to

Table I(a)

Constants of Lithium Niobate[21]

Density (kg/m^2) $\rho = 4.7 \times 10^3$

Relative dielectric constants $\begin{pmatrix} \epsilon_{11}^S/\epsilon_0 & 0 & 0 \\ 0 & \epsilon_{11}^S/\epsilon_0 & 0 \\ 0 & 0 & \epsilon_{33}^S/\epsilon_0 \end{pmatrix}$	$\epsilon_{11}^S/\epsilon_0 = 44$ $\epsilon_{33}^S/\epsilon_0 = 29$
Elastic constants ($\times 10^{11}$ newton/m^2) $\begin{pmatrix} c_{11}^E & c_{12}^E & c_{13}^E & c_{14}^E & 0 & 0 \\ c_{12}^E & c_{11}^E & c_{13}^E & -c_{14}^E & 0 & 0 \\ c_{13}^E & c_{13}^E & c_{33}^E & 0 & 0 & 0 \\ c_{14}^E & -c_{14}^E & 0 & c_{44}^E & 0 & 0 \\ 0 & 0 & 0 & 0 & c_{44}^E & c_{14}^E \\ 0 & 0 & 0 & 0 & c_{14}^E & c_{66}^E \end{pmatrix}$	$c_{11}^E = 2.03$ $c_{12}^E = 0.53$ $c_{13}^E = 0.75$ $c_{14}^E = 0.09$ $c_{33}^E = 2.45$ $c_{44}^E = 0.60$ $c_{66}^E = 0.75$
Piezoelectric constants $\begin{pmatrix} 0 & 0 & 0 & 0 & e_{15} & -e_{22} \\ -e_{22} & e_{22} & 0 & e_{15} & 0 & 0 \\ e_{31} & e_{31} & e_{33} & 0 & 0 & 0 \end{pmatrix}$	$e_{15} = 3.7$ $e_{22} = 2.5$ $e_{31} = 0.2$ $e_{33} = 1.3$

TABLE Ib

Propagation Direction	Type of Wave Excited	Velocities ($\times 10^5$ cm/sec) Calculated (1)	(2)	Measured (3)	(4)	Particle Displacement	Excitation E-Fields	Electromechanical Coupling Constant K_i^2	Conversion Eff. Calculated (-db)	Measured (-bd)
X_1	Shear	4.81	4.1	4.95	4.95	(0,-0.636,0.771)	E_1(norm)	0.446	10	10
	Shear	4.10	3.45	--	4.1	(0, 0.771,0.636)	E_1(norm)	0.0058		
	Long S_{11}	6.84	6.57	6.65	6.5	(1 0 0)	E_2(paral)	0.073		
X_2	Shear S_{12}	4.42	4.0	4.01	4.0	(1 0 0)	E_1(paral)	0.177		
	Long	6.84	6.6	6.9	6.83	(0,1,2.13×10^{-2})	E_2(norm)	0.0532	17.8	16
	Shear	4.53	3.56	4.5	4.3	(0,-2.13×10^{-2},1)	E_2(norm)	0.334	12	13
X_3	Shear S_{13}	4.52	3.58	3.7	--	(1 0 0)	E_1(paral)	0.36		
	Shear S_{23}	4.52	3.58	3.7	--	(0 1 0)	E_2(paral)	0.36		
	Long S_{33}	7.27	7.2	7.3	7.3	(0 0 1)	E_3(norm)	0.027		

(1) Based on stiffened elastic constants
(2) Based on unstiffened elastic constants
(3) Pulse echo measurements
(4) Bragg diffraction measurements

the surface while there are tangential fields in the circular gap between the center post and the gap of the cavity. The velocities are measured in the usual way by measuring the round trip times between delay echoes of each acoustic wave in the crystal. These values are listed in the first column of the measured velocities. The values in the second column of the measured velocities are measured by Bragg diffraction technique; in Chapter IV we discuss the measurement technique. It will be shown that the position of the diffracted light spot critically depends on the Bragg condition

$$\sin \theta_B = \frac{\lambda}{2v_s} f$$

which is related to the velocities of the acoustic waves. By measuring the Bragg angle θ_B we can determine accurately the velocity of the wave. Also the optical probing technique provides a direct observation of the acoustic energy distributions of the acoustic waves generated by the applied electric fields. We will discuss the optical probing in detail in Section 4.3 The measured values of the velocities are shown in column 3 (pulse echo measurement) and column 4 (Bragg diffraction technique).

It is noted that the measured velocities for the waves excited by the normal fields agree satisfactorily with the calculated values in column 1 (the medium is piezoelectrically stiffened) and the measured velocities for the waves excited by the parallel fields check with the calculated values in column 2 (the medium is piezoelectrically unstiffened). These have not been explained satisfactorily yet. The study of the parallel field excitation of acoustic waves in $LiNbO_3$ is still underway.

The electromechanical coupling constants K_i^2 are related to the conversion efficiencies, which can be easily measured experimentally by pulse echo measurement. The conversion efficiencies are shown in (2.33) as a function of K_i^2 , Q_0 , A , $\Lambda^{(i)}$ and the effective volume V of the stored electric energy in the cavity and the crystal. The typical

value of cavity Q_0 is 1200. The cross section A of the acoustic beam can be determined by a laser probe which will be discussed in Section 4.3. For normal field excitation in a re-entrant cavity, the A is found to be equal to the cross section of the center post. Unfortunately there is no easy way to determine accurately the effective volume V of the stored energy. However, the ratio of conversion efficiencies of two acoustic modes that both are excited by normal fields in the re-entrant cavity at the same frequency will be independent of A/V . From Eq. (2.33), the ratio of the conversion efficiencies for the acoustic waves at the same frequency is

$$\frac{\mu^{(i)}}{\mu^{(j)}} = \frac{K_i^2 v^{(i)}}{K_j^2 v^{(j)}} \quad . \qquad (2.58)$$

We have measured the conversion efficiencies for the waves excited by the normal fields in a re-entrant cavity by pulse echo measurement. The measured conversion efficiencies are listed in Table I. If we assign the measured value -10 dB for the shear waves being excited by E_1 and propagating along the x_1 - axis to be equal to the calculated conversion efficiency, all the other calculated values [from Eq. (2.58)] of the conversion efficiencies for other waves are within 1 dB of the measured values as shown in Table I. Based on these values, the filling factor V/A is found to be 0.45 cm from Eq. (2.33), which is a reasonable value for a (5 × 5 × 10 mm) crystal mounted in a re-entrant cavity with A = 60 mils center post.

2.4 INTEGRAL DELAY LINES USING DIELECTRIC RESONATORS

The high Q cavity used in Section 2.3.2 as shown in Fig. 2.2 is to step up the electric fields and to increase the conversion efficiency for the generation of acoustic waves in piezoelectric media. The function of a metal cavity can be replaced by a dielectric resonator.[31] In this section the scheme of using a dielectric resonator to increase the electric field and excite acoustic waves in the surface of a piezoelectric medium will be discussed. Preliminary experimental results will be shown to confirm the theoretical predictions.

2.4.1 Theory

Recently developed single domain crystals of $LiNbO_3$ have unusually large piezoelectric constants e_{ijk}. In addition to this, $LiNbO_3$ has relatively high dielectric constants and small loss tangent,[32] and thus can be used to construct high Q dielectric resonators.[33] The resonant frequencies are determined by the dimensions of the resonators. When the resonators are coupled to electromagnetic waves in a waveguide or coax line, the field configurations in the resonators can be determined. Usually the lower order modes in the resonators are used. For a rectangular parallelpiped the lowest mode TE_{110} for one particular crystalline orientation is shown in Fig. 2.3a. The rf electric field encircles the direction of the magnetic field, which is chosen to coincide with the x_3 axis (c axis) of the (3m) crystal. The electric field has components tangent to the four boundary surfaces which are parallel to the direction of the magnetic field.

If the above resonator is cut into two halves and mounted on a metallic surface as in Fig. 2.4a then, because of the mirror effect of the metallic surface upon the electromagnetic field, the resonant frequency of the half resonator remains the same as that of the original whole resonator. However, the electric field in the bottom surface is now normal to the surface. A typical value of Q_0 is about 3000 for the whole resonators. For half resonators, the Q_0 is lower, about 2000, because of the additional rf loss in the metallic base.

The large piezoelectric constants and the electrical and acoustic Q of the $LiNbO_3$ resonators make it possible in principle to efficiently generate acoustic waves at the surface of the resonators at high microwave frequencies. The acoustic waves can then propagate through the resonators as delay media and reconvert to electromagnetic waves at the surfaces.

The generation of the microwave acoustic waves in the surface of the resonators is due to the surface excitation as discussed in Section 2.3. For half resonators, the excitation fields are normal to the surface, while the whole resonators have parallel field excitations where the electric fields are tangent to the surface. The field

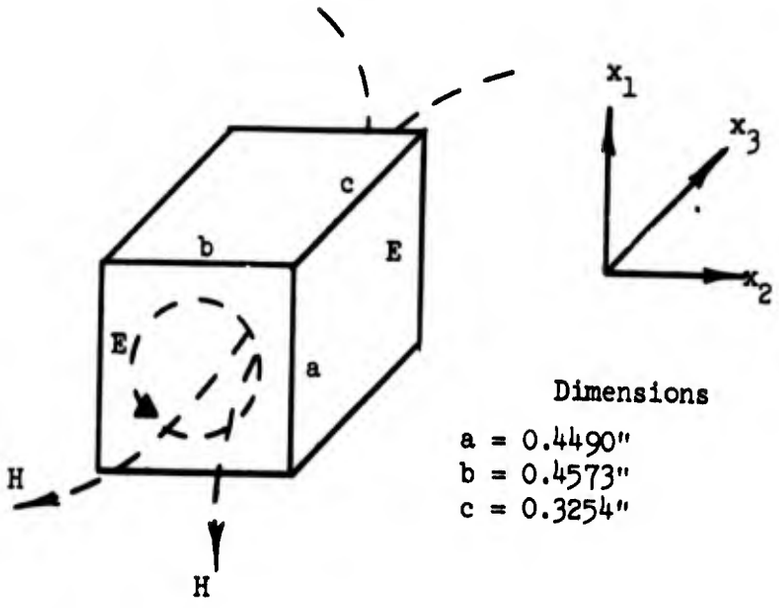

Dimensions

a = 0.4490"
b = 0.4573"
c = 0.3254"

FIG. 2.3(a)--Field configuration in a whole $LiNbO_3$ resonator.

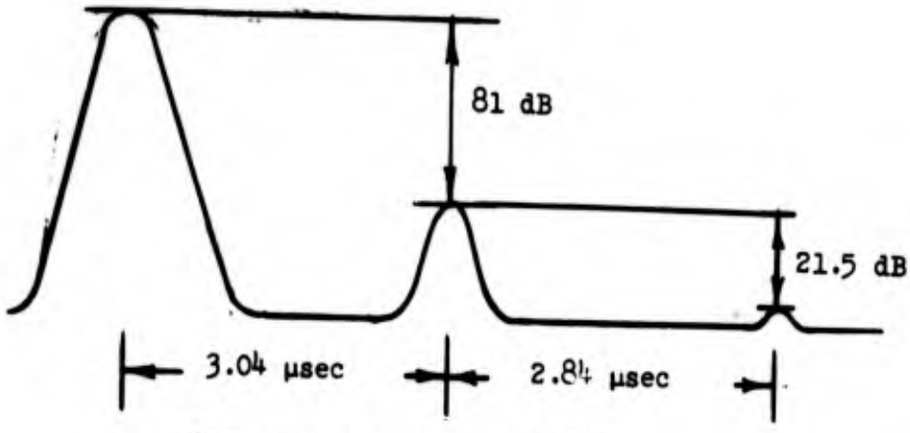

Resonant frequency = 3576 Mc

Conversion eff. = $\frac{81 - 21.5}{2}$ = 29.75 dB

Velocity of the shear wave along the y-axis

= $\frac{1.14 \text{ cm}}{2.84 \text{ μsec}} = 4.02 \times 10^5$ cm/sec

FIG. 2.3(b)--Pulse echo pattern of the shear wave S_{12}.

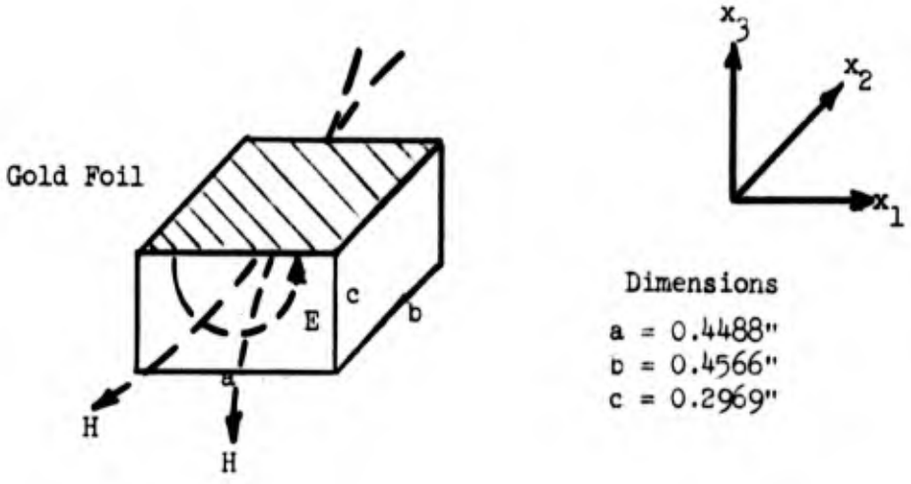

FIG. 2.4(a)--Field configuration in a half $LiNbO_3$ resonator.

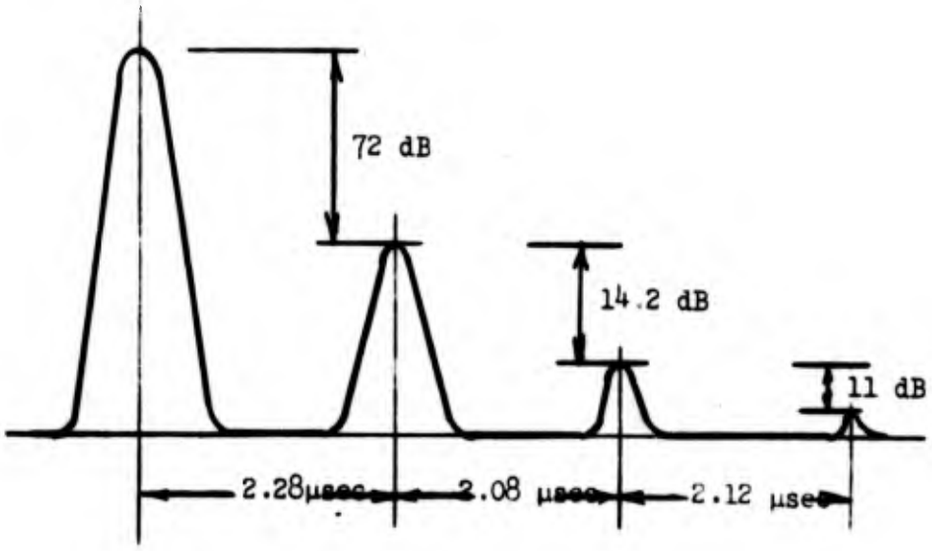

Resonant frequency = 3475 Mc

Conversion eff. = $\frac{72 - 14}{2}$ = 29 dB

Velocity of longitudinal wave along the z-axis

$$= \frac{2 \times 0.743 \text{ cm}}{2.1 \text{ μsec}} = 7.07 \times 10^5 \text{ cm/sec}$$

FIG. 2.4(b) Pulse echo pattern of S_{33} .

distribution of a lowest order mode for a whole resonator under the perfect open circuit condition[31] is shown in Fig. 2.3a. The perfect open circuit condition requires infinite dielectric permittivity for the dielectric resonators. For $LiNbO_3$ resonant at S band frequencies the relative dielectric constant is of the order of 50 when normal to the c-axis of the crystal and of 25 when parallel to the c-axis. These high dielectric permittivities permit most of the input energy to concentrate in the dielectric resonator. As shown in Fig. 2.3a, the E-field configuration in the x_1x_2 plane for the lowest mode TE_{110} in the resonator can be expressed approximately by

$$E_{x_1} = E_{mx_1} \sin \frac{\pi}{a} x_1 \cos \frac{\pi}{b} x_2 \qquad (2.59a)$$

$$E_{x_2} = E_{mx_2} \cos \frac{\pi}{a} x_1 \sin \frac{\pi}{b} x_2 \quad , \qquad (2.59b)$$

where E_{mx_1} and E_{mx_2} are the electric fields at the surfaces of the resonator. It is assumed that there is no variation of the electric field along the x_3 - axis for the lowest mode. The input power P_{in} to the resonator is defined as

$$P_{in} = \frac{\omega W}{Q_0} \quad , \qquad (2.60)$$

where Q_0 is the measured Q_0 of the resonator under the critical coupling condition, ω is the frequency, and W is the total stored energy in the system. When the dielectric constant of the resonator is finite, the total stored energy W is given by

$$W = W_{in} + W_{out} \quad , \qquad (2.61)$$

where W_{in} is the stored energy inside the resonator of a volume V and W_{out} is the stored energy outside the resonator. In order to make an order of magnitude estimation of the ratio W_{out}/W_{in}, consider the experimental set-up of the integral delay line. For the coupling of the electromagnetic fields into the resonator, the resonator is usually placed at the axis of a waveguide, which has a movable short in one end. The movable short produces a standing wave pattern in the waveguide. By adjusting the position of the resonator inside the waveguide, the coupling condition can be over-coupled, critical coupled and under-coupled as shown in Fig. 2.5. The discussion on the coupling to TiO_2 and $SrTiO_3$ resonators have been given by Yee.[31] It has been found that the critical coupling position is located in the weak H-field and strong E-field region as shown in Fig. 2.5. Due to the continuity of tangential electric fields on the surfaces of the resonator, the maximum waveguide electric field E^0 is assumed to be equal to E_{mx_1}. The electric field in the waveguide with a short in one end can then be expressed as

$$E^0 = E_{mx_1} \sin \frac{\pi}{d_3} x_3 \sin \frac{\pi}{d_2} x_2 \quad , \qquad (2.62)$$

where d_3 is the width of the waveguide and $d_2 = \lambda/2$ is the distance from the short. The energy stored in the waveguide is found by integrating over the volume V^0

$$W_{out} = \frac{1}{8} \epsilon_0 E^2_{mx_1} V^0 \quad , \qquad (2.63)$$

where $V^0 = d_2 d_3 h$ is the volume of the waveguide between the resonator and the short. The energy stored in the resonator is readily obtained from Eqs.(2.59a and b) as

$$W_{in} = \frac{1}{8} \epsilon'_{11} \epsilon_0 [(E_{mx_1})^2 + (E_{mx_2})^2] V \quad , \qquad (2.64)$$

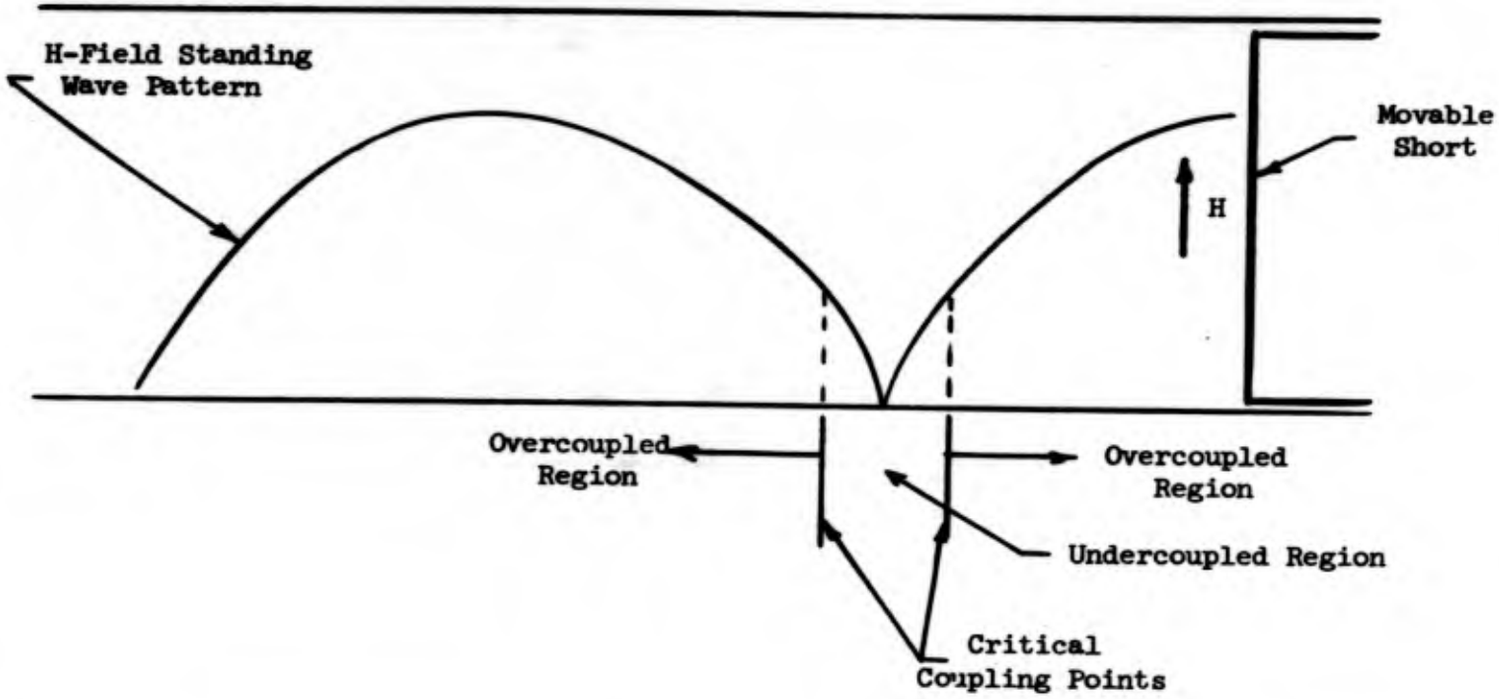

FIG. 2.5--Coupling conditions for a dielectric resonator in a waveguide with a short.

where $V = abc$ is the volume of the resonator and ϵ'_{11} is the relative dielectric constant, i.e., $\epsilon_{11} = \epsilon'_{11}\epsilon_0$. From Eqs. (2.63) and (2.64), we have

$$\frac{W_{in}}{W_{out}} \cong \frac{\epsilon'_{11} V}{V^0} \quad , \tag{2.65}$$

by letting $E_{mx_1} = E_{mx_2}$. In generally, for an S-band $LiNbO_3$ resonator we have $\epsilon'_{11} = 50$ and $V/V^0 = 1/40$. We can see the W_{out} is comparable to W_{in} . Let the total energy of the system W be

$$W = \beta W_{in} \quad , \tag{2.66}$$

where $\beta > 1$ is a factor to include the energy stored outside the resonator.

After determining the energy stored in the system, the conversion efficiencies of the acoustic waves generated can be calculated following the argument of Section 2.3. It is shown in Table I that the tangential electric field in the surface normal to the x_2 - axis will excite a shear S_{12} propagating along the x_2 - axis with velocity v_{12} . The whole resonator as shown in Fig. 2.3a has a field component E_{x_1} [given in Eq. (2.59a)] tangent to the surfaces normal to the x_2 - axis. The acoustic power of S_{12} is found to be [from (2.30)]

$$P_{ac} = \frac{1}{2} c_{66} v_{12} \int_0^a \int_0^c \frac{e_{16}^2}{c_{66}^2} E_{mx_1}^2 \sin^2\left(\frac{\pi}{a} x_1\right) dx_1 \, dx_3$$

$$= \frac{1}{4} \frac{e_{16}^2 E_{mx_1}^2}{c_{66}} v_{12} \, ac \quad . \tag{2.67}$$

The conversion efficiency for generating S_{12} by the parallel field excitation E_{x_1} is then

$$\mu_{16} = \frac{P_{ac}}{P_{in}} = 2 K_{16}^2 \frac{Q_0 \Lambda_{12}}{\pi\beta b} \frac{E_{mx_1}^2}{E_{mx_1}^2 + E_{mx_2}^2} \quad , \qquad (2.68)$$

where

$$K_{16}^2 = \frac{e_{16}^2}{\epsilon'_{11}\epsilon_0 c_{66}}$$

is the electromechanical coupling constant for S_{12} wave; Λ_{12} is the wavelength of the S_{12} wave; b is the distance that S_{12} wave propagates along the x_2-axis; β is the factor discussed in Eq. (2.66). The factor of 2 is due to the two surfaces which generate S_{12} waves. The conversion efficiencies for other acoustic waves excited by the parallel field in the surface of a resonator can be obtained in the same manner.

For half resonators, the excitation fields are normal to the surface next to the metallic base as shown in Fig. 2.4a. Taking a x_3-cut (z-cut) half resonator for example, the field distribution in the x_1x_3 plane are given by

$$E_{x_1} = E_{mx_1} \sin \frac{\pi x_1}{a} \sin \frac{\pi x_3}{2c} \qquad (2.69a)$$

$$E_{x_3} = E_{mx_3} \cos \frac{\pi x_1}{a} \sin \frac{\pi x_3}{c} \quad , \qquad (2.69b)$$

and there is no variation along the x_2-axis. The conversion efficiency for the longitudinal wave S_{33} propagating along the x_3-axis excited by the normal field E_{x_3} is found to be

$$\mu_{33} = K_{33}^2 \frac{Q_0 \Lambda_{33}}{\pi\beta c} \frac{E_{mx_3}^2}{E_{mx_1}^2 + E_{mx_3}^2} \quad ,$$

where Λ_{33} is the acoustic wavelength of the S_{33} wave and c is the distance that S_{33} travels in the crystal.

2.4.2 Experimental Results

The experimental setup for demonstrating the integral delay line application of $LiNbO_3$ resonators is similar to that of the usual pulse-echo measurement. However, the coupling of the delay line to the electrical circuit is much simpler, as the rectangular $LiNbO_3$ resonator is simply placed approximately in the center of a standard waveguide or put in the vicinity of a coupling loop attached to a coax line. We first use a sweep oscillator and observe the reflected signal on a scope, to locate the resonant frequency of the lowest mode of the resonator and to optimize the coupling by adjusting a movable short in the end of the waveguide or rotating the orientation of the coupling loop. We then apply a 1 μsec at a level of a few mw rf power to the resonator and detect the delayed echoes by a standard microwave receiver.

Figure 2.3b shows a typical echo pattern for a whole resonator, while Fig. 2.4b is for a half resonator. The acoustic wave echoes shown in Fig. 2.3b are due to shear waves having strains S_{12} polarized along the x_1 - axis and propagating along the y-axis. The shear waves are generated by the piezoelectric constant e_{112}, and the tangential electric field E_1 of the resonator normal mode at the surface normal to the x_2 - axis. The waves then travel with the shear wave velocity and appear as echoes in the receiver. The velocity of the shear waves along the y-axis, calculated from the distance along the y-axis and the delay time measured between echoes, is about 4.02×10^5 cm/sec which is close to the known shear wave velocity along the y-axis.

The acoustic echoes shown in Fig. 2.4b are produced by longitudinal waves propagating along the x_3-axis. The longitudinal waves, which are generated by the normal field E_3 at the surface next to the metallic base, through the constant e_{333}, have to travel a round trip from the bottom surface to the top surface and back to the bottom surface to produce an echo. The measured velocity of the longitudinal waves in this case is about 7.15×10^5 cm/sec, which also checks with the known value.

The calculated and measured values of the velocities and conversion effects for the whole resonator and half resonator are listed in Table II. It is noted that the measured conversion efficiency of S_{33} in the x_3-cut half resonator checks closely with the calculated value, but the measured conversion efficiency for S_{12} in the whole resonator is about 10 dB lower than the calculated value. This may be due to the critical surface condition over a large area (the wavelength of S_{12} is of the order of 10^{-4} cm). If the surface that generates the S_{12} wave is not flat within one wavelength, interference effect will occur and cancel some of the waves generated. Also the acoustic inhomogeneity is a problem. An acoustic probing device which may resolve the surface flatness and acoustic inhomogeneity is under development. Resonators of this kind are found to constitute a very simple, compact and rugged microwave delay line which couples easily to standard transmission circuits without the critical tolerances on location and alignment within the coupling circuit which are encountered with other types of delay lines.

2.5 $LiNbO_3$ DISK TRANSDUCERS

We have shown in Sections 2.3 and 2.4 that $LiNbO_3$ crystals can efficiently generate microwave acoustic waves. The conversion efficiency as given in Eq. (2.33) is inversely proportional to the effective thickness, which is defined as the ratio of the volume of stored energy v to the cross section of the acoustic beam A, i.e., $t = v/A$. This is the so-called filling factor. In the surface excitation in $LiNbO_3$ crystals as discussed in Section 2.4, the filling factor extends to the length of the crystal used which is in the order of 0.5 cm. In order to decrease the effective thickness, and hence increase the conversion efficiency we have fabricated thin disk x-cut and y-cut $LiNbO_3$ transducers. Also the thin disk transducers can be bonded to any delay media and generate acoustic waves therein. However, the bonding techniques, especially for shear waves, have always imposed some problem. We will discuss the studies of shear wave bonds in Section 4.4.

TABLE II

			Velocities 10^5 cm/sec						Conversion Efficiencies		
Propagation Direction	Excitation E-Field	Types of Wave Excited	Calculated	Measured	f_0 (mc)	Q_0	β	Attenuation dP/μsec	Calc.	Meas.	Dimension (mil)
x_2	E_{x_1}	S_{12}	4	4	3576	2400	2	7.3	21	30	a = 449 b = 4573 c = 325
x_3	E_{x_3}	S_{33}	7.27	7.2	3476	1700	2	7	29	39	a = 449 b = 456 c = 297
x_1	E_{x_1}	Shear	4.85	4.45	2580					39	a = 307 b = 573
		Long S_{11}	6.84	6.8						32	c = 572

The $LiNbO_3$ disk transducers are cut and polished in disk shapes of 5 mils in thickness and 100 mils in diameter. The disk is then bonded to a delay medium (single crystal rods with low acoustic attenuation at microwave frequencies such as sapphire, YAG, quartz and rutile rods,[34] which have been optically polished and made parallel in two ends). Surprisingly, we have discovered that phenyl benzoate provides a convenient and satisfactory bond for the shear wave transducers. Phenyl benzoate is a compound with a melting temperature of 70°C. It will crystallize to form a solid bond when cooled to room temperature. The end of the delay medium, which is to be bonded to the transducer, is coated with a thin layer of gold (1000 Å). The assembly of the transducer and the delay medium is then mounted in a high Q re-entrant cavity as shown in Fig. 2.6. The gold layer serves as an electrode to terminate the E-field which is concentrated in the gap between the center post of the cavity and the gold layer and so reduce the effective thickness. The re-entrant cavity is tunable in the frequency range 0.8 - 2 GHz. Typical values of the Q_0 of the cavity are of the order of 1000. It provides a step-up transformer for the applied electric field in the cavity gap and a frequency selector by tuning the cavity.

The acoustic impedences of the $LiNbO_3$ disk and the delay medium are usually of the same order of magnitude. The acoustic impedance of the bonding material between the transducer and the delay medium may be much smaller than the impedance of the disk transducer and produce an acoustic mismatch for the disk transducer. In Section 4.4 the acoustic impedance of the phenyl benzoate bond and the effect of the friction at the interfaces between the bond and delay medium will be discussed. If there is a large acoustic mismatch between the disk transducer and the phenyl benzoate bond, the disk transducer will be acoustically resonant in thickness vibration modes.

Tiersten obtained the equation which determines the overtone frequency of a piezoelectric plate,[25] e.g.,

$$\text{Tan } k_s t = \frac{k_s t}{K^2} \quad , \qquad (2.70)$$

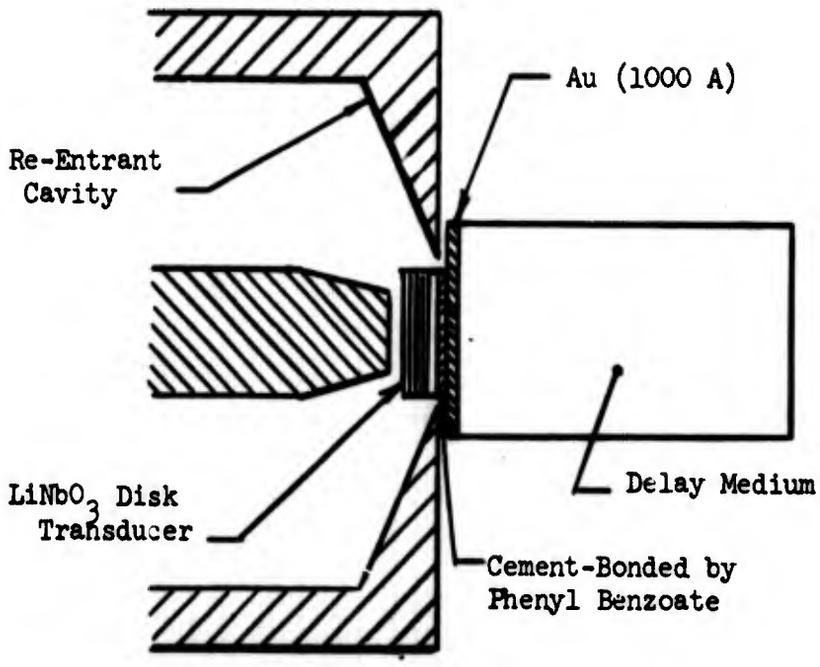

FIG. 2.6--Assembly of a disk transducer bonded on a delay line and a re-entrant cavity.

where k_s is the wavenumber of the acoustic wave, t is the thickness of the plate, and K^2 is the electromechanical coupling for the acoustic wave. The overtone frequencies as shown from Eq. (2.70) are not integral multiples of the fundamental frequency of the plate. However, at high frequencies the overtone frequencies are expected to be close to the multiple integrals of the fundamental. At the frequency of 1 GHz, the overtone frequency is close to the 31st harmonics for a 5 mil x_1 - cut shear wave transducer. At the odd overtone frequencies, where the disk transducer is acoustically resonant, the power absorbed by the disk transducer from the input circuit reaches a peak. When the disk transducer, which is bonded to a delay medium, is mounted in a re-entrant cavity as shown in Fig. 2.5, the resonant absorption lines of the transducer modes as well as of the re-entrant cavity can be observed experimentally. Typical absorption lines of the transducer modes and the cavity are shown in Fig. 2.7a. It is noted that the resonant absorption lines of the transducer modes are sharp, indicating high Q resonances. If the cavity frequency is tuned to coincide with one of transducer resonant modes, a typical double humped resonance curve for two strongly coupled resonant circuits[35] can be observed. The resonance curve of the coupled transducer and cavity is shown in Fig. 2.7b. This shows that we have to calculate the acoustic power generated in the transducer under conditions of acoustic resonance.

The theory for the particle displacement and the acoustic power generation under acoustically resonant conditions in a disk transducer, which is cut from anisotropic piezoelectric crystals with high piezoelectric constants, is not available. The theoretical discussion of the acoustic power generation in Section 2.3 is for single surface excitation in anisotropic piezoelectric crystals with high piezoelectric constants, in which there is no acoustic resonance involved. In this study, no theoretical calculation for the acoustic power generation in a thin disk transducer under resonant conditions will be attempted. Only experimental results of measured conversion efficiencies of the acoustic waves generated in a disk transducer, which is bonded to a delay medium, will be discussed.

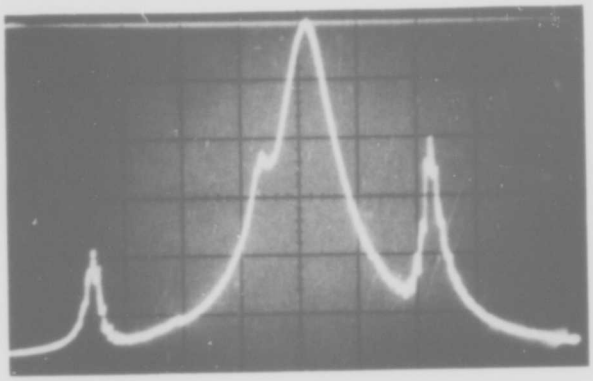

(a) CAVITY AND TWO TRANSDUCER RESONANT ABSORPTION LINES
f_o = 1100 Mc 3 Mc/cm

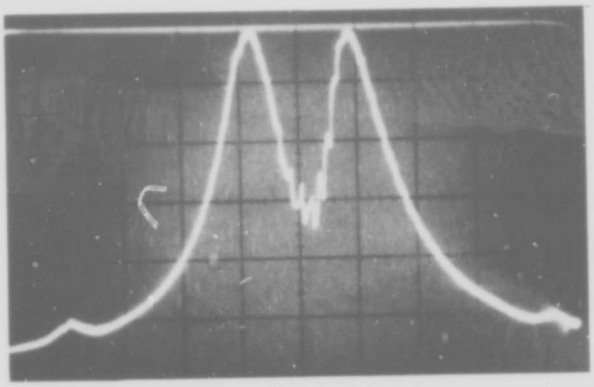

(b) RESONANCE CURVE OF THE COUPLED DISC TRANSDUCER AND CAVITY
f_o = 1070Mc 2Mc/cm

FIGURE 2.7

The experiment was performed in two parts. Figure 2.8a shows the schematic diagram of the experimental set-up for observing resonance curves of the coupled cavity and transducer mode. Typical resonance curves were shown in Fig. 2.7. From these curves, the resonance frequency f_0 of the transducer mode, the unloaded Q of the cavity, the Q_0 of the transducer mode with acoustic loading and the frequency separation between two humps of the resonance curve for the coupled cavity and transducer mode can be measured. The conversion efficiencies of the transducers are measured by pulse echo measurement using the set-up shown schematically in Fig. 2.8b. Table III lists the experimental results for the conversion efficiencies of x-cut and y-cut $LiNbO_3$ disk transducers bonded to a delay medium. The results of this investigation of disk couplers, which have succeeded in producing efficient shear wave generation, are employed in experiments described later.

2.6 EFFICIENT MICROWAVE SHEAR WAVE GENERATION BY MODE CONVERSION[43]

This section is concerned with surface conversion of longitudinal waves to shear waves, through which virtually the full efficiency available for longitudinal wave generation can be applied to shear waves.

It is well known that mode conversion occurs when a plane acoustic wave in a solid strikes a plane boundary surface at an angle,[36] and the use of this process to convert longitudinal waves to shear waves at ultrasonic frequencies has been reported.[37] We have extended this process to the microwave range, and find that single-crystal YAG is capable of very efficient surface conversion.

In Fig. 2.9 an incident longitudinal wave in an isotropic medium, making an angle β with the normal to a free boundary surface in the x,y plane, produces a reflected shear wave at angle α and a reflected longitudinal wave at angle β, such as to satisfy the condition $\sin\alpha/\sin\beta = v_s/v_\ell$, where v_s and v_ℓ are the velocities of shear and longitudinal waves, respectively. The reflected wave amplitudes are functions of the incident angle β, and there is a particular angle for which the reflected longitudinal wave is zero and the total energy of the incident wave appears in the shear wave. For the special case

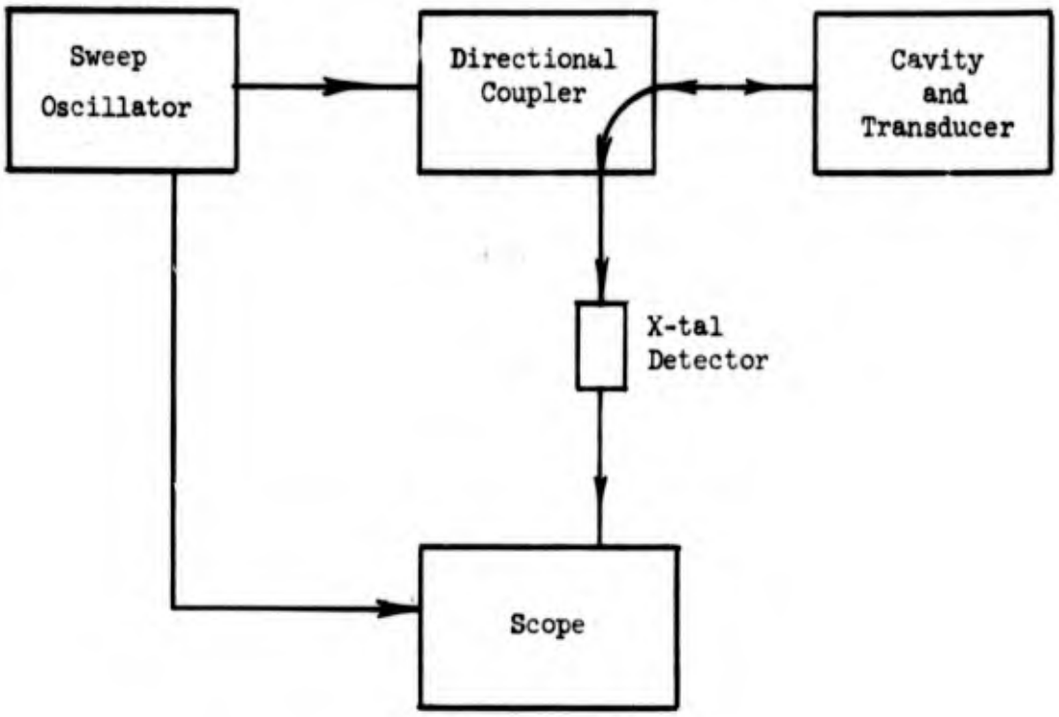

FIG. 2.8(a)--Experimental arrangement for observing resonant absorption lines.

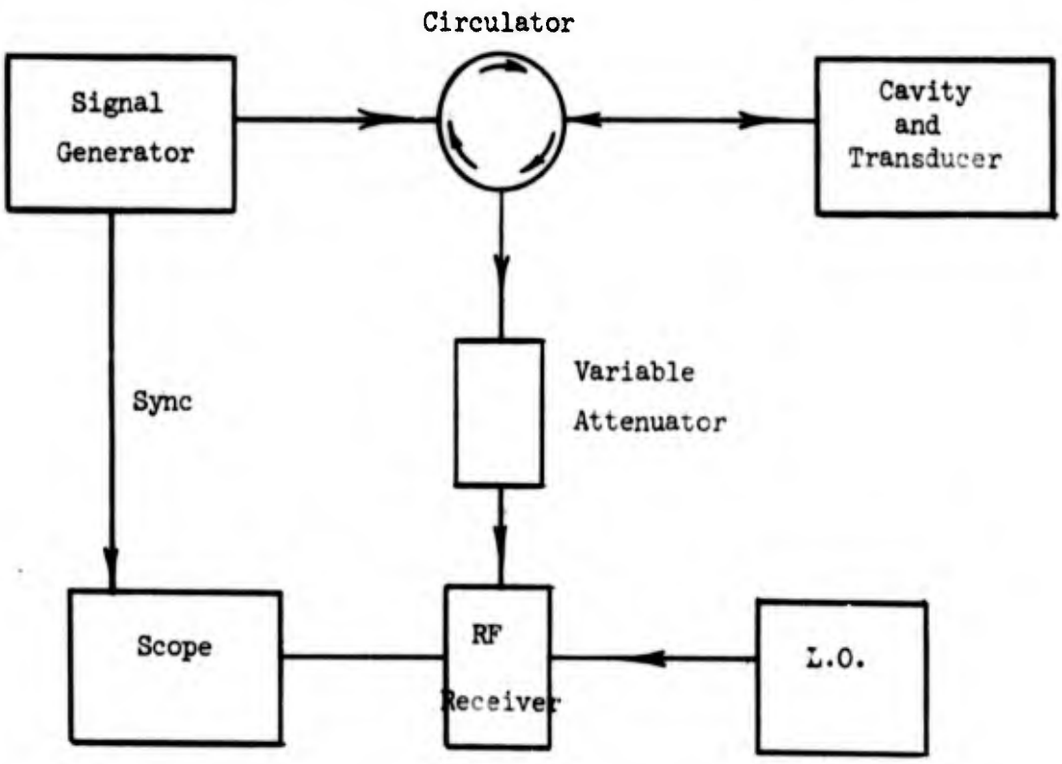

FIG. 2.8(b)--Experimental arrangement for pulse echo measurements.

TABLE III

$LiNbO_3$ Disk Transducer	Delay Medium	Types of Waves Excited	Frequency f_0(Mc)	Cavity Q_0	Transducer Q_{20}	Frequency Separation Δf(Mc)	Measured Conversion Efficiency (dB)	Reference
x-cut (6 mils)	x-cut Sapphire	Shear	1070	800	1000	6.4	-14	M.L. Notebook #990, p. 138
x-cut (6 mils)	x-cut Sapphire	Shear	1030	1000	2000	2.2	- 7.5	M.L. Notebook #990, p. 136
x-cut (6 mils)	c-cut $LiNbO_3$	Shear	1050	350	1050	6	-19	M.L. Notebook #990, p. 133
x-cut (12 mils)	x-cut Sapphire	Shear	1070	470	1400	3.4	-12.5	M.L. Notebook #990, p. 140
y-cut	x-cut	Long.	1030	500	0	0	- 6	M.L. Notebook #990, p. 128
(6 mils)	Sapphire	Shear	1050	500	0	2.5	-17	M.L. Notebook #990, p. 130

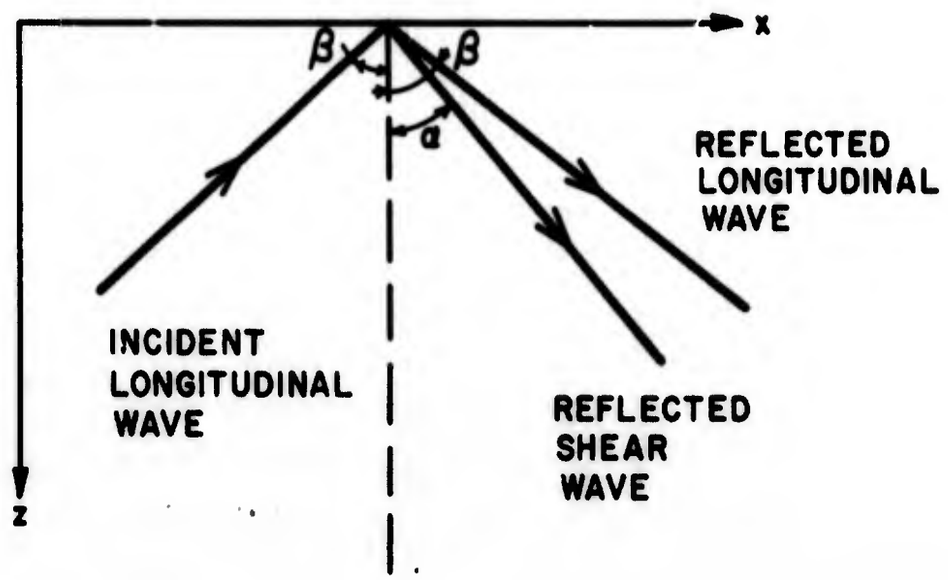

FIG. 2.9--Conversion of a longitudinal plane wave incident on a plane surface at angle β .

$v_\ell/v_s = \sqrt{3}$, the theoretical input angle β for total conversion is 60°, and furthermore $\beta + \alpha = 90^\circ$.

YAG is a cubic crystal with an isotropy factor[38] $2c_{44}/(c_{11}-c_{12})$ of 1.03, so that we can reasonably apply the isotropic analysis. Using the published velocities[38] for YAG, we have $v_\ell/v_s = 1.70$, and we calculate that $\beta + \alpha = 90^\circ$ when $\beta = 59^\circ\ 34.5$ minutes. This is so close to the total-conversion angle that the theoretical intensity of the reflected longitudinal wave is 26 dB below that of the input longitudinal wave when this value is used for the incident angle. Thus, YAG has the property that both the longitudinal and shear waves can propagate along cube edge axes, if desired, and at the same time closely satisfy the conditions for total conversion.

Experiments were carried out using a parrallelopiped sample as illustrated in Fig. 2.10. A ZnO disk transducer was used in a re-entrant cavity in the usual way[23] to generate a longitudinal input wave. The ZnO transducer has an insertion loss of 12 dB, but film transducers of higher efficiency could be readily substituted. This longitudinal wave converts to a shear wave at the right-hand inclined surface. Reflection from the top surface produces an echo which retraces this path back to the transducer.

Clearly, if the right-hand face of the YAG crystal were cut normal to the top and bottom faces, and thus perpendicular to the shear-wave direction, the shear wave could be reflected back from that face without mode conversion, or, alternatively, the shear wave could be transmitted into some other material bonded to the right-hand face. These configurations are of interest for applications of shear waves.

In the present experiment, to simplify testing the surface conversion process, the shear-to-longitudinal conversion at the right-hand surface was included so that echoes could be received at the input transducer even if the angle between the shear wave and the input longitudinal wave were not exactly 90°. Also, it was simpler to make surfaces mutually parallel than to make them mutually perpendicular. Parallelism between the top and bottom faces, and also between the two inclined faces, was held within four seconds of arc, and the flatness of all faces was held to one-tenth wavelength of mercury light.

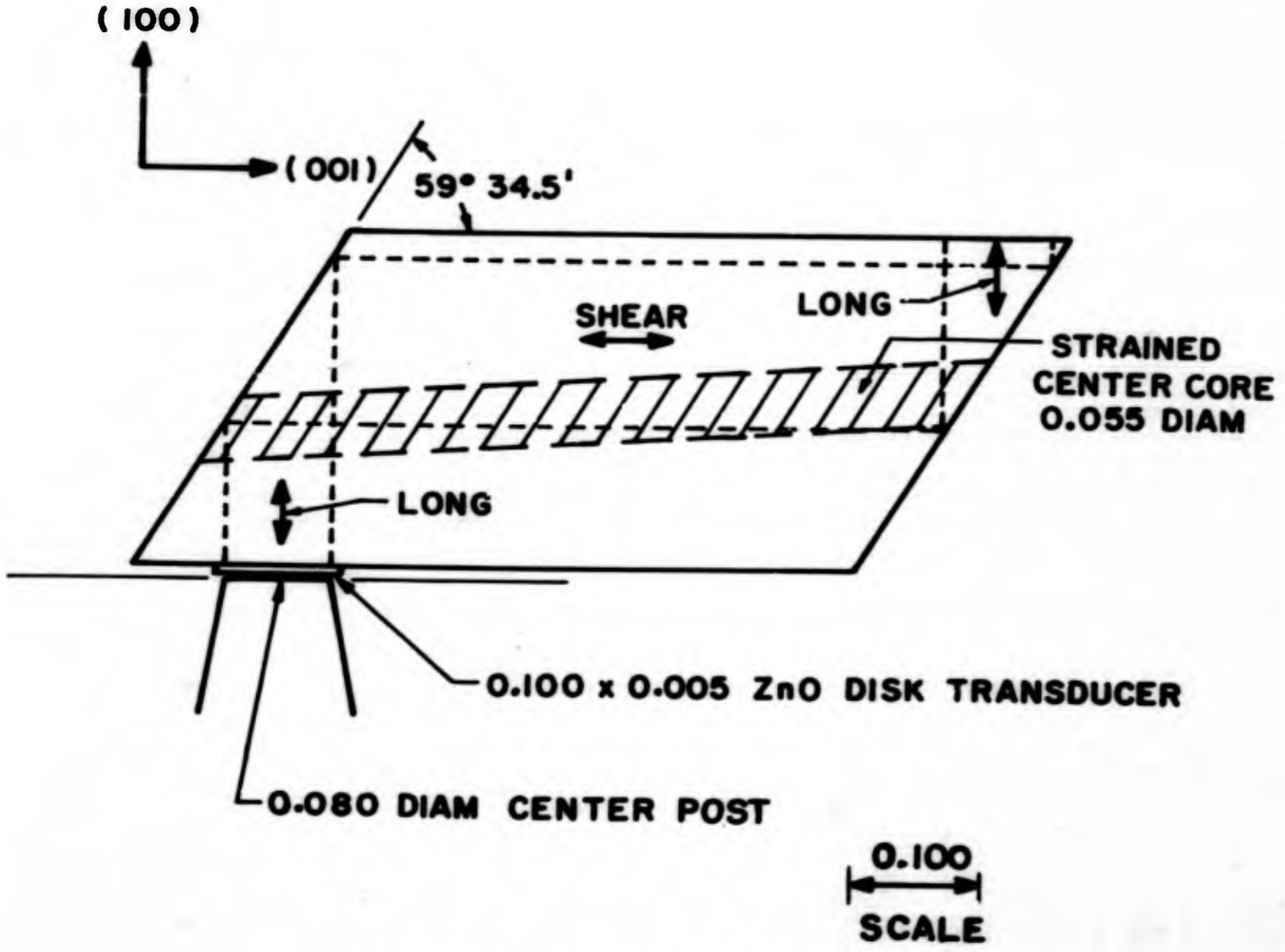

FIG. 2.10--Experimental YAG sample.

Figure 2.11 shows a pulse echo train observed at the input transducer at a frequency of 1461 MHz. The first pulse on the left is the transmitter leakage pulse. Note that each echo pulse has undergone four mode conversions in its transit through the crystal. The time separation between successive echoes is 6.1 microseconds, which agrees with the calculated value of 6.15 microseconds for the round-trip transit time through the crystal, obtained by applying the values[38] for v_s and v_ℓ to the appropriate portions of the wave path in Fig. 2.10. The small spurious pulses which can be seen at the right end of Fig. 2.11 are 48 dB below the first echo pulse.

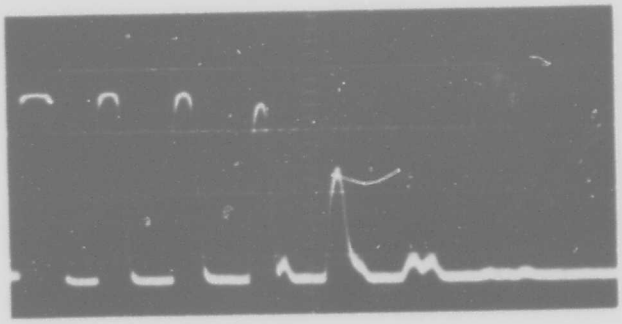

TIME 5 μ sec / div

FIG. 2.11--Pulse echo train of the YAG mode converter.

CHAPTER III

LIGHT DIFFRACTION BY MICROWAVE SHEAR WAVES

3.1 INTRODUCTION

Transverse acoustic waves have very interesting properties and potentially important applications. These arise because of their low propagation velocity, their polarization properties, and their interaction with other types of waves in solids. They have, however, received less attention than longitudinal waves at microwave frequencies. It has been known for a long time that acoustic waves can produce diffraction of optical beams. This process has been studied for the case of microwave longitudinal waves[3] and found to be important for the experimental probing[39] and analysis of longitudinal wave propagations in liquids[40] and solids.[3,39] It has also been found that there are potential applications for microwave devices by using light diffraction of microwave acoustic waves.[41] Diffraction of light by microwave shear waves has not been studied extensively. In this chapter we will discuss the theory of the shear wave diffraction of light. (In the next chapter we will describe the experiments of the shear wave diffraction of light.)

It has been shown that the Bragg diffraction of light by microwave acoustic waves is a parametric interaction process.[11,34] The coupling between the light waves and acoustic waves is through photoelastic effect. Under the normal experimental conditions[42] the Bragg diffraction can be simplified to a three wave parametric interaction involving the incident and diffracted light waves and the strain waves in the crystals. This is called the first-order Bragg diffraction. The theory for the first-order Bragg diffraction by longitudinal waves has been investigated and demonstrated experimentally. The calculation of the Bragg diffraction by microwave shear waves is complicated by the polarization effect of both the light waves and strain waves. This polarization effect, which is a unique property of transverse waves, is the basis of the theory and application of the shear wave diffraction.

A brief review of the photoelastic effect based on Nye[44] will be given in Section 3.2 to discuss the coupling mechanism of the parametric interaction. In Section 3.3 a formulation of the first-order Bragg diffraction by the coupled wave equations for the incident and diffracted lights is discussed and a solution for the field components of the diffracted light under the weak diffraction limit is given. The diffracted field components are essentially determined by the induced displacement vectors in the crystal. In Section 3.4 a calculation of induced displacement vectors for shear wave diffraction in yttrium aluminum garnet crystals (YAG) is given. This illustrates the important characteristic of shear wave diffraction theory.

3.2 PHOTOELASTIC EFFECT

Photoelastic effect describes the change in optical properties in crystals in the presence of elastic waves. In this section we will use Nye's approach[44] to derive quantitatively the relations that exist between the elastic and the optical constants of crystals.

The elastic properties of a crystal under normal condition are characterized by linear Hooke's Law,

$$T_{ij} = C_{ijgh} S_{gh} \qquad (3.1)$$

$$(i,j,g,h = 1, 2, 3)$$

where T_{ij} , S_{gh} are stress and strain tensor; C_{ijgh} is the elastic constant tensor. The optical properties of the crystal are usually specified by the indicatrix,

$$B_{ij} x_i x_j = 1 \qquad (3.2a)$$

$$(i,j = 1, 2, 3) \quad ,$$

where $B_{ij} = \epsilon_0 (\partial E_i / \partial D_j)$ is the impermeability of the crystal and ϵ_0 is the dielectric constant in vacuum. The indicatrix is an ellipsoid

of wave normals whose coefficients are the components of the relative dielectric impermeability tensor B_{ij} at optical frequencies. If coordinates are referred to the principal dielectric axes of the crystal, Eq. (3.2) becomes

$$B_{11}x_1^2 + B_{22}x_2^2 + B_{33}x_3^2 = 1 \quad , \tag{3.2b}$$

and $B_{ii} = 1/\epsilon_{ii}$ $(i = 1,2.3)$ where ϵ_{ii} is the relative dielectric constants along the principal dielectric axes.

The photoelastic effect, which results in a small change of electrical susceptibility in the presence of an elastic strain (or stress), can be described as a small change in the shape, size, and orientation of the indicatrix. This change is most conveniently specified by giving the small changes in the coefficients B_{ij} . Let the coefficient of the indicatrix of the strained crystal be B'_{ij} and

$$B'_{ij} = B_{ij} + \Delta B_{ij} \qquad (i,j = 1, 2, 3) \quad . \tag{3.3}$$

The changes ΔB_{ij} in the impermeability is assumed in the first order approximation to be linearly related to the six strain S_{gh} (or stress) components with photoelastic constants p_{ijgh} which characterize this relationship:

$$\Delta B_{ij} = p_{ijgh}\, S_{gh} \qquad (i,j,g,h = 1, 2, 3) \quad . \tag{3.4}$$

Equation (3.4) is the photoelastic effect due to the strain components in the crystal. A similar relation holds for the stress components in the crystal. If we use the standard matrix notation for symmetrical tensors in which the single subscript m $(m = 1, 2, \ldots 6)$ represents the double subscript ij with $i,j = 1,2,3$, Eqs. (3.3) and (3.4) can be written as

$$B'_m = B_m + \Delta B_m \tag{3.5}$$

$$\Delta B_m = p_{mn}\, S_n \qquad (m,n = 1, 2, \ldots .6) \tag{3.6}$$

where the photoelastic constants P_{mn} form a 6×6 matrix and the S_n constitute a 1×6 matrix.

The indicatrix is the geometrical representation of the optical properties of the crystal. It has the following important property. Draw through the origin of the ellipsoid a straight line parallel to the incident light propagation direction as shown in Fig. 3.1. Draw the central section of the ellipsoid perpendicular to the straight line. The central section will be an ellipse with two semiaxes that are related to the refractive indices of the two waves that may be propagated through the crystal. The direction of the displacement vector D induced in the crystal by the incident E-field may also be found from the ellipse. Draw a line through the center of the ellipse parallel to the incident E-field. At the intersection of the line with the ellipse draw a normal to the ellipse at the intersect point. The direction of the normal is parallel to the D-vector induced by the incident E-field.

The dielectric constants ϵ_m' of the strained crystal, defined as the inverses of the B_m' coefficients, are given by

$$\epsilon_m' = \epsilon_m + \Delta\epsilon_m \quad . \tag{3.7}$$

The $\Delta\epsilon_m$ represent the changes of dielectric constants of the crystal resulting from the acoustic waves. The $\Delta\epsilon_m$ are the fundamental coupling factors for the parametric interaction involved in light diffraction. In matrix notation, $\Delta\epsilon_m$ are the element of a 3×3 dielectric tensor $[\Delta\epsilon]$.

3.3 THREE WAVES PARAMETRIC INTERACTION

It has been shown that the Bragg diffraction of light by acoustic waves is a parametric interaction process.[34] The parametric coupling results from a periodical change in the electrical susceptibility of a material in time and space due to acoustic waves acting through the photoelastic effect. It has been shown that the medium in the presence of acoustic waves can be characterized by the relative dielectric

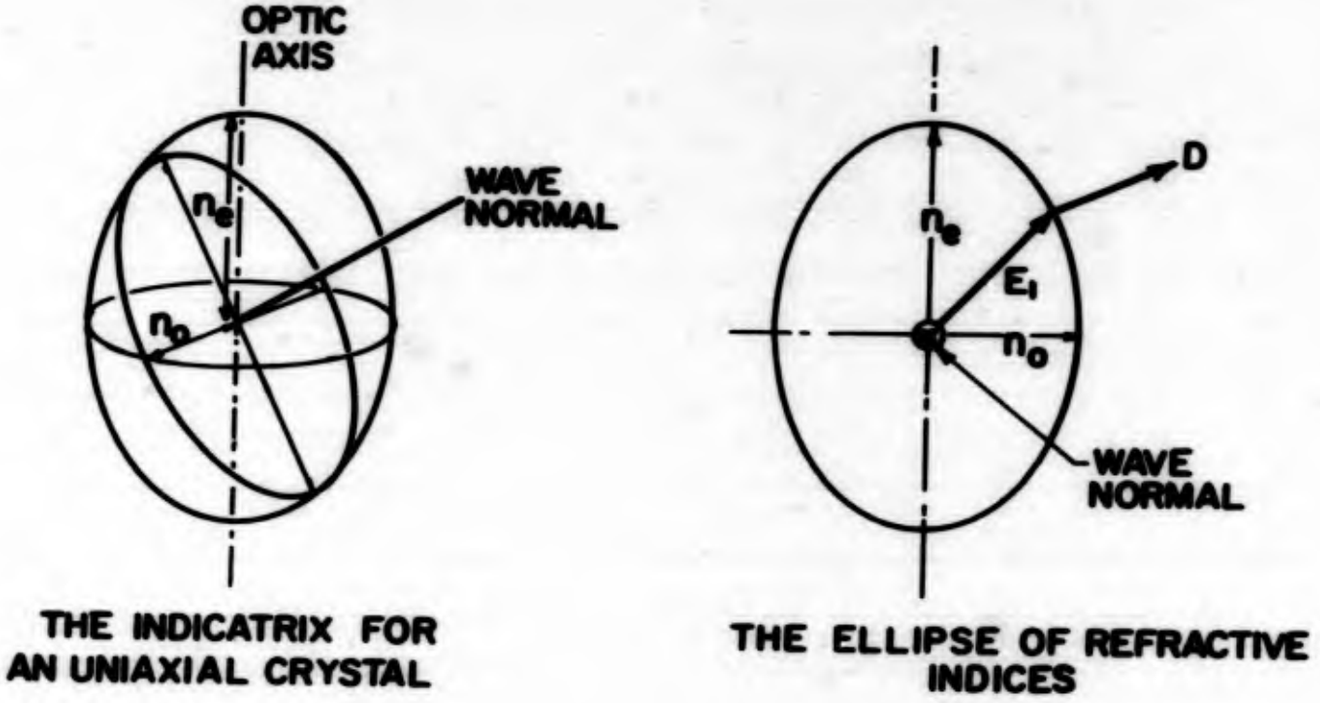

FIG. 3.1--Geometrical representation of indicatrix.

tensor $[\epsilon_n']$ given in Eq. (3.7). The electric fields $\underset{\sim}{E}$, which exist in the strained crystal, can be obtained, in general, from the wave equation

$$\nabla \times \nabla \times \underset{\sim}{E} + \frac{1}{c^2} \frac{\partial^2}{\partial t^2} [\epsilon_n'] \underset{\sim}{E} = 0 \tag{3.8}$$

with proper boundary conditions. As discussed by Slater,[45] the solution may consist of an infinite number of plain waves. In the case of first-order Bragg diffraction, only the incident electric field $\underset{\sim}{E}_1$, the diffracted electric field $\underset{\sim}{E}_2$ and the strain waves given by S_n in the medium are important and one has a three wave parametric interaction. Let

$$\underset{\sim}{E}_1 = \hat{\underset{\sim}{E}}_1 e^{j(\omega_1 t - \underset{\sim}{k}_1 \cdot \underset{\sim}{r})} + \text{c.c.} \tag{3.9}$$

$$\underset{\sim}{E}_2 = \hat{\underset{\sim}{E}}_2 e^{j(\omega_2 t - \underset{\sim}{k}_2 \cdot \underset{\sim}{r})} + \text{c.c.} \tag{3.10}$$

$$S_n = \hat{S}_n e^{j(\omega_s t - \underset{\sim}{k}_s \cdot \underset{\sim}{r})} + \text{c.c.} \quad (n = 1, 2, \ldots 6) , \tag{3.11}$$

where $\hat{\underset{\sim}{E}}_1$ and $\hat{\underset{\sim}{E}}_2$ are the vector amplitudes of the incident and diffracted fields, $\hat{S}_n$ are complex phasors representing strain amplitudes and c.c. designates the complex conjugate. For ω and wave vector $\underset{\sim}{k}$, the subscripts 1, 2 and 3 stand for the incident, the diffracted and the strain waves, respectively.

In the presence of S_n, ϵ_n' was shown in the Section 3.2 to be

$$\epsilon_n' = \epsilon_n + \Delta\epsilon_n \qquad (n = 1, 2, \ldots 6) ,$$

where $\Delta\epsilon_n$ is a function of frequency ω_s and wave vector $\underset{\sim}{k}_s$. The $\Delta\epsilon_n$ can be written

$$\Delta\epsilon_n = \Delta\hat{\epsilon}_n e^{j(\omega_s t - \underset{\sim}{k}_s \cdot \underset{\sim}{r})} + \text{c.c.} , \tag{3.12}$$

where $\Delta\hat{\epsilon}_n$ is the amplitude variation of the dielectric constants due to photoelastic effect.

In the case of first-order Bragg diffraction, the electric fields in the medium are given simply by $\underset{\sim}{E} = \underset{\sim}{E}_1 + \underset{\sim}{E}_2$ and Eq. (3.8) gives

$$\nabla \times \nabla \times (\underset{\sim}{E}_1+\underset{\sim}{E}_2) + \frac{1}{c^2}\frac{\partial^2}{\partial t^2}[\epsilon_n](\underset{\sim}{E}_1+\underset{\sim}{E}_2) = -\frac{1}{c^2}\frac{\partial^2}{\partial t^2}[\Delta\epsilon_n](\underset{\sim}{E}_1+\underset{\sim}{E}_2) \quad . \tag{3.13}$$

Substituting Eqs. (3.9), (3.10), and (3.11) into Eq. (3.13) and equating the same harmonics in the resultant equation, one obtains two sets of coupled equations; the first set for the case $\omega_2 = \omega_1 + \omega_s$ is

$$\nabla \times \nabla \times \underset{\sim}{E}_1 - \frac{\omega_1^2}{c^2}[\epsilon_n]\,E_1 = \frac{\omega_1^2}{c^2}[\Delta\epsilon_n^*]\,E_2 \tag{3.14a}$$

$$\nabla \times \nabla \times \underset{\sim}{E}_2 - \frac{\omega_2^2}{c^2}[\epsilon_n]\,\underset{\sim}{E}_2 = \frac{\omega_2^2}{c^2}[\Delta\epsilon_n]\,E_1 \quad . \tag{3.14b}$$

The second set for the case $\omega_1 = \omega_2 + \omega_s$ is

$$\nabla \times \nabla \times \underset{\sim}{E}_1 - \frac{\omega_1^2}{c^2}[\epsilon_n]\,\underset{\sim}{E}_1 = \frac{\omega_1^2}{c^2}[\Delta\epsilon_n]\,\underset{\sim}{E}_2 \tag{3.15a}$$

$$\nabla \times \nabla \times \underset{\sim}{E}_2 - \frac{\omega_2^2}{c^2}[\epsilon_n]\,\underset{\sim}{E}_2 = \frac{\omega_2^2}{c^2}[\Delta\epsilon_n^*]\,\underset{\sim}{E}_1 \quad . \tag{3.15b}$$

In general, both $\underset{\sim}{E}_1$ and $\underset{\sim}{E}_2$ have three-field components and are functions of three spatial coordinates because of the coupling between $\underset{\sim}{E}_1$ and $\underset{\sim}{E}_2$ in Eqs. (3.14) and (3.15). In principle, $\underset{\sim}{E}_1$ and $\underset{\sim}{E}_2$ could be obtained from (3.14) or (3.15) with proper boundary conditions.

A special case of the three-wave interaction in a half infinite medium, when $\underset{\sim}{E}_1$ and $\underset{\sim}{E}_2$ are coupled only in one coordinate, x_3 (and consequently, are functions of x_3 only) has been formulated and analyzed by Bloembergen.[46] For more general cases, when the interaction region is finite due to finite width of either the acoustic beam or the incident light beam, or both, the solutions for $\underset{\sim}{E}_1$ and $\underset{\sim}{E}_2$ (which are functions of three spatial coordinates) will be complicated. However, for many practical cases the intensity of the diffracted light intensity is not substantially depleted by the diffraction process in which case $\underset{\sim}{E}_1$ may be assumed constant during the interaction process. Equations (3.14) and (3.15) reduce to two independent inhomogeneous differential equations

$$\nabla^2 \underset{\sim}{E}_2 + \frac{\omega_2^2}{c^2} [\epsilon_n] \underset{\sim}{E}_2 = - \frac{\omega_2^2}{c^2} [\hat{\Delta\epsilon}_n] \underset{\sim}{E}_1 e^{-j(\underset{\sim}{k}_1 + \underset{\sim}{k}_s)\cdot \underset{\sim}{r}} e^{j\omega_2 t} \qquad (3.16)$$

for the case $\omega_2 = \omega_1 + \omega_s$ and

$$\nabla^2 \underset{\sim}{E}_2 + \frac{\omega_2^2}{c^2} [\epsilon_n] \underset{\sim}{E}_2 = - \frac{\omega_2^2}{c^2} [\hat{\Delta\epsilon}_n^*] \underset{\sim}{E}_1 e^{-j(\underset{\sim}{k}_1 - \underset{\sim}{k}_s)\cdot \underset{\sim}{r}} e^{j\omega_2 t} \qquad (3.17)$$

for the case $\omega_2 = \omega_1 - \omega_s$.

From the source term of the diffracted light in Eq. (3.16) or (3.17) the field components of the diffracted light are essentially determined by the induced displacement vector $\underset{\sim}{D}_2$, which is the product of the induced dielectric tensor and the incident fields $\underset{\sim}{E}_1$, i.e.,

$$\underset{\sim}{D}_2 = [\hat{\Delta\epsilon}_n] \underset{\sim}{E}_1 \qquad (\text{for } \omega_2 = \omega_1 + \omega_s) \qquad (3.18a)$$

or

$$\underset{\sim}{D}_2 = [\hat{\Delta\epsilon}_n^*] \underset{\sim}{E}_1 \qquad (\text{for } \omega_2 = \omega_1 - \omega_s) \quad . \qquad (3.18b)$$

Here $[\Delta\epsilon_n]$ or $[\hat{\Delta\epsilon}_n^*]$ is a 3×3 matrix and $\underset{\sim}{E}_1$ has three components in general. By choosing the coordinate system such that the direction of the wave vector of the incident light $\underset{\sim}{k}_1$ coincides with one of the coordinates, Eqs. (3.18) and (3.19) can be reduced to two dimensions.

The solution of either Eq. (3.16) or (3.17) can be readily obtained by Green's function technique. For example, the solution of the field component E_{2y} in Eq. (3.16) is found to be

$$E_{2y} = \int_{V'} \frac{\omega_2^2}{c^2} ([\hat{\Delta\epsilon}]\, \underset{\sim}{E}_1)_y\, e^{-j(\underset{\sim}{k}_1+\underset{\sim}{k}_s)\cdot\underset{\sim}{r}'}\, G(\underset{\sim}{r}\cdot\underset{\sim}{r}')\, dV' \quad , \qquad (3.19)$$

where V' is the volume of the source region and the Green's function

$$G(\underset{\sim}{r}\cdot\underset{\sim}{r}') = \frac{e^{-jk_2|\underset{\sim}{r} - \underset{\sim}{r}'|}}{4\pi|\underset{\sim}{r} - \underset{\sim}{r}'|} \qquad (3.20)$$

is the solution of the inhomogeneous wave equation

$$(\nabla^2 + k_2^2)\, G(\underset{\sim}{r} \cdot \underset{\sim}{r}') = -\delta(\underset{\sim}{r} - \underset{\sim}{r}') \quad . \qquad (3.21)$$

In the far field region the following assumptions are valid:

$$|\underset{\sim}{r} - \underset{\sim}{r}'| \approx R - \underset{\sim}{n} \cdot \underset{\sim}{r}'$$

where $\underset{\sim}{n}$ is the unit vector along the direction of $\underset{\sim}{k}_2$, R is the average distance from the source region to the observation point and

$$G(\underset{\sim}{r} \cdot \underset{\sim}{r}') \approx \frac{e^{-jk_2R + j\,\underset{\sim}{k}_2\cdot\underset{\sim}{r}'}}{4\pi R} \quad . \qquad (3.22)$$

Equation (3.19) becomes

$$E_{2y} = \frac{\omega_2^2}{c^2} \left([\hat{\Delta\epsilon}]\, \underset{\sim}{E}_1\right)_y \frac{e^{-jk_2R}}{4\pi R} \int_{V'} e^{-j(\underset{\sim}{k}_1+\underset{\sim}{k}_s-\underset{\sim}{k}_2)\cdot\underset{\sim}{r}'} dV' \quad . \tag{3.23}$$

The diffracted field in Eq. (3.23) will be maximum when the phases of the waves involved are matched, i.e.,

$$\underset{\sim}{k}_1 + \underset{\sim}{k}_s - \underset{\sim}{k}_2 = 0 \quad . \tag{3.24}$$

It should be recognized that Eq. (3.20) together with the equation $\omega_2 = \omega_1 - \omega_3$ are the two fundamental relations, the conservations of momentum and energy, for the three-wave parametric interaction. In general, the magnitudes of $\underset{\sim}{k}_1$ and $\underset{\sim}{k}_2$ may be different in anisotropic crystals. An important application due to the difference in magnitudes of $\underset{\sim}{k}_1$ and $\underset{\sim}{k}_2$ will be discussed in the next chapter. In isotropic crystals magnitudes of $\underset{\sim}{k}_1$ and $\underset{\sim}{k}_2$ are assumed to be equal. The slight change in the magnitude of $\underset{\sim}{k}_2$ due to the frequency change in the diffracted light (the frequency of the diffracted light ω_2 is doppler shifted by the acoustic wave, i.e., $\omega_2 = \omega_1 \pm \omega_s$) is negligible since the acoustic frequency ω_s is 10^5 lower than the incident light frequency ω_1 . Equation (3.24) can then be represented by an isosceles triangle as shown in Fig. 3.2b. A well known relation for Bragg diffraction is readily obtained from the triangle

$$\sin\theta = \frac{|k_s|}{2|k_1|} = \frac{\lambda_1}{2\Lambda} \quad , \tag{3.25}$$

where θ is the Bragg angle in the crystal measured from the acoustic wavefront, λ_1 is the wavelength of the incident light in the medium, and Λ is the acoustic wavelength. The phase mismatch in the waves can be represented by

$$\Delta\underset{\sim}{k} = \underset{\sim}{k}_1 + \underset{\sim}{k}_s - \underset{\sim}{k}_2 \quad . \tag{3.26}$$

By knowing the volume of the source region V', Eq. (3.23) can be integrated. For the case that the source region is a rectangular box with dimensions WLH, Eq. (3.23) becomes

$$E_{2y} = \frac{\omega_2^2}{c^2} \left([\hat{\Delta\epsilon}_n] \underset{\sim}{E}_1\right)_y \frac{e^{-jk_2R}}{4\pi R} WLH\, F_1F_2F_3 \quad , \qquad (3.27a)$$

where

$$F_1 = \frac{\sin \Delta k_x(W/2)}{\Delta k_x(W/2)} \qquad (3.27b)$$

$$F_2 = \frac{\sin \Delta k_y(L/2)}{\Delta k_y(L/2)} \qquad (3.27c)$$

$$F_3 = \frac{\sin \Delta k_z(H/2)}{\Delta k_z(H/2)} \quad , \qquad (3.27d)$$

which are the well known $\frac{\sin X}{X}$ pattern for the diffracted fields as the phases of the waves involved are not exactly matched.[47] The Δk_x, Δk_y and Δk_z are the components of $\Delta \underset{\sim}{k}_s$ given in Eq. (3.26).

3.4 SHEAR WAVE DIFFRACTION IN CUBIC CRYSTALS

In order to demonstrate the important characteristics of the shear wave diffraction theory, we will consider the case of an incident light beam diffracted by a column of shear waves of width W at frequency ω_s propagating along one of the cubic axes in a cubic crystal. As shown in Fig. 3.2(a), the coordinates are chosen so that x_1, x_2 and x_3 are parallel to the cubic edges of the crystal and x_2 coincides with the propagation direction of the shear waves. The shear waves can be characterized by Eq. (3.11) using only two strain components S_4 and S_6. Here S_4 represents the wave for which the direction

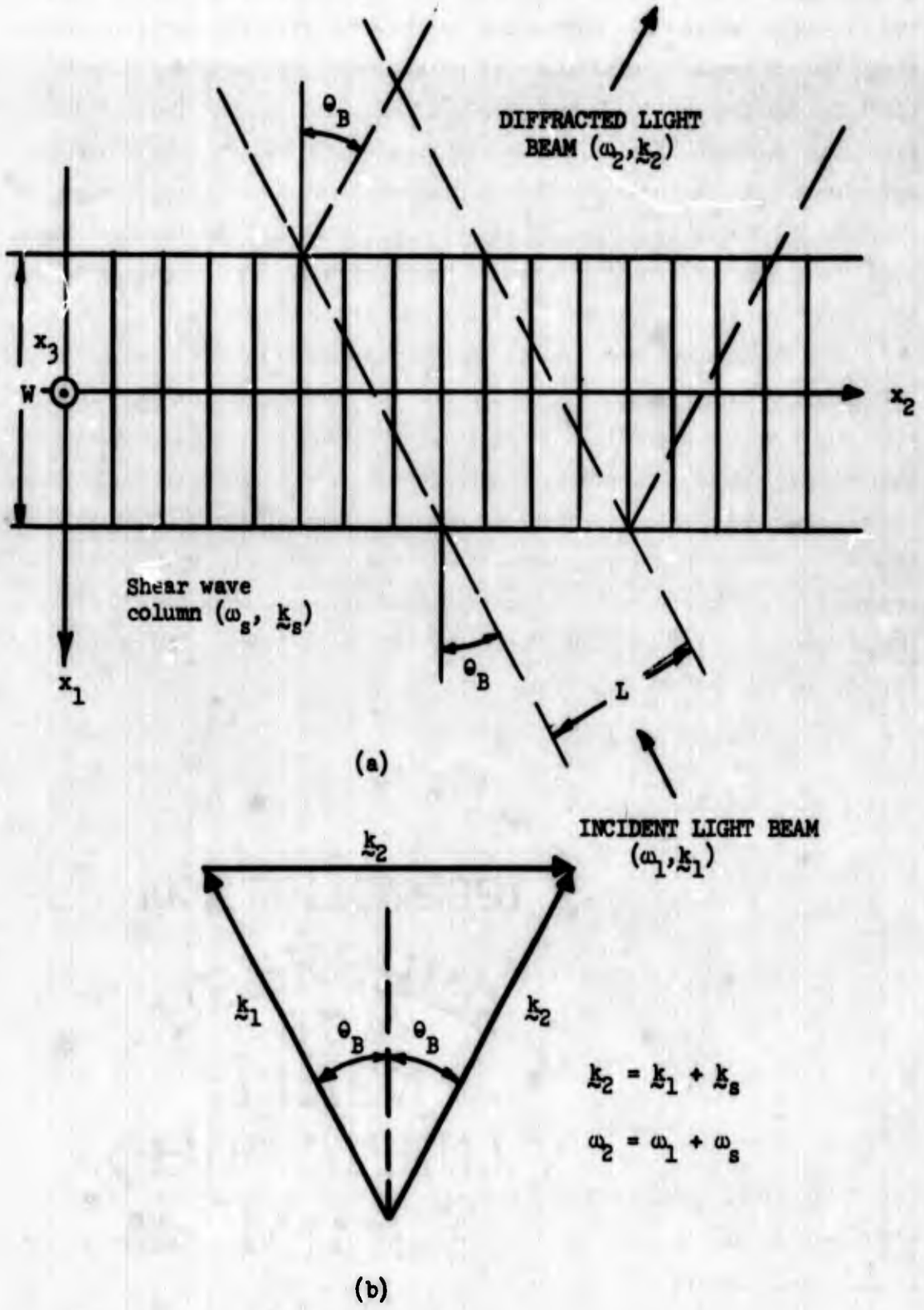

FIG. 3.2--Bragg diffraction by shear waves.

of propagation is along the x_2-axis and the particle motion is along the x_3-axis while S_6 correspond to the wave with the particle motion along the x_1-axis . The state of polarization of the shear waves is specified by the amplitude and phases of S_4 and S_6 . The incident light with a width L is incident at Bragg angle θ_B to the acoustic wave front (the x_1-axis). The diffracted light from the source region (defined by the intersection of the acoustic beam and the incident light beam) is reflected from the acoustic wave front at θ_B as required by the condition of Eq. (3.20a) for isotropic crystals.

Now we proceed to calculate the dipole source for the diffracted light generated by strains S_4 , S_6 and the incident light $\underset{\sim}{E}_1$ in a yttrium aluminum garnet (YAG) crystal. The YAG crystal has excellent optical and elastic properties and we found that it has relatively large photoelastic constants for shear waves. The form of the photoelastic tensor for different classes of crystals can be found by symmetry argument.[48] However, most of the constants have not been published in the literature. YAG belongs to the crystal class (m3m). The photoelastic tensor has the following form:

$$[p_{mn}] = \begin{pmatrix} p_{11} & p_{12} & p_{12} & \cdot & \cdot & \cdot \\ p_{12} & p_{11} & p_{12} & \cdot & \cdot & \cdot \\ p_{12} & p_{12} & p_{11} & \cdot & \cdot & \cdot \\ \cdot & \cdot & \cdot & p_{44} & \cdot & \cdot \\ \cdot & \cdot & \cdot & \cdot & p_{44} & \cdot \\ \cdot & \cdot & \cdot & \cdot & \cdot & p_{44} \end{pmatrix} . \qquad (3.28)$$

YAG crystals, which are optically isotropic have an indicatrix of a YAG crystal in the absence of external strains, given by a sphere defined in Eq. (3.2),

$$B_1(x_1^2 + x_2^2 + x_3^2) = 1 \qquad (3.29)$$

where B_1 is the principal impermeability of the YAG. In the presence of strains S_4 and S_6, the indicatrix of the strained YAG crystal becomes

$$B_1(x_1^2 + x_2^2 + x_3^2) + 2\Delta B_4\, x_2x_3 + 2\Delta B_6\, x_1x_2 = 1 \quad , \qquad (3.30a)$$

where ΔB_4 and ΔB_6 can be found by the product of Eq. (3.28) and the strain wave in the crystal having the components S_4 and S_6 as shown in Eq. (3.6), so that

$$\Delta B_4 = p_{44}\, S_4 \qquad (3.30b)$$

$$\Delta B_6 = p_{44}\, S_6 \quad . \qquad (3.30c)$$

The optical properties such as the index of refraction and the direction of the displacement vector of the unstrained and strained YAG crystal can now be found from the indicatrices and the propagation direction of the incident light. Let the incident light beam be in the x_1x_2 plane and at an angle θ_B with respect to the x_1-axis. Draw a line through the origin of the indicatrix of the unstrained crystal and parallel to the direction of the incident light beam. Draw a central section of the indicatrix normal to the straight line. The central section is a circle as shown in Fig. 3.3a, for the unstrained YAG crystal. This is why the YAG crystal is optically isotropic. For this case the direction of the displacement vector is always parallel to the electric field of the incident light. For the strained crystals the central cross section of the indicatrix seen by the incident light is an ellipse. The equation of the ellipse is found from Eq. (3.30a) and the direction of the incident light is

$$(B_1 - 2\Delta B_6 \sin 2\theta_B)x_2'^2 + x_3'^2 + 2\Delta B_4 \cos\theta_B\, x_2'x_3' = 1 \qquad (3.31)$$

where $x_2'x_3'$ and rotated axes of x_2 and x_3 with respect to the x_3-axis. The angle rotated is θ_B such that x_1' is along the propagation direction of the incident light. Bragg angle θ_B given by

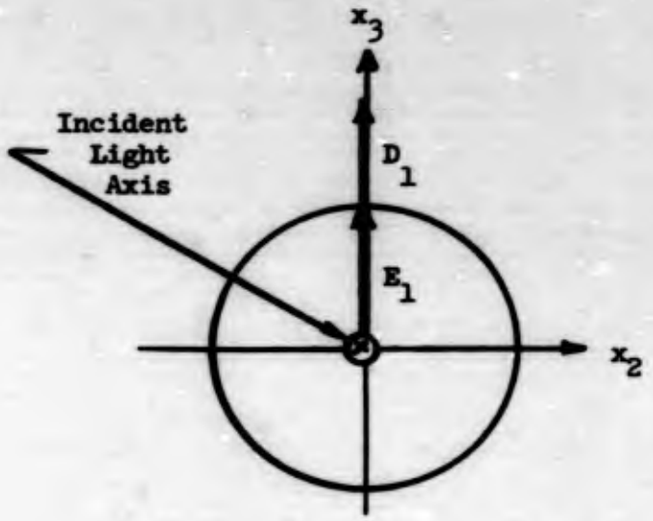

(a) Unstrained cubic crystal.

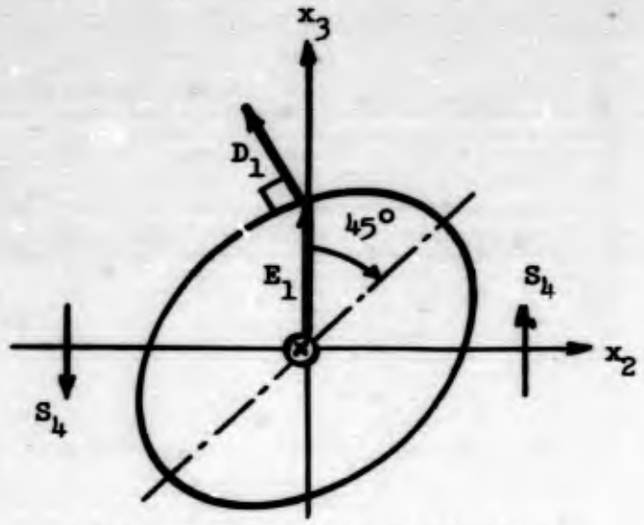

(b) Strained cubic crystal.

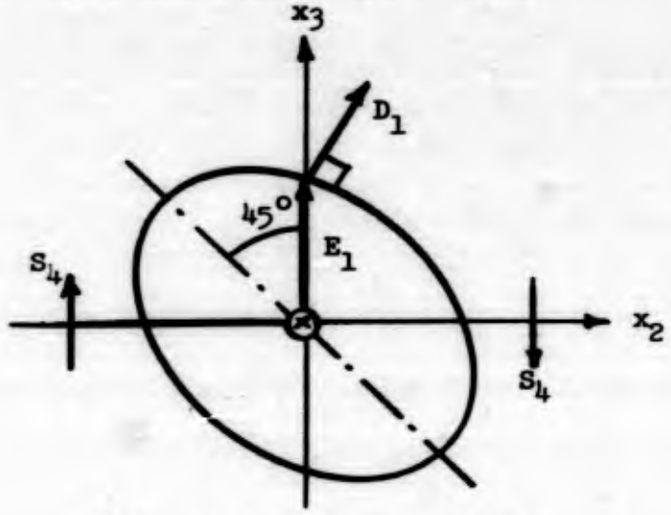

(c) Strained cubic crystal.

(d) Induced displacement vector D_2 by S_4 .

FIG. 3.3--Geometrical presentation of optical properties in cubic crystals.

Eq. (3.25) is in the order of 2 degrees for shear waves at 1 GHz in the YAG crystal. Under normal experimental conditions ΔB_6 is more than two order of magnitude smaller than B_1. The quantity $2\Delta B_6 \sin 2\theta_B$ is therefore negligible compared to B_1. For simplicity, we can assume in the calculation that the incident light is along the x_1-axis. Nevertheless, the small angle θ_B must be satisfied by the incident light in order to observe Bragg diffraction.

The direction of the induced displacement vector $\underset{\sim}{D}_1$, in the strained crystal by a vertically polarized incident light $\underset{\sim}{E}_1$ can be determined geometrically from the ellipse given in Eq. (3.31). As shown in Fig. 3.3b, the ellipse has principle axes rotated 45° with respect to the x_2' and x_3' axes; D_1 is perpendicular to the ellipse at the intersection of the ellipse and $\underset{\sim}{E}_1$ and therefore D_1 is not parallel to E_1. It should be noticed from Eq. (3.31), that the optical properties of the crystal seen by an incident light along the x_1-axis are effected only by the strain component S_4 but not by S_6. If the strain S_4 and ΔB_4 changes sign, the ellipse will rotate 90° as shown in Fig. 3.2c; D_1 must rotate clockwise in order to remain perpendicular to the new ellipse. Due to S_4 (which is a sinusoidal function at frequency ω_s) the ellipse wobbles from Fig. 3.2b to Fig. 3.3c at the frequency ω_s. In Fig. 3.3d we sketch the directions of the induced displacement vectors by $\underset{\sim}{E}_1$ in the strained crystal together. There is a horizontally polarized displacement D_2 induced by the oscillating $\underset{\sim}{D}_1$'s which form the dipole source for the diffracted light. While D_1 vibrates at the frequency of the incident light ω_1, D_2 vibrates at the frequency $(\omega_1 \pm \omega_s)$ due to the modulation of S_4. Similarly, if the incident light is horizontally polarized, a vertically polarized induced dipole D_2 will be produced in the crystal strained by S_4.

If the incident light is rotated 90° and assumed propagating along the x_3-axis, the same argument holds as for the case in which the incident light is along the x_1-axis. There will be a cross polarized dipole D_2 produced in the strained crystal except that D_2 is now induced by S_6 instead of S_4. Recall that S_4 represents the strain wave with the particle motion along the x_3-axis while S_6 with the particle motion along the x_1-axis.

So far we have discussed qualitatively the dipole sources for the diffracted light. Two important characteristics of the shear wave diffraction theory can now be concluded. First, the polarization of the diffracted light is rotated by 90° with respect to the incident light polarization. This feature has experimental advantages. The diffracted light can be conveniently separated from the transmit light and all the scattered light by surface irregularities by a polarizer. The signal-to-noise ratio can be largely improved. Second, we notice that only the strain component which has the particle motion direction perpendicular to the incident beam axis contributes to the diffracted light; S_4 diffracts the incident light which is along the x_1-axis while S_6 diffracts the incident light along the x_3-axis . This polarization effect of the shear waves has important applications.

In order to calculate the magnitude of the induced displacement vector D_2 by the strain waves, we need to know the relative dielectric constants of the strained crystal. The coefficients of the ellipse seen by an incident light along the x_1-axis are given by Eq. (3.30a) can be written in a 2×2 matrix,

$$\begin{pmatrix} B_1 & \Delta B_4 \\ \Delta B_4 & B_1 \end{pmatrix} .$$

According to Eq. (3.7) the dielectric constants which relate the induced displacement vector to the field components of the incident light along the x_1-axis , are

$$\begin{pmatrix} \epsilon_1 & \Delta\epsilon_4 \\ \Delta\epsilon_4 & \epsilon_1 \end{pmatrix} = \begin{pmatrix} \epsilon_1 & -\epsilon_1^2 p_{44} S_4 \\ -\epsilon_1^2 p_{44} S_4 & \epsilon_1 \end{pmatrix} , \qquad (3.32)$$

provided $\Delta B^2 \ll B_1$ which is valid in all the normal experimental conditions. The second matrix in (3.32) is the induced dielectric constants by S_4 . We have then

$$\begin{pmatrix} D_{2y} \\ \\ D_{2z} \end{pmatrix} = \begin{pmatrix} 0 & -\epsilon_1^2 p_{44} S_4 \\ \\ -\epsilon_1^2 p_{44} S_4 & 0 \end{pmatrix} \begin{pmatrix} E_{1y} \\ \\ E_{1z} \end{pmatrix} , \qquad (3.33)$$

where E_{1y} , E_{1z} and D_{2y} , D_{2z} are components of the incident field and the induced D_2 along the x_2 and x_3 axes, respectively. It is obvious from Eq. (3.33), that $\underset{\sim}{D}_2$ is cross-polarized with respect to $\underset{\sim}{E}_1$. For a vertically polarized light having only E_{1z} component, the induced dipole for the diffracted light is horizontally polarized with

$$D_{2y} = -\epsilon_1^2 p_{44} S_4 E_{1z} \quad . \qquad (3.34a)$$

Similarly, a horizontally polarized incident light E_{1y} gives

$$D_{2z} = -\epsilon_1^2 p_{44} S_4 E_{1y} \quad . \qquad (3.34b)$$

Once the induced dipole $\underset{\sim}{D}_z$ is determined, the field components of the diffracted light can then be calculated from Eq. (3.19). For example, let the incident light have only an E_{1z} component. The induced displacement D_{2y} is given by Eq. (3.33b). For simplicity assume the incident light beam has a rectangular cross section with dimensions LH . Due to the negligible small Bragg angle θ_B , the source region at the intersection of the acoustic beam with a width W and the incident light beam can be assumed to be a rectangular box with dimensions LHW . The diffracted field E_{2y} due to D_{2y} is readily found from Eq. (3.27a) to be

$$E_{2y} = k_2^2(\epsilon_1 p_{44} S_4) E_{1z} \frac{e^{-jk_2 R}}{4\pi R} HLWF_1F_2F_3 \quad , \qquad (3.35)$$

where F_1 , F_2 , and F_3 are given in Eqs. (3.27b,c,d). The ratio of the intensities of the diffracted light beam to the incident light beam is

$$\frac{I_2}{I_1} = \frac{|E_{zy}|^2 \times \text{spot size of } I_2}{|E_{1z}|^2 \times \text{spot size of } I_1} \quad . \tag{3.36}$$

The spot size of I_2 is determined by the far field diffraction pattern of Eq. (3.35) which is the sin x/x pattern of F_2 and F_3 . Most of the intensity in the diffracted light is seen within the area defined by the first minimum of F_2 and F_3 . It can be shown that the angle spread for the first minima of F_2 is

$$2\Delta\theta = \frac{2\pi}{k_2 L} \quad . \tag{3.37}$$

Similarly, the angle spread for F_3 is

$$2\Delta\varphi = \frac{2\pi}{k_2 H} \quad . \tag{3.38}$$

The spot size of the diffracted light is then

$$R^2 \frac{(2\pi)^2}{k_2^2 HL} \quad ,$$

while the spot size of the incident light is HL . We have then, from Eq. (3.36),

$$\frac{I_2}{I_1} = \frac{k_2^2}{4} (\epsilon_1 p_{44} S_4)^2 W^2 F_1^2 \quad . \tag{3.39}$$

The factor F_1 is the sin x/x pattern due to the mismatch Δk_x and the acoustic beam width W . Similarly to the calculation of Δk_y , it can be shown that

$$\Delta k_x = k_s \Delta\phi \quad ,$$

where $\Delta\phi$ is the angle spread of the k_s for a finite width acoustic beam. In terms of the acoustic power density in the crystal, which is given by

$$P_{ac} = \frac{1}{2} C_{44} |S_4|^2 v_s \quad , \tag{3.40}$$

where C_{44} is the elastic constant and v_s is the shear wave velocity, Eq. (3.39) becomes

$$\frac{I_2}{I_1} = \frac{k_0^2 n_1^6 p_{44}^2}{2 C_{44} v_s} P_{ac} W^2 \left(\frac{\sin k_s \Delta\phi \frac{W}{2}}{k_s \Delta\phi \frac{W}{2}} \right)^2 \quad , \tag{3.41}$$

where n_1 is the index of refraction seen by the diffracted light, $\epsilon_1 = n_1^2$. The diffracted light by shear waves is a function of the photoelastic constants and the power distribution of the acoustic waves inside the crystal. In addition, Bragg diffraction by shear waves predicts the important polarization effect for both acoustic waves and the light wave as we have discussed. In the next chapter, we utilize this polarization effect to probe the acoustic birefringence in YAG and to determine experimentally the orientation and ellipticity of shear waves generated from transducers.

CHAPTER IV

EXPERIMENTAL RESULTS

4.1 INTRODUCTION

In this chapter the important properties of shear wave diffraction theory will be demonstrated experimentally. Optical probing techniques by longitudinal waves have been used to probe the acoustic energy distributions in solids,[39] to measure the intrinsic acoustic attenuation of delay media,[15] and to study the acoustic harmonics generation and the effect of finite amplitude elastic waves in solids.[49] Utilizing the unique characteristics of shear wave diffraction, the optical probing techniques will be extended to map the shear wave energy distribution, to measure the shear wave attenuation, to determine the conversion efficiency of the longitudinal to shear waves mode convertor, to study the shear wave bonds, to probe the acoustic birefringence in solids and to determine experimentally the orientation and the ellipticity of the shear wave generated from an experimental transducer.

4.2 EXPERIMENTAL APPARATUS

The experimental arrangement, shown schematically in Fig. 4.1, is similar to that used in longitudinal diffraction experiments.[3] A Ne-He cw gas laser (6328 Å Spectra Physics Model 130) was used for the incident light source. The quarter wave plate is oriented such that the laser beam, after passing through the quarter wave plate, becomes circularly polarized. The polarization of the incident light can then be rotated to any angle with respect to the crystal axes of the sample by a rotatable polarizer.

The crystal bonded with an acoustic wave transducer used for the diffraction experiment is mounted in a re-entrant cavity, which is used as a step-up transformer to increase the electric field across the transducer and hence improve the conversion efficiency as discussed in

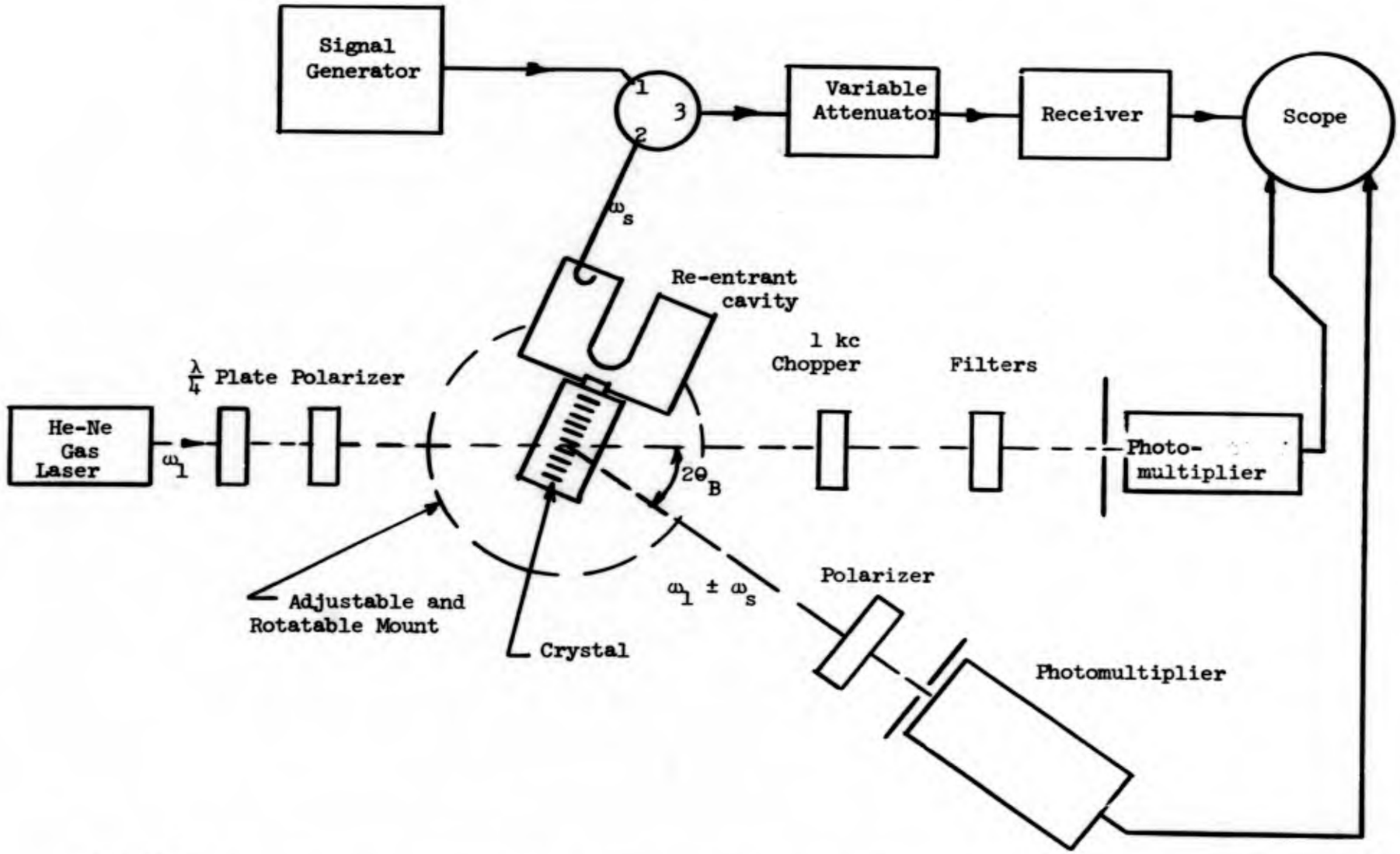

FIG. 4.1--Experimental arrangement for Bragg diffraction of light by shear waves.

Chapter II. The cavity and crystal are mounted on a rotary table which permits rotation in a horizontal plane and three-dimensional translation. This table allows very accurate adjustments of the position of the crystal with respect to the laser beam.

The microwave signal fed into the cavity comes from a signal generator which can be pulsed or 1 Kc square-wave modulated. The reflected power from the cavity is detected by a standard heterodyne receiver and displayed on an oscilloscope. Standard pulse echo measurements are performed to determine the properties of the acoustic waves in the crystal and to measure the conversion efficiency of the transducer.

A photomultiplier is used to detect the diffracted light. Since the light diffracted by shear waves is crossed polarized with respect to the transmitted and scattered light, a crossed polarizer is put in front of the photomultiplier to improve the signal-to-noise ratio. The same photomultiplier with calibrated neutral density filters is used to measure the intensity of the transmitted light.

4.3 OPTICAL PROBING OF ACOUSTIC WAVES

As shown in Eq. (3.41), the intensity of the diffracted light is a function of the proper photoelastic constants P_{mn}, the acoustic power density P_{ac} and the distance W that the incident light travels in the acoustic beam. In the following sections, we will apply the shear wave diffraction theory to map the shear wave column in the YAG mode converter discussed in Section 2.3, to measure the shear wave attenuation in YAG and to determine the mode conversion efficiency.

4.3.1 Acoustic Beam Mapping

The measured time separation between successive echoes, which agrees with the calculated value of the round trip time through the crystal obtained by applying the values for V_s and V_ℓ to the appropriate portions of the wave path in Fig. 2.10, is one of the evidences that there is a shear wave column generated in the YAG mode convertor. A second experimental verification of the existence of a shear wave column is by the Bragg diffraction technique. The change in polarization of

the diffracted light is one of the unique characteristics of the shear wave diffraction. In addition to the polarization change the incident angle θ_B for shear waves is different from that for longitudinal waves due to the difference in velocities.

The incident angle θ_B measured from the acoustic wave front, which is in the (001) plane, can be calculated from Eq. (3.25) to be

$$\theta_B = \sin^{-1}\left(\frac{0.6328 \times 10^{-4}}{2 \times 3.36 \times 10^{-4}}\right) = 5.4^\circ$$

at a frequency of 1461 Mc. The Bragg angle is measured from outside the crystal so that there is a factor equal to the index of refraction difference in the value calculated from Eq. (3.25). The diffracted beam deviates from the transmitted beam by $2\theta_B$ and has its polarization rotated 90° with respect to that of the incident beam.

Figure 4.2 shows the result of mapping the shear wave acoustic column by a 0.020 inch-diameter laser beam probe, which was mechanically scanned transversely across the column at a cross section located near the excitation end of the YAG mode converter. The calculated curve shows scattered light intensity from a constant density column having an elliptical cross section with a major axis of 0.136 inches, which is the value predicted from the geometry of Fig. 2.10 when the input longitudinal wave circular column has a 0.080 inch diameter. The calculated curve also takes into account the effect of the finite incident beam diameter. We see good agreement between the experimental and calculated cross section of the shear wave column.

4.3.2 Shear Wave Attenuation and Mode Conversion Efficiency Measurements In YAG[45]

Bragg diffraction of light by injected acoustic waves has been used to measure the intrinsic attenuation of longitudinal waves in quartz.[15] It was shown that the technique will avoid the difficulties of the pulse echo method of measuring acoustic attenuation. We have measured the shear wave attenuation in YAG and hence have determined the mode conversion

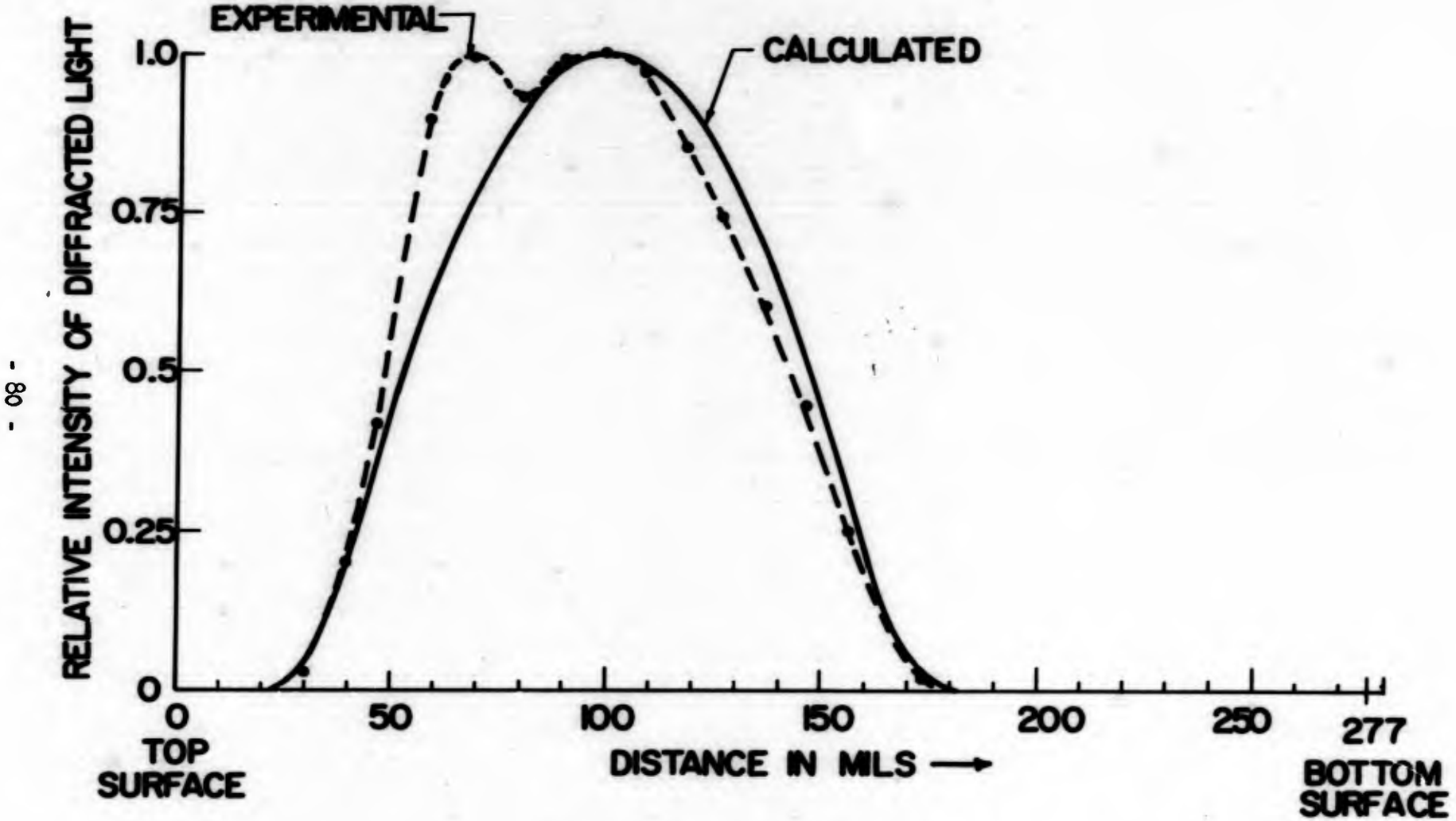

FIG. 4.2--Shear wave beam profile.

efficiency of the mode converter. We have also discovered the inhomogeneity of the acoustic attenuation in the YAG sample. The inhomogeneity caused by a strained center core as shown in Fig. 4.3 can easily be seen under the polariscope.

By introducing the attenuation constant α in the acoustic power density,

$$P_{ac} = (P_{ac})_0 e^{-2\alpha z} \tag{4.1}$$

where $(P_{ac})_0$ is the acoustic power density at $z = 0$, we can determine α by measuring the diffracted powers at two points along the direction of the acoustic wave propagation, i.e.,

$$\frac{I_2(z_1)}{I_2(z_2)} = e^{-2\alpha(z_1-z_2)} \tag{4.2}$$

The procedure for measuring the ratio of the diffracted power ratio in order to obtain the attenuation in the YAG converter will now be described. Instead of using cw power, we excite the ZnO transducer with a 2 μsec rf pulse. The sample will contain a 2 μsec acoustic pulse traveling with the shear wave velocity while in the shear wave region. The incident light with a 0.020 inch beam diameter is applied to the shear wave region. As the acoustic pulse passes through the incident beam, part of the incident light will be diffracted and registered in the photomultiplier. Figure 4.4 shows the typical diffracted light registered in the photomultiplier. The first pulse in the oscillogram represents the first pulse of the diffracted light as discussed previously. The second pulse is the diffracted signal from the return acoustic wave pulse which is reflected back from the far end of the sample. The third pulse in the oscillogram is for calibration purposes so that we can measure the intensities in dB by a variable attenuator. By moving the incident beam or the crystal itself along the propagation direction of the shear waves and measuring the change in the intensity of the first diffracted light pulse, we can accurately measure the attenuation constant.

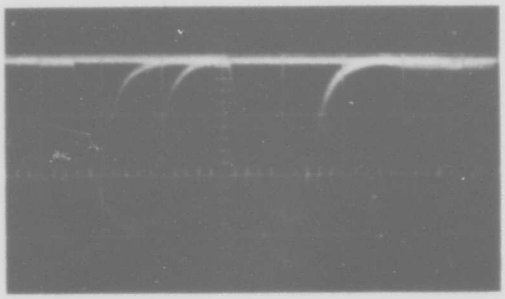

1 μsec/cm

FIG. 4.4--Echoes for diffracted light. The first pulse indicates the intensity of light diffracted by the forward acoustic pulse. The second pulse is by the reflected acoustic pulse. The third pulse is for the calibration purpose.

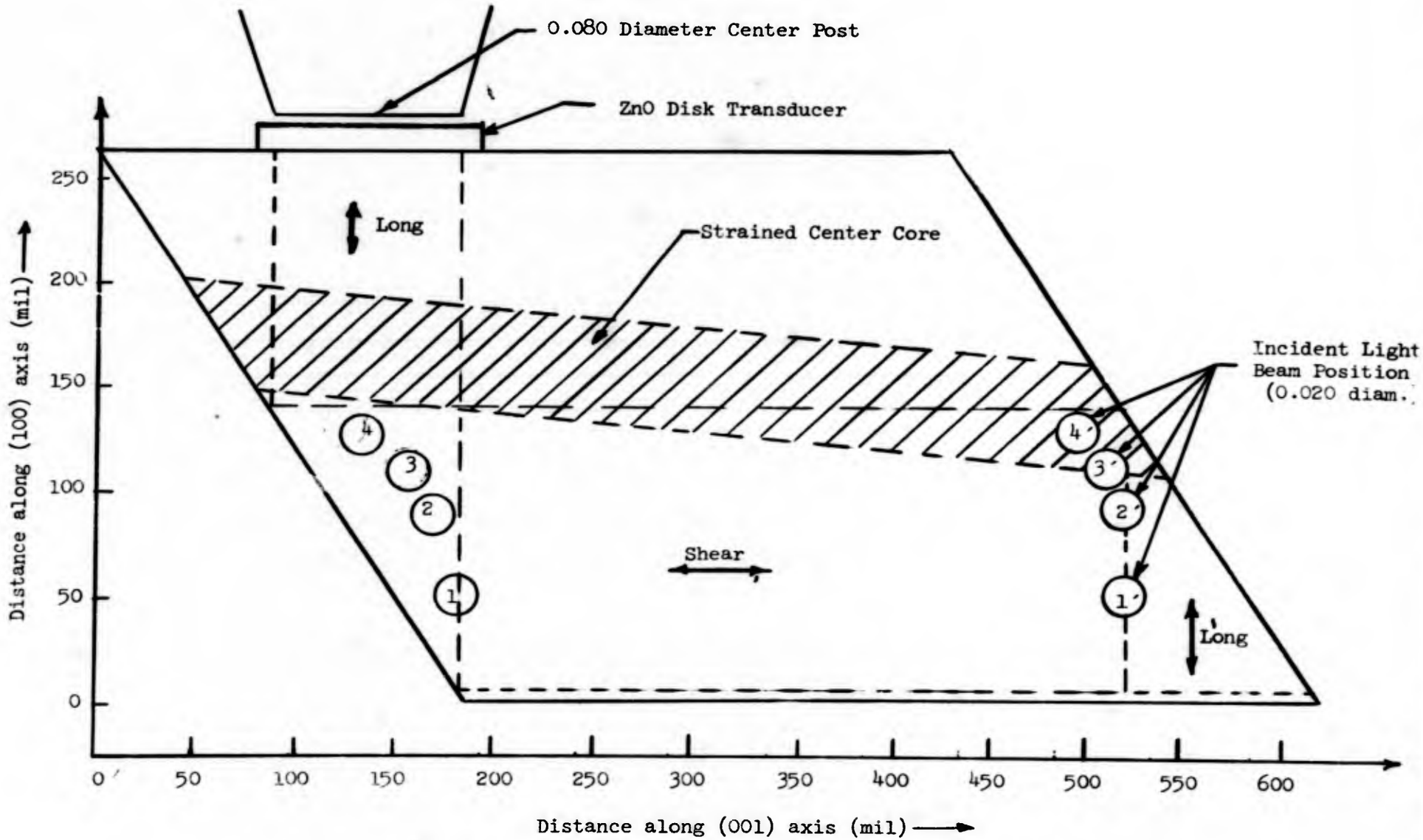

FIG. 4.3--Attenuation measurement in the YAG converter.

The attenuation measurements in the YAG converter are taken along four different paths in the crystal as indicated by (1) - (1′), (2) - (2′), etc., in Fig. 4.3. The measured values for the shear wave attenuation in YAG along the different paths are: along (1) - (1′), α = 0.4 dB/cm ; along (2) - (2′), α = 0.32 dB/cm ; along (3) - (3′), α = 2.79 dB/cm ; along (4) - (4′), α = 2.5 dB/cm . The inhomogeneity of the attenuation constants in the crystal suggested by the experimental results is verified by observing the residual strain in the crystal under the polariscope as shown in Fig. 4.5. The sample was cut such that the strained core of the grown crystal, extended partially into the region of the shear wave column, as indicated in Fig. 4.3. This explains the increase in the attenuation as the shear waves propagate closer to the strained region. This also explains the asymmetry in the measured curve for the diffracted light in Fig. 4.2.

The mode conversion efficiency for the longitudinal waves converted to shear waves or vice versa at the inclined surface of the YAG converter can be determined by measuring the difference in intensities between the first and second diffracted echoes as shown in Fig. 4.4. It should be noted that the difference in intensities between the first and second diffracted echoes includes twice the shear wave attenuation from the laser spot to the inclined surface, plus twice the mode conversion loss and twice the longitudinal attenuation from the inclined surface to the bottom surface of the crystal. By subtracting the attenuation from the shear wave and the longitudinal wave region, the mode conversion loss will readily be obtained. Although no exact value of longitudinal wave attenuation has been measured by Bragg diffraction techniques, the reported elastic Q of longitudinal waves at microwave frequencies is within the same order of magnitude of the shear wave elastic Q .[38] Assuming the same attenuation for both longitudinal and shear waves, the measured mode conversion loss from longitudinal to shear waves or vice versa was less than 0.1 dB, which agrees closely to the predicted value.

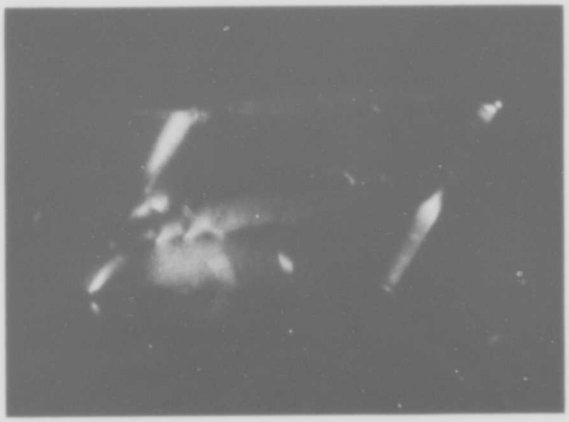

STRAINED CENTER CORE
IN THE YAG CONVERTER SEEN
UNDER A POLARISCOPE

FIG. 4.5--YAG converter under polariscope.

It is worth mentioning that in spite of the different shear wave attenuation values measured along the four paths in Fig. 4.3, the total loss in each path (which is due to twice the shear wave attenuation, twice the longitudinal wave attenuation, four times the mode conversion losses, and the loss in the transducer bond) remains constant and equal to the value measured (12 dB) by pulse echo techniques.

4.3.3 Photoelastic Constants of YAG

As shown in Eq. (3.45), the intensity of the diffracted light at the Bragg condition is

$$\frac{I_2}{I_1} = \frac{k_0^2}{2} \frac{n_1^6 P_{44}^2}{C_{44} v_s} W^2 P_{ac} \quad , \qquad (4.3)$$

where k_0 is the wave number of the incident light in vacuum; n_1 is the index of refraction seen by the diffracted light; P_{44} is the appropriate photoelastic constant; C_{44} is the elastic constant; v_s is the shear wave velocity; W is the width of the acoustic column; and P_{ac} is the acoustic power density in the crystal. For convenience, we have defined a C-factor which is the ratio of the diffracted light intensity to the incident light in dB for a 1 mw total acoustic power in a circular beam in the crystal:

$$\text{C-factor} = 10 \log \left(\frac{8\pi}{\lambda_0^2} \frac{n_1^6 P_{44}^2}{C_{44} v_s} \right) \quad . \qquad (4.4)$$

The C-factor for longitudinal waves in various materials has been tabulated.[50] The C-factor for the shear waves in the [100] YAG rod was measured to be -53 dB. The photoelastic constant P_{44} is then calculated from Eq. (4.4) to be 0.075.

4.4 STUDIES OF SHEAR WAVE BONDS

In this section we are concerned with a new technique of the optical probing to study the acoustic bonds between delay media. It is essential to have efficient acoustic bonds to cement the transducers on delay media or to join two delay media together. Using an indium bond[18] the bond loss for longitudinal waves has been reduced to a few dB, while the efficient bonds for shear waves are much more difficult to make. Recently an optical bond technique[51] has been reported to have transmitted 90 percent of the incident shear waves at 1.5 GHz. Except for the optical bonds, the transmission efficiencies of the "cement" bonds are still poor at microwave frequencies. We have studied several bonding materials such as polystyrene, phenyl benzoate and phenyl salicylate, which are found to be convenient cements for bonding the shear wave transducers on the delay media. The transmission efficiencies of these shear wave bonds depend on the thickness of the bond and the surface conditions of the bonded media. Instead of discussing in detail the technique of shear wave bonds, we will present a technique to measure the bonding efficiency. It has been shown in Sections 4.2 and 4.3 that the Bragg diffraction technique is a convenient probe to measure the acoustic intrinsic attenuations and to map the acoustic energy distribution. This technique combined with the optical heterodyne detection[52] can be used as a standing wave detector for acoustic waves to measure the magnitudes and phases of the reflection and transmission coefficients of acoustic bonds.

As shown in Fig. 4.6(a) two delay media are bonded together by a shear wave bond of thickness ℓ . An incident shear wave pulse is propagating from the left. The quantities we are interested in are the reflection coefficient at $Z = 0$ and the transmission coefficient at $Z = \ell$. Using a transmission line analogy, we can consider the shear wave bond between two delay media as a small section of lossy transmission line with the characteristic impedance corresponding to the acoustic impedance in the bond sandwiched between two half infinite transmission lines as shown in Fig 4.6(b). The impedances of the half infinite lines correspond to the acoustic impedances of the delay media.

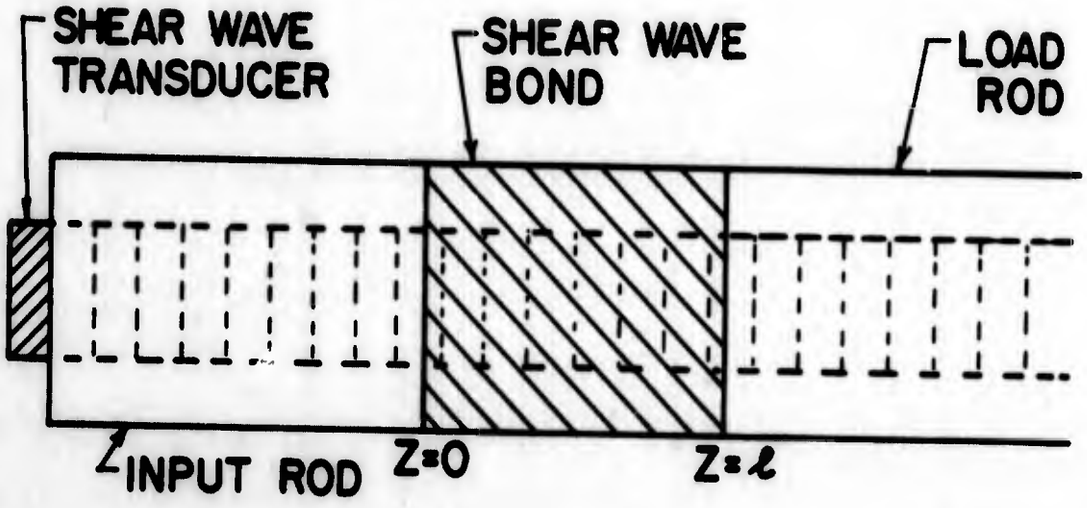

(a) Shear wave bond

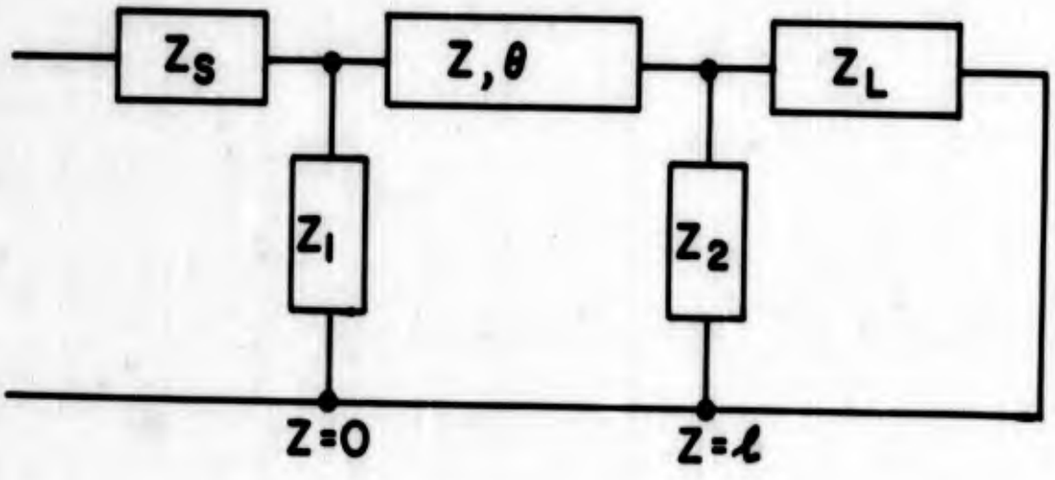

(b) Transmission line model

FIGURE 4.6

The acoustic loss in the bond is taken into account by the Q of the lossy transmission line section. Also shown in Fig. 4.6(b) are two shunt impedances Z_1 and Z_2 due to any slippage losses of the particle displacement at the interfaces $Z = 0$ and $Z = \ell$ between the bond and delay media. The reflection and transmission coefficients are calculated in Appendix A.

We have demonstrated the measurement of reflection and transmission coefficients of phenyl benzoate shear wave bonds by the optical probing technique. A thin layer of phenyl benzoate was used to bond two x-cut $LiNbO_3$ rods. One of the x-cut $LiNbO_3$ rods was used as an input rod and mounted in a re-entrant cavity. A 2 μsec pulse of shear waves was then excited in the input rod. The shear wave pulse propagated with the shear wave velocity toward the phenyl benzoate bond. Part of the incident shear wave pulse was reflected by the shear wave bond and became a reflected pulse. The remaining shear wave was attenuated in the medium of the shear wave bond and transmitted into the load rod as the transmitted pulse. The intensities of the reflected and transmitted pulses are the amptitudes of the reflection and transmission coefficients, respectively. The laser beam was incident in the input rod close to the bond with proper Bragg condition. The intensities of the diffracted light by the input and reflected shear wave pulses were measured. It has been shown in Chapter III that the intensity of the diffracted light is directly related to the acoustic power. Neglecting the small attenuation in $LiNbO_3$ at the frequency range 1 to 2 GHz, the ratio of the reflected and input shear wave pulses is equal to the reflection coefficient R. Similarly, by moving the laser in the load rod, we measured the diffracted light by the transmitted pulse and consequently the transmission coefficient T. Figure 4.7 shows the reflection and transmission coefficients of phenyl benzoate shear bond between two x-cut $LiNbO_3$ rods as a function of shear wave frequencies. As the acoustic frequency is varied, the effective acoustic thickness of the bond varies. Analogous to transmission line theory the reflection coefficient becomes zero at the frequencies when the thickness of the bond is integer half wavelengths. Since the bond is lossy, there is no zero reflection coefficient

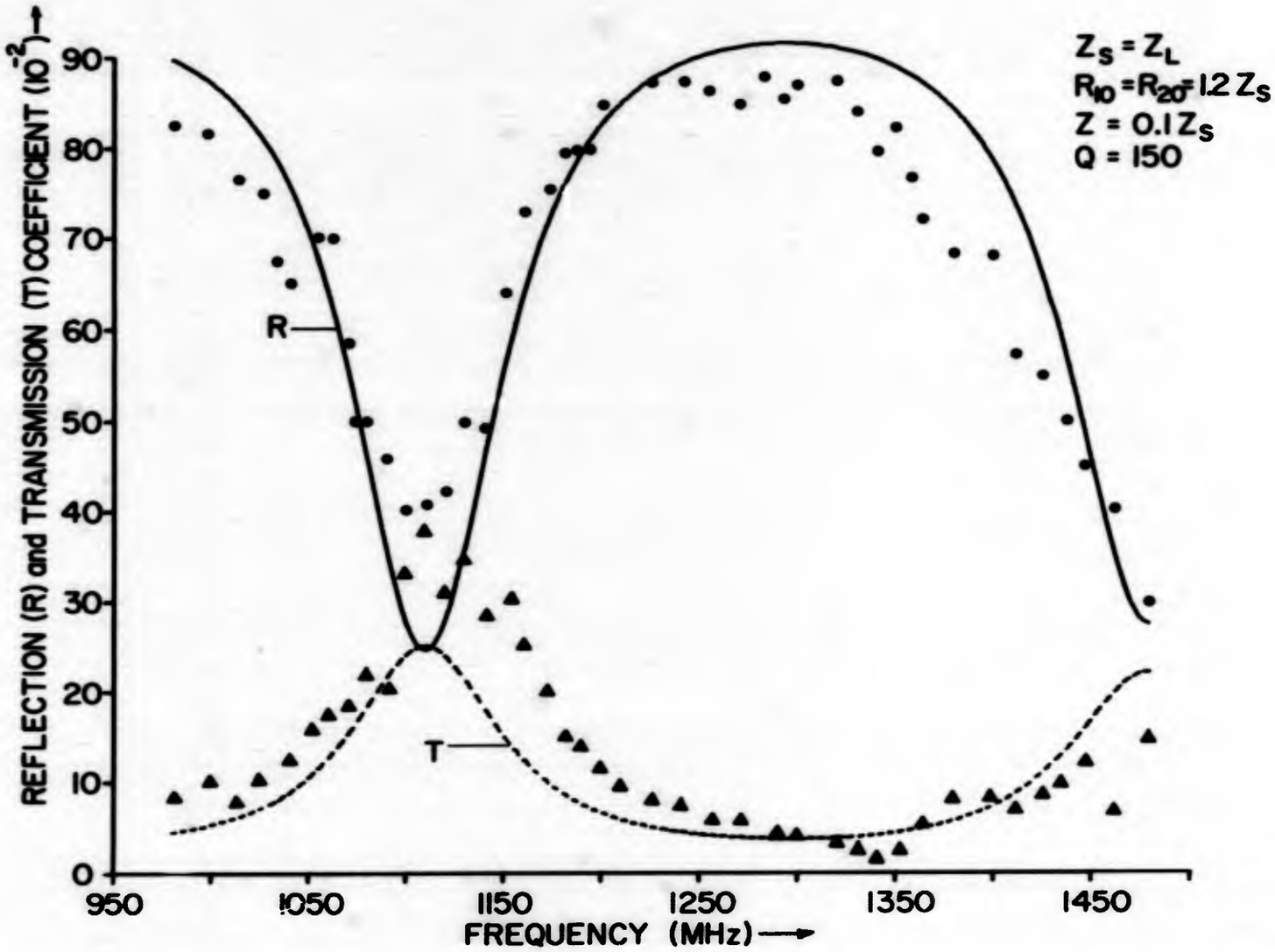

FIG. 4.7--Reflection and transmission coefficients of phenyl benzoate shear wave bond vs frequencies.

even at the frequencies of exact integer half wavelength. For the case shown in Fig. 4.7 the thickness of the bond at f = 150 Mc is 1-1/2 wavelength of the shear wave in the bond. The transmission is about 0.35 and the reflection coefficient is 0.4. In order to match the measured curves of the reflection and transmitted coefficients by the transmission line model, the slippage losses of shear waves at the interfaces between the bond and the rods have to be included in addition to the bond loss. There is no information available on the velocity, the impedance and the attenuation of shear waves in phenyl benzoate. It is also difficult to measure the physical thickness of the bond. The calculated curve in Fig. 4.7 is obtained by adjusting three parameters: the acoustic impedance, Q of the bond and the resistance representing the slippage losses at the interfaces, in the theory given in Appendix A, to fit the measured curves. A self-consistent picture based on this calculation is as follows. The ratio of the acoustic impedance and the rod impedance $Z_0/Z_1 = 0.1$. The Q of the shear wave bond is about 150 and the resistance of the friction loss at the interfaces is about 1.2 times the $LiNbO_3$ impedance. It should be noticed that the losses at the interfaces are very large for the shear wave bonds.

4.5 ACOUSTIC BIREFRINGENCE IN YAG PROBED BY A LASER BEAM[53]

In this section we will discuss the essential characteristics of diffracted light by a column of transverse elastic waves at frequency ω_s propagating along the [110] axis of a [110] oriented YAG rod. The reason for choosing the [110] axis as the acoustic beam axis, which is one of three pure mode axes in cubic crystals, will become clear later. As shown in Fig. 4.8, the coordinates are chosen so that x_1 , x_2 and x_3 are parallel to the cubic edges, η coincides with the [110] axis, ξ is parallel to the [110] axis, and ζ is parallel to the [001] axis. The transverse acoustic wave propagating along the η-axis can be characterized as in Eq. (8) using only two strain components, S_4 and S_6 . Here the subscripts 4 and 6 refer to the rotated coordinate system, so that S_4 represents the wave for which particle motion is

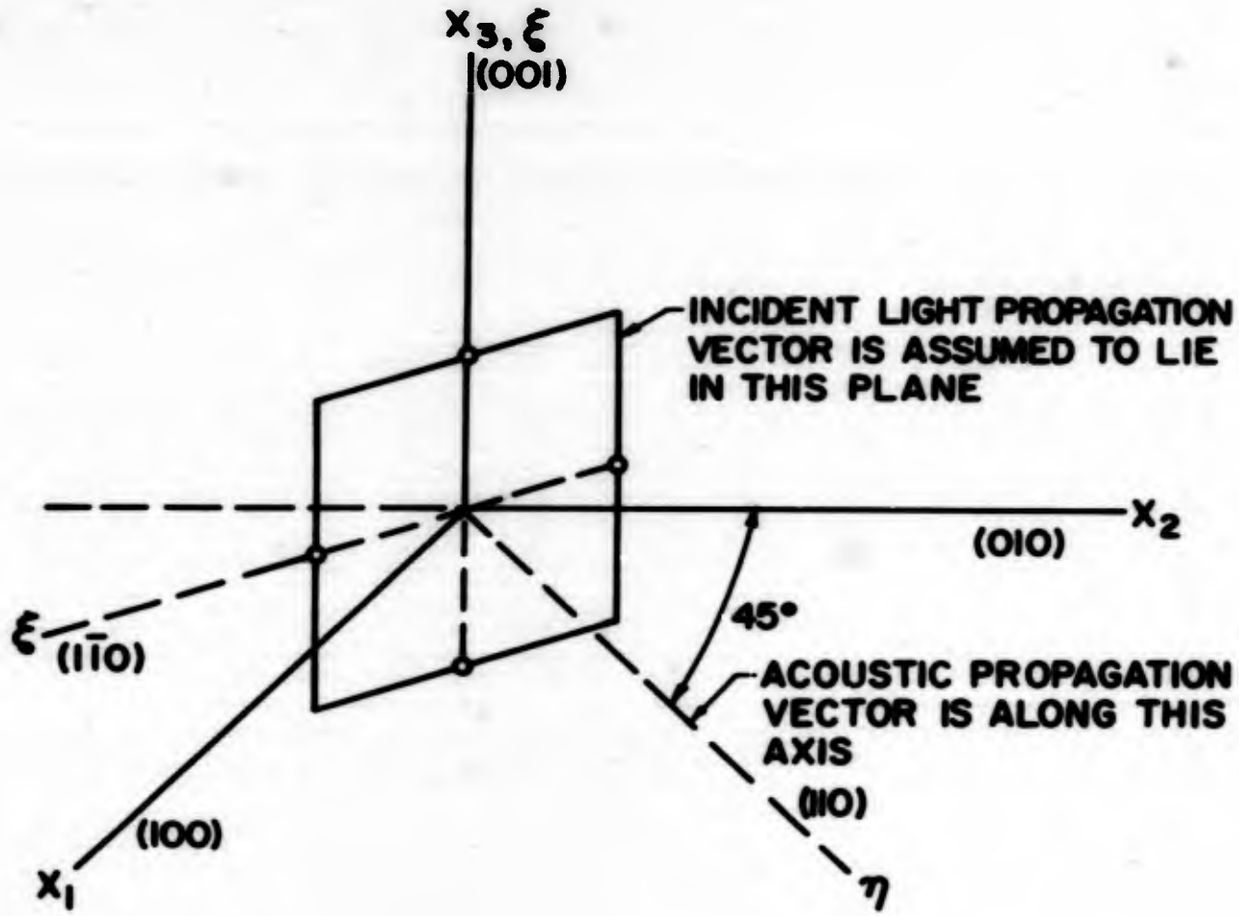

FIG. 4.8--Rotated axes for the [110] YAG rod.

along the ζ - axis, and S_6 corresponds to the wave for the partial motion along the ξ - axis. The state of polarization of the transverse acoustic wave is specified by the amplitudes and phases of S_4 and S_6.

The [110] oriented YAG rod is acoustically birefringent when shear waves propagate along the rod axis. Analogous to optical birefringence, acoustic birefringence will occur if the waves involving S_4 and S_6 travel at different velocities in the crystal. Due to relative phase changes as the waves propagate along the crystal, the polarization of the composite shear wave undergoes periodic changes of ellipticity and orientation. In a [110] YAG rod the velocity difference for shear waves polarized along [100] and [110], respectively, is 8320 cm/sec.[38] In addition to the small acoustic birefringence, YAG has excellent acoustic and optical properties, and we find that it also has large photoelastic constants for shear waves.

An input linearly-polarized shear wave was generated from a y-cut $LiNbO_3$ disk transducer of 5 mils thickness and 100 mils diameter, cement-bonded to the [110] YAG rod with phenyl benzoate. The y-cut $LiNbO_3$ transducer is capable of efficient generation of shear waves at microwave frequencies. The conversion efficiency from electromagnetic to acoustic energies can be as high as -12 dB at 1 GHz.

Figure 4.9 shows the changes of shear wave polarization as the wave propagates along the [110] YAG axis. The transducer was oriented so that the shear wave started out linearly polarized at 45° to the orthogonal [001] and $[1\bar{1}0]$ axes. As the waves progress, the polarization transforms progressively into right-hand circular, cross-polarized linear, left-hand circular, and back to linear with the original orientation. These transformations proceed with a "beat" wavelength λ_B which is inversely proportional to the velocity difference of the [001] and $[1\bar{1}0]$ shear wave components.

A small-diameter laser beam was passed through the crystal, with incident angle equal to the Bragg angle measured with respect to the wave front of the shear wave. Part of the incident light is diffracted at the Bragg angle. As discussed in Section 3.4, the strain component which is normal to the propagating direction of the light beam contributes

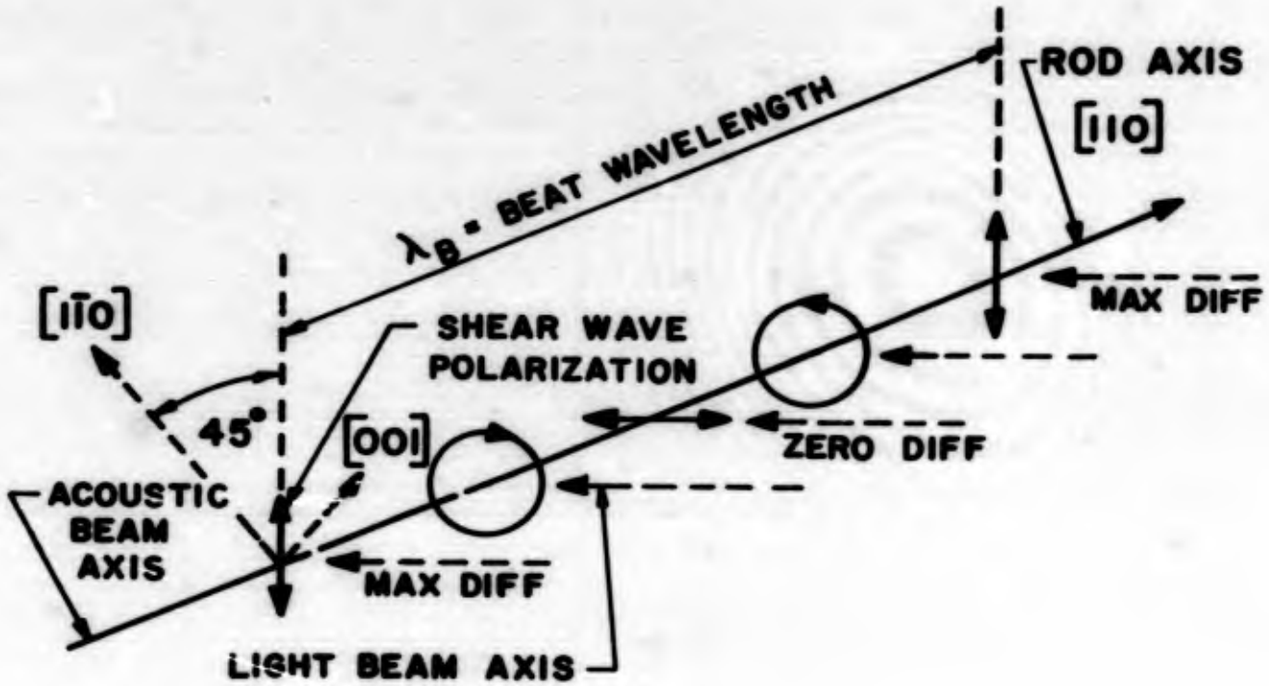

$$\lambda_B \sim \Delta v^{-1}$$

FIG. 4.9--Acoustic birefringence in [110] oriented YAG rod.

to the diffracted light, and the strain component parallel to the light-beam axis produce no diffraction in a photoelastically isotropic media. The laser beam was mechanically scanned along the axial direction of the sample. As indicated in Fig. 4.9, the diffracted light intensity is maximum when the incident light axis is perpendicular to the linearly-polarized shear wave, and decreases to zero as the incident light becomes aligned with the linearly-polarized shear wave. Intermediate intensities of diffracted light are produced at intermediate locations. The intensity of the diffracted light, as a function of the incident laser beam position along the rod axis, is sinusoidal with a wavelength equal to the beam wavelength λ_B .

The calculation of the diffracted light intensity as a function of the incident laser position along the [110] axis of the YAG rod is similar to the calculation in Section 3.4. The photoelastic tensor $[p'_{mn}]$ suitable for the [110] oriented YAG crystal can be obtained by rotating the photoelastic tensor $[p_{mn}]$ given in Eq. (3.28) by 45° with respect to the x_3 - axis. The indicatrix, which describes the optical properties of the strained [110] YAG rod by S_4 and S_6 , is found from Eq. (3.30a) to be

$$B_1 (\xi^2 + \eta^2 + \zeta)^2 + 2\Delta B_4 \eta\zeta + 2\Delta B_6 \eta = 1 \qquad (4.5)$$

with

$$\Delta B_4 = p_{44} S_4$$

$$\Delta B_6 = \frac{1}{2} (p_{11} - p_{12}) S_6 \quad .$$

The dielectric tensor $[\epsilon']$ of the strained [110] oriented YAG rod, which relates the induced displacement vector in the crystal to the

incident field component, is then

$$[\epsilon'] = \begin{pmatrix} \epsilon_1 & 0 & 0 \\ 0 & \epsilon_1 & 0 \\ 0 & 0 & \epsilon_1 \end{pmatrix} - \epsilon_1^2 \begin{pmatrix} 0 & \frac{P_{11}-P_{12}}{2}\hat{S}_6 & 0 \\ \frac{P_{11}-P_{12}}{2}\hat{S}_6 & 0 & P_{44}\hat{S}_4 \\ 0 & P_{44}\hat{S}_4 & 0 \end{pmatrix} \tag{4.6}$$

where ϵ_1 is the unstrained dielectric constant of YAG. The second term of Eq. (4.6) contributes the polarization dipole for the diffracted light.

The induced displacement vector D_2 as discussed in Section 3.4 is determined by the propagation direction of the incident light and the dielectric ellipsoid with the dielectric tensor given in Eq.(4.6). Because the Bragg angle θ_B is essential for phase but negligible for amplitude calculations, we assume that the incident light is along the $\xi\ \zeta$ plane (the acoustic wave front) in the following calculation for the amplitude of D_2 .

For the case that the incident light is along the ξ - axis [$1\bar{1}0$ axis], D_2 is found to be

$$\begin{pmatrix} D_{2\eta} \\ D_{2\zeta} \end{pmatrix} = \begin{pmatrix} 0 & -\epsilon_1^2 P_{44}\hat{S}_4 \\ \epsilon_1 P_{44}\hat{S}_4 & 0 \end{pmatrix} \begin{pmatrix} E_{1\eta} \\ E_{1\zeta} \end{pmatrix} . \tag{4.7}$$

The incident light propagating along the $[1\bar{1}0]$ axis of the crystal has two polarizations. According to Eq. (3.39), the maximum diffracted light for the incident light along the $[1\bar{1}0]$ axis with vertical or horizontal polarization is

$$I_{1\bar{1}0} = \frac{k_2^2}{4} (\epsilon_1 P_{44} S_4)^2 W^2 I_1 \quad , \tag{4.8}$$

where I_1 is the intensity of the incident light and W is the width of the acoustic beam.

Similarly, for the case that the incident light is along the ζ axis [001 axis] we will find the D_2 for the diffracted light to be

$$\begin{pmatrix} D_{2\xi} \\ D_{2\zeta} \end{pmatrix} = \begin{pmatrix} 0 & -\epsilon_1^2 \frac{P_{11}-P_{12}}{2} \hat{S}_6 \\ -\epsilon_1 \frac{P_{11}-P_{12}}{2} S_6 & 0 \end{pmatrix} \begin{pmatrix} E_{1\xi} \\ E_{1\zeta} \end{pmatrix} \tag{4.9}$$

and the intensity is

$$I_{001} = \frac{k_2^2}{4} \left(\epsilon_1 \frac{P_{11}-P_{12}}{2} S_6 \right)^2 W^2 I_1 \quad , \tag{4.10}$$

where I_1 indicates the intensity of the incident light propagating along the [001] axis with either vertical or horizontal polarization.

For the case that the incident light is incident at an azimuthal angle ϕ with respect to the ξ - axis [$1\bar{1}0$ axis] in the ξ-ζ plane as shown in Fig. 4.10, the D_2 for the diffracted light is found to

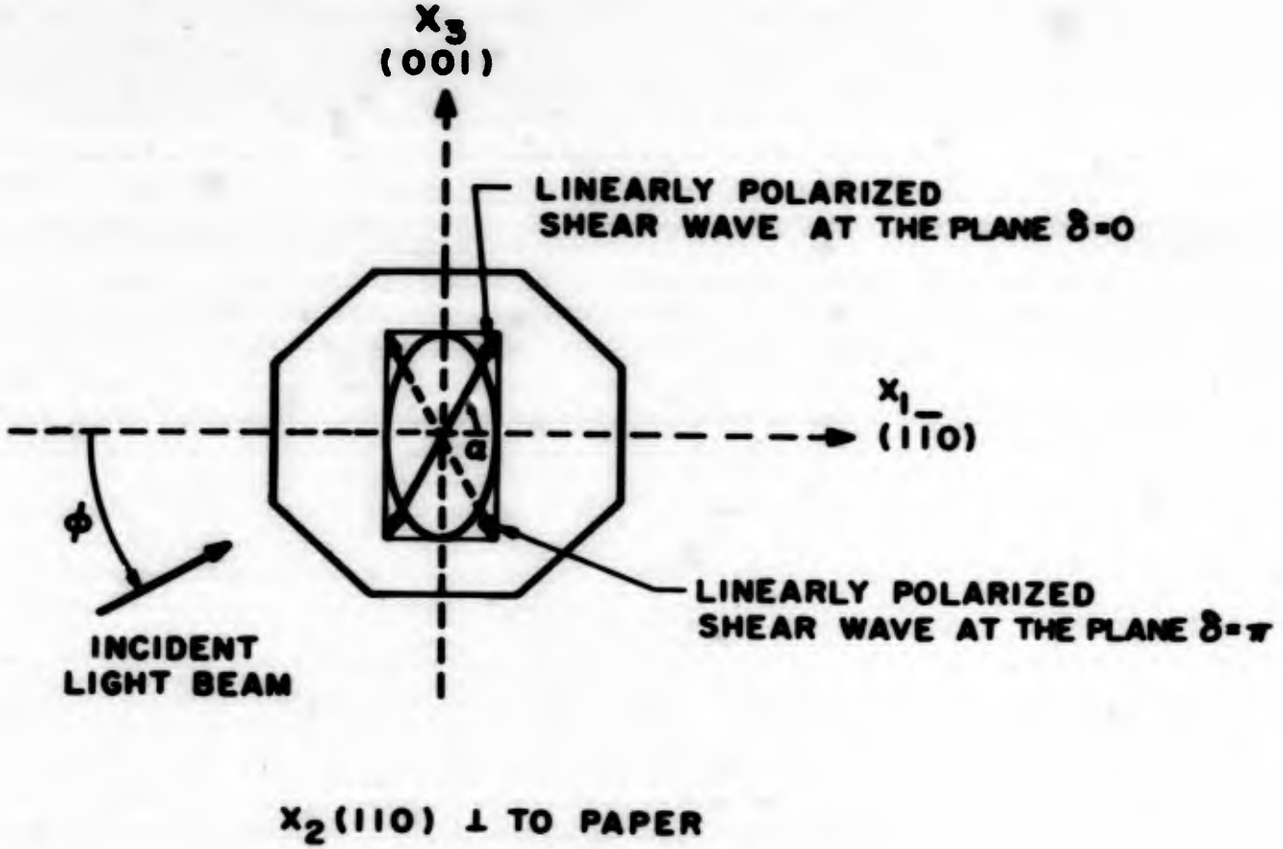

FIG. 4.10--[110] YAG rod with an input linear shear wave polarized at an angle α with respect to the $[1\bar{1}0]$ axis.

be

$$\begin{pmatrix} D_{2\zeta} \\ D_{2\zeta'} \end{pmatrix} = \begin{pmatrix} 0 & \Delta\varepsilon_4 \cos\phi - \Delta\varepsilon_6 \sin\phi \\ \Delta\varepsilon_4 \cos\phi - \Delta\varepsilon_6 \sin\phi & 0 \end{pmatrix} \begin{pmatrix} E_{1\zeta} \\ E_{1\zeta'} \end{pmatrix} \tag{4.11}$$

with

$$\Delta\varepsilon_4 = \epsilon_1^2 P_{44} \hat{S}$$

$$\Delta\varepsilon_6 = -\epsilon_1^2 \frac{P_{11}-P_{12}}{2} \hat{S}_6 \quad ,$$

where ζ' is the rotated axis from the ζ axis by an angle ϕ . If the incident light is vertically polarized and has only a component $E_{1\zeta'}$, D_2 of the diffracted light becomes horizontally polarized and has

$$D_{2\eta} = (\Delta\varepsilon_4 \cos\phi - \Delta\varepsilon_6 \sin\phi) E_{1\zeta'} \tag{4.12}$$

and

$$\Delta\varepsilon_4 = -\epsilon_1^2 p_{44} \hat{S}_4$$

$$\Delta\varepsilon_6 = -\epsilon_1^2 \frac{P_{11}-P_{12}}{2} \hat{S}_6 \quad .$$

Due to acoustic birefringence S_4 and S_6 have different phases as the shear waves propagate along the rod axis. Let

$$\hat{S}_6 = |\hat{S}_6| \, e^{i\delta_1}$$

$$\hat{S}_4 = |\hat{S}_4| \, e^{i\delta_2} \tag{4.13}$$

where

$$\delta_1 = \frac{2\pi}{\Lambda_1} \, y$$

$$\delta_2 = \frac{2\pi}{\Lambda_2} \, y \, , \tag{4.14}$$

where y is the distance measured along the [110] axis, Λ_1 and Λ_2 are acoustic wavelengths of S_6 and S_4 . Taking into account the polarization change in Eq. (4.58), we have the intensity of the diffracted light from Eq. (3.36);

$$I_2 = I_{001} \cos^2 \phi + I_{1\bar{1}0} \sin^2 \phi - \sqrt{I_{001} I_{1\bar{1}0}} \sin 2\phi \cos \delta \, \frac{\sin \frac{\pi a}{\Lambda_B}}{\frac{\pi a}{\Lambda_B}} \, , \tag{4.15}$$

where $1/\Lambda_B = 1/\Lambda_1 - 1/\Lambda_2$, and $\delta = 2\pi y/\Lambda_B$ is the phase difference in S_4 and S_6 at any point y along the rod axis. In (4.15) a is the diameter of the laser beam, and

$$\frac{\sin \frac{\pi a}{\Lambda_B}}{\frac{\pi a}{\Lambda_B}}$$

is the effect of the finite laser beam diameter on the diffracted light resulting from the averaging over the distance a along the rod axis; I_{001} [given in Eq. (4.10] is the intensity of the diffracted light when the incident light is along the [001] axis and $\phi = 0^\circ$; $I_{1\bar{1}0}$ [given in Eq. (4.8)] is the diffracted light intensity when the incident light is along the $[1\bar{1}0]$ axis and $\phi = 90^\circ$.

Both I_{001} and $I_{1\bar{1}0}$ are readily measurable quantities. For each incident azimuthal angle ϕ , Eq. (4.15) predicts a sinusoidal curve with beam wavelength λ_B determined by the condition $\delta = 2\pi$ if the laser beam diameter a is smaller than the beat wavelength λ_B .

Figure 4.11 shows a recorder plot of the intensity of the diffracted light as a function of the axial position y of the laser beam probe. The experimental results agree with the theoretical prediction. The measured beat wavelength Λ_B is in excellent agreement with the calculated values based on the published values of the velocities.[38] Figure 4.12 shows the measured and calculated values of Λ_B as a function of frequency. The beat wavelength has a value of 10 mils at the frequency of 1.3 GHz. This is a convenient value for the construction of acoustic quarter wave plates, which are the acoustic analog of familiar optical quarter wave plates. These [110] YAG quarter wave plates have been constructed and demonstrated for new microwave devices.[54,55] The beat wavelength measurement also provides an excellent method of accurately measuring the velocity difference of two shear waves in a crystal.

4.6 EXPERIMENTAL DETERMINATION OF THE ORIENTATION AND ELLIPTICITY OF SHEAR WAVES

The optical probing of shear waves diffraction has another important application. It provides a method to determine the ellipticity and orientation of the polarization of shear waves at any point inside the delay medium. On occasions it has been necessary to know exactly the ellipticity and orientation of the polarization of the shear waves generated by experimental transducers. Unusual pulse echo measurements

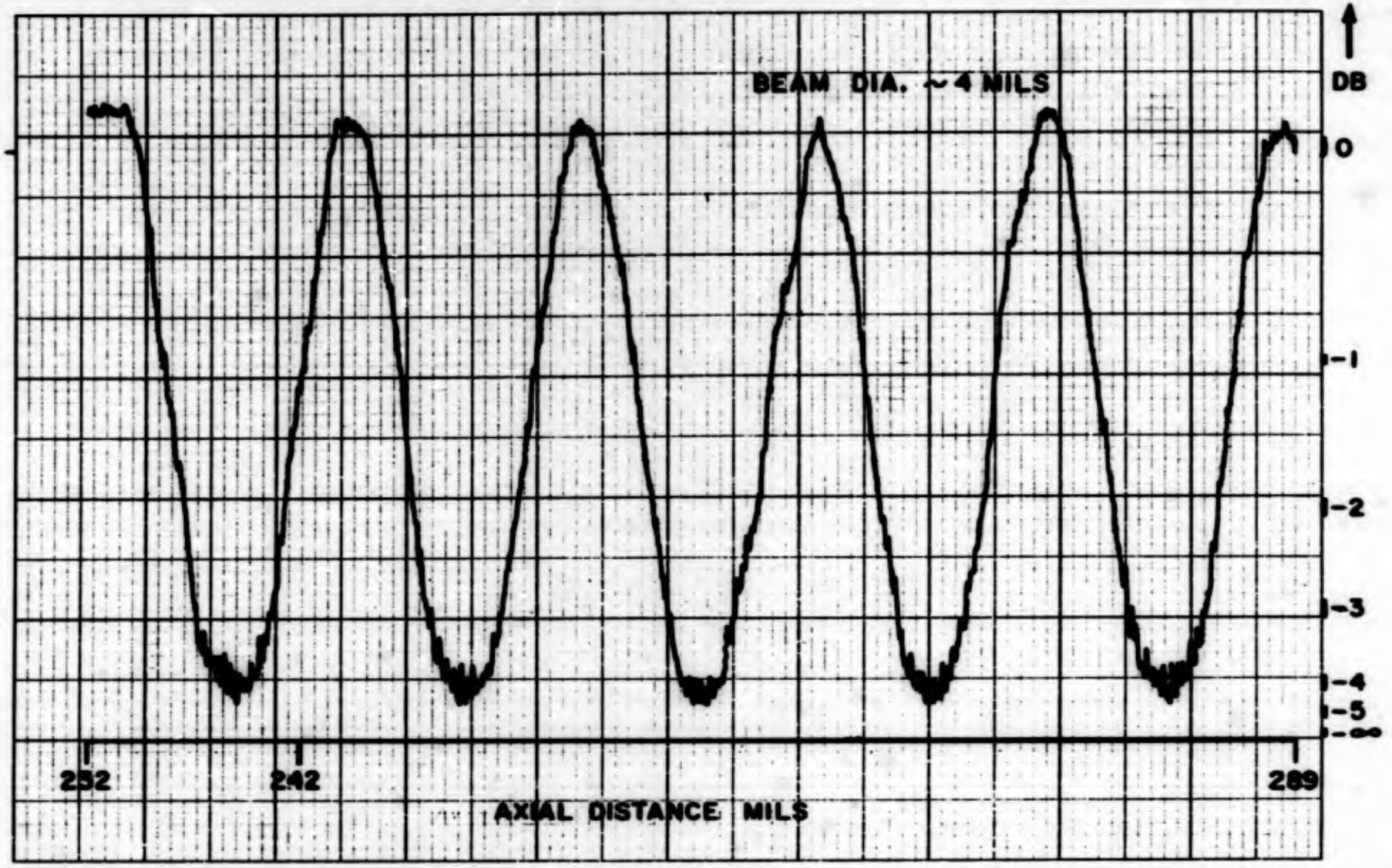

FIG. 4.11--Record plot of the intensity of the diffracted light as a function of axial position along the [110] oriented YAG rod.

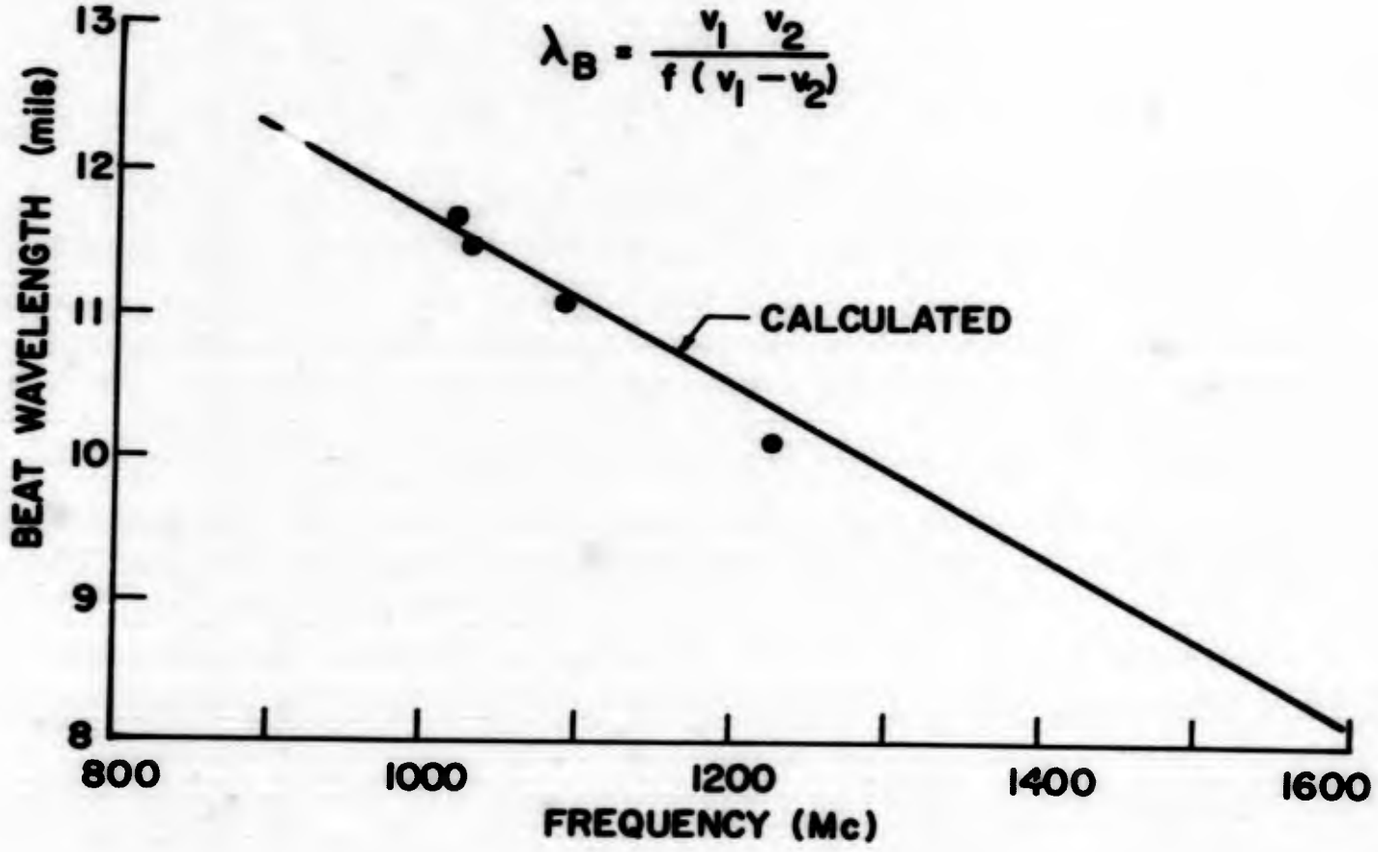

FIG. 4.12--Beat wavelength vs frequencies.

give only the indirect information of the shear wave polarization of the shear waves and is difficult to interpret.

The scheme can be used to detect the shear wave polarization either in acoustically isotropic or anisotropic media. For the purpose of illustrating the technique, consider an input shear wave linearly polarized at an arbitrary angle α with respect to the [110] axis as indicated by the solid line in Fig. 4.10. The strain of the linearly polarized shear wave has two components, $|\hat{S}_4| = |S| \sin \alpha$ and $|S_6| = |S| \cos \alpha$, when $|S|$ is the strain amplitude. The intensity of the diffracted light as a function of azimuthal angle ϕ for the linear polarized shear wave can be easily obtained from Eq. (4.15) by letting $\sigma = 0$ and

$$\frac{\sin \frac{\pi a}{\Lambda_B}}{\frac{\pi a}{\Lambda_B}} = 1 \quad ,$$

i.e.,

$$I_2(\phi) = \left(\sqrt{I_{001}} \cos \phi - \sqrt{I_{1\bar{1}0}} \sin \phi \right)^2 \tag{4.16}$$

with

$$\frac{I_{011}}{I_{1\bar{1}0}} = \left(\frac{p_{11}-p_{12}}{2p_{44}} \right)^2 \cot^2 \alpha \quad . \tag{4.17}$$

By knowing the photoelastic isotropic factor of the crystal $p_{11}-p_{12}/2p_{44}$ (the condition for photoelastic isotropy is $p_{11}-p_{12}/2p_{44} = 1$) , one should be able to determine the polarization angle α by measuring the ratio of $I_{011}/I_{1\bar{1}0}$.

This technique has been applied to determine the particle displacement direction of x-cut $LiNbO_3$ transducers. In Section 2.3 we have shown that there are two orthogonal shear wave modes excited in a x-cut transducer. One has larger electromechanical coupling constant. As shown in Table I, the velocity of the large coupling mode is 4.9×10^5 cm/sec and the direction of the particle displacement is (0: -0.636 : 0.771) which has a 40° angle measured from the z-axis. In order to check the calculation experimentally, the shear wave diffraction technique was used to probe the linear shear waves generated from a x-cut $LiNbO_3$ disk transducer bonded to a [100] oriented YAG crystal. The [100] oriented YAG crystal is photoelastically isotropic so that the intensity of the diffracted light as a function of ϕ is a direct measurement of the polarization of the shear wave. According to Eq. (4.16), and (4.17), the intensity of the diffracted light as a function of ϕ is proportional to $\cos^2(\phi-\alpha)$, where α is the polarization angle. We have measured the diffracted intensities as a function of ϕ from the linearly polarized shear waves in a [100] YAG rod. The x-cut $LiNbO_3$ disk transducer, which was bonded to the YAG rod and generated the linearly polarized shear wave in the rod, has been x-rayed to determine the orientation of the y- and z-axes with respect to the crystal axes of the [100] YAG rod. The measured polarization angle in 40° from the z-axis as predicted in the calculation.

If the medium is acoustically birefringent, the state of the polarization of the shear wave will change periodically with a periodicity of Λ_B along the rod axis. For each azimuthal incident angle ϕ the intensities of the diffracted light as given in Eq. (4.15) vary sinusoidally as the phase δ changes along the rod axis. The situation is analogous to the standing wave pattern of electromagnetic waves in a waveguide with a mismatched impedance . The light beam works exactly as the standing wave probe does. Based on the same analogy, we can measure the standing wave ratio R as the ratio of

the maximum to the minimum diffracted light intensities by moving the laser beam along the rod axis for a particular azimuthal incident angle ϕ . The standing wave ratio measurement has experimental advantages over the absolute intensity measurement in that the effect of input power fluctuations can be minimized.

Figure 4.13 shows the experimental results of standing wave ratio R together with the calculated value. The calculated curve is for the case that $\alpha = 47^{\circ}$, $(p_{11}-p_{12})/2p_{44} = 0.3$ and $a = 4.7$ mils . The location of maximum value of R can be found to be

$$\tan \phi = \frac{p_{11}-p_{12}}{2p_{44}} \tan \alpha \quad . \qquad (4.18)$$

By knowing the anisotropic factor $(p_{11}-p_{12})/2p_{44}$, the orientation of the linearly polarized shear wave can be determined by Eq. (4.18). Equation (4.18) can also be used to find the anisotropic factor by injecting a shear wave with known polarization. For the [110] YAG sample, the input linearly polarized shear wave was generated by a y-cut $LiNbO_3$ transducer. The orientation was determined by x-ray. It was checked that $\alpha = 47^{\circ}$ with respect to the [110] axis. The anisotropic factor of YAG is calculated to be 0.3. The P_{44} of YAG was found in Section 3.4.3 to be in the order of 0.074; $(p_{11}-p_{12}/2$ is then 0.022.

It is obvious that the incident beam diameter will affect the resolution of the standing wave pattern. Figure 4.14 shows the standing wave ratio R as a function of incident beam diameter a when the incident angle $\phi = 45^{\circ}$ with respect to the $[1\bar{1}0]$ axis. This provides more evidence that the theory and experiments are in good agreement.

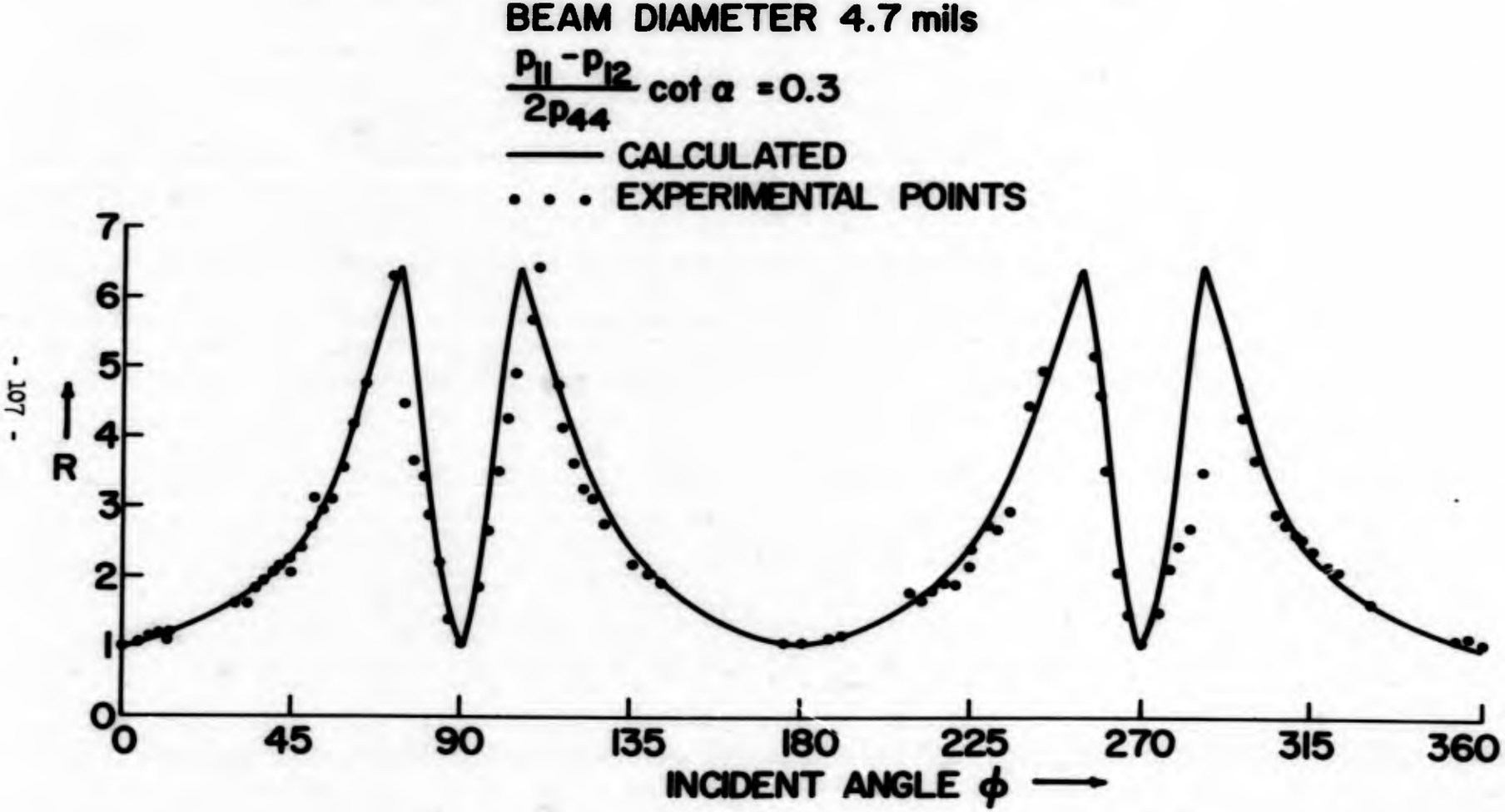

FIG. 4.13--Standing wave ratio (R) vs azimuthal angle ϕ .

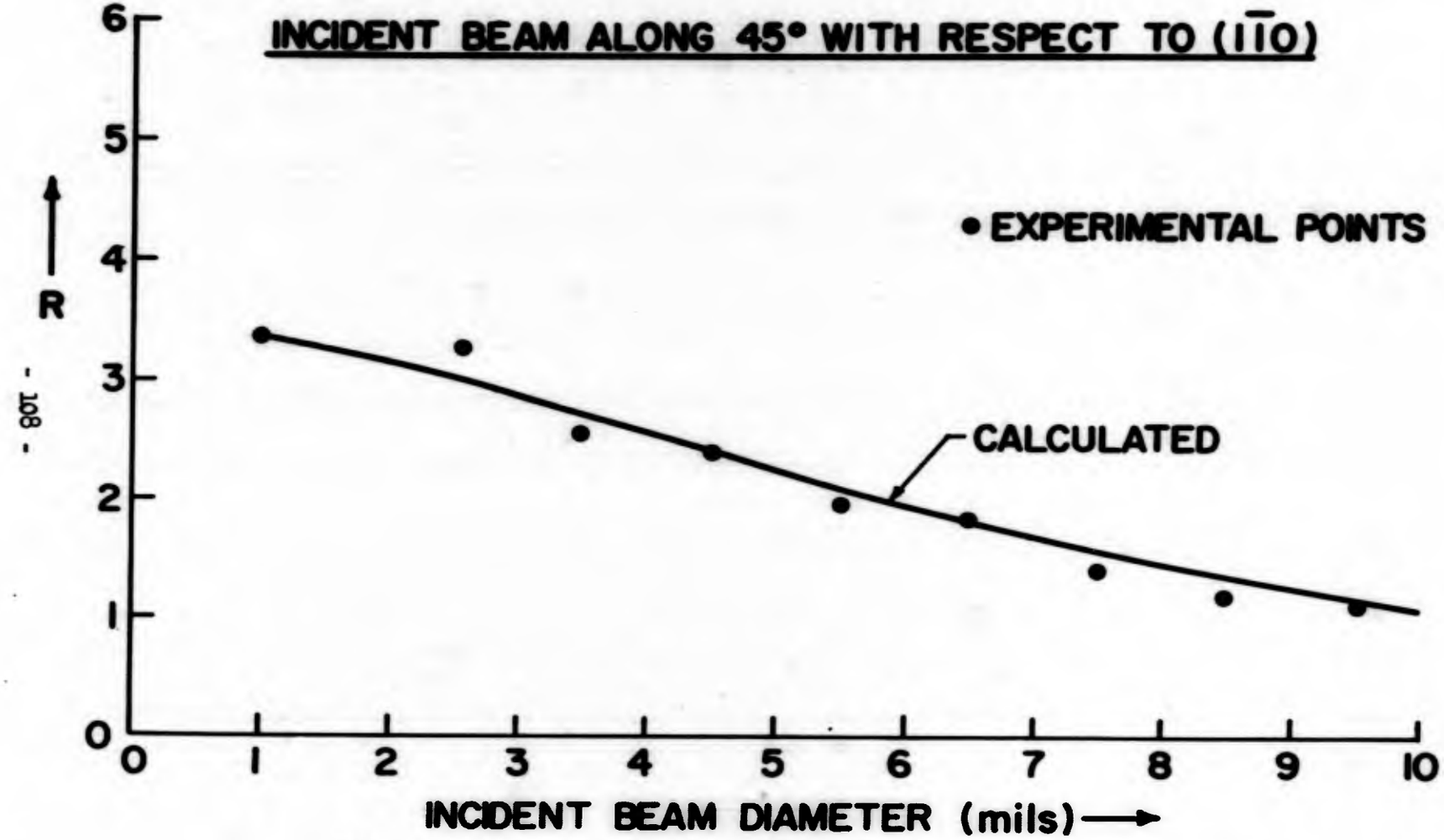

FIG. 4.14--Standing wave ratio (R) vs diameter of the incident light.

CHAPTER V

CONTINUOUS DEFLECTION OF LASER BEAMS

5.1 INTRODUCTION

The development of methods of high speed, high resolution optical beam deflection has recently received considerable attention. Most of the high speed optical scanning devices employ the electro-optic effect[56] or acousto-optic effect.[57] Fowler, et. al.,[58] have recently reviewed the methods of laser beam deflection and the limitations of the present systems. It is clear that optical deflection systems do not yet compete with the electron beam for high speed scanning and recording of information. It is therefore worthwhile to consider alternative methods for the continuous scanning of light beams.

Acousto-optic light deflectors which are capable of continuously deflecting a light beam through 200 spot diameters have been reported by Korpel, et al.[59] The light deflection was achieved by Bragg scattering of light from a steerable 30 Mc sound column. The principles of acousto-optic deflection of light waves has been reviewed recently by Gordon.[59] "Phase matching" is a basic requirement of this process, and requires that the vector sum of the wave vectors of these waves with finite diameters add to zero, i.e., $\underset{\sim}{k}_2 = \underset{\sim}{k}_1 \pm \underset{\sim}{k}_s$ as discussed in Chapter III. Here $\underset{\sim}{k}_s$ is the wave vector for the sound wave, $\underset{\sim}{k}_1$ and $\underset{\sim}{k}_2$ are the wave vectors for the incident light and diffracted light, respectively. The "phase matching" condition of Bragg diffraction is required both in isotropic crystals and in anisotropic crystals. Most of the acousto-optic deflectors have employed Bragg diffraction in isotropic crystals. Isotropic deflectors are limited in the range of the deflection angle and in the resolution of the devices. In this chapter we present a method of laser beam deflection based on the Bragg scattering of light from a sound wave in a birefringent crystal. In sapphire we have been able to deflect a laser beam continuously through an angle of 4° by varying a single electric parameter – the frequency of the sound

wave. In Section 5.2, we will discuss and compare the schemes of acousto-optic deflectors using both isotropic and anisotropic crystals. In Section 5.2.3, calculations on the deflected beam in sapphire will be given to check the experimental results. In Section 5.2.4, we will discuss the extension of these types of acousto-optic deflectors.

5.2 SCHEMES OF ACOUSTO-OPTIC DEFLECTORS USING BRAGG DIFFRACTION TECHNIQUES

5.2.1 In Isotropic Media

As discussed in Chapter III, the basic requirement for the first order Bragg diffraction are the conservations of frequencies and wave vectors:

$$\omega_2 = \omega_1 \pm \omega_s \tag{5.1}$$

$$\underset{\sim}{k}_2 = \underset{\sim}{k}_1 \pm \underset{\sim}{k}_s \tag{5.2}$$

where the subscripts s, 1, and 2 stands for the acoustic wave, the incident and diffracted lights, respectively. In isotropic media, where $|k_1| = |k_2|$ as discussed in Section 3.3, Eq. (5.2) can be represented by an isosceles triangle as shown in Fig. 3.2. The Bragg angle θ which is the angle of the incident and diffracted lights measured from the acoustic wave front because

$$\sin\theta = \frac{|k_s|}{2|k_1|} = \frac{\lambda_1}{2V_s} f \quad , \tag{5.3}$$

[as shown in Eq. (3.25)]. In (5.3) the acoustic wavelength $\Lambda = \frac{V_s}{f}$ has been substituted for $|k_s| = \frac{2\pi}{\Lambda}$. The scattering angle measured from the transmitted beam is 2θ.

If the acoustic wave and the incident wave are infinite plane waves, the condition in (5.2) or (5.3) in isotropic crystals has to be satisfied exactly in order to observe the diffracted light. In the cases of finite acoustic and light beams, the phase matching condition is not so critical. We have calculated the amplitude of the far field diffraction for a rectangular light beam and finite acoustic beams as a

function of phase mismatch. The results, as shown in Eq. (3.27a), contained the well known $\frac{\sin x}{x}$ pattern due to the phase mismatching. The angular spread of the diffracted beam is approximately given by

$$\Delta\alpha = \frac{2\pi}{k_2 L} \quad , \tag{5.4}$$

where $\Delta\alpha$ is the angular spread and L is the diameter of the incident light. The effect of the finite width of the acoustic beam W to the intensity of the diffracted light given by

$$\left(\frac{\sin k_s \Delta\phi \frac{W}{2}}{k_s \Delta\phi \frac{W}{s}}\right)^2$$

in Eq. (3.45) can be represented by a wave vector of the acoustic wave which is no longer well defined but rather has an angular spread given by

$$\Delta\phi = \frac{2\pi}{k_s W} \quad . \tag{5.5}$$

In (5.5), k_s is the acoustic wave vector at frequency f_s.

Cohen and Gordon[39] have considered the case of scattering with longitudinal acoustic beams of finite width and have measured the angular distribution or the far field diffraction pattern of the acoustic beams by rocking the crystal in the incident plane. They have come to the same results for the angular spread of the acoustic wave vector.

For the purpose of beam deflection by acoustic Bragg diffraction in an isotropic crystal, we want to deflect the diffracted beam through an angle $\Delta\theta$ by changing the magnitude or direction or both of k_s as shown in Fig. 5.1. The parameter N, which describes the resolution of deflection devices, is defined by

$$N = \frac{\Delta\theta}{\Delta\alpha} \quad , \tag{5.6}$$

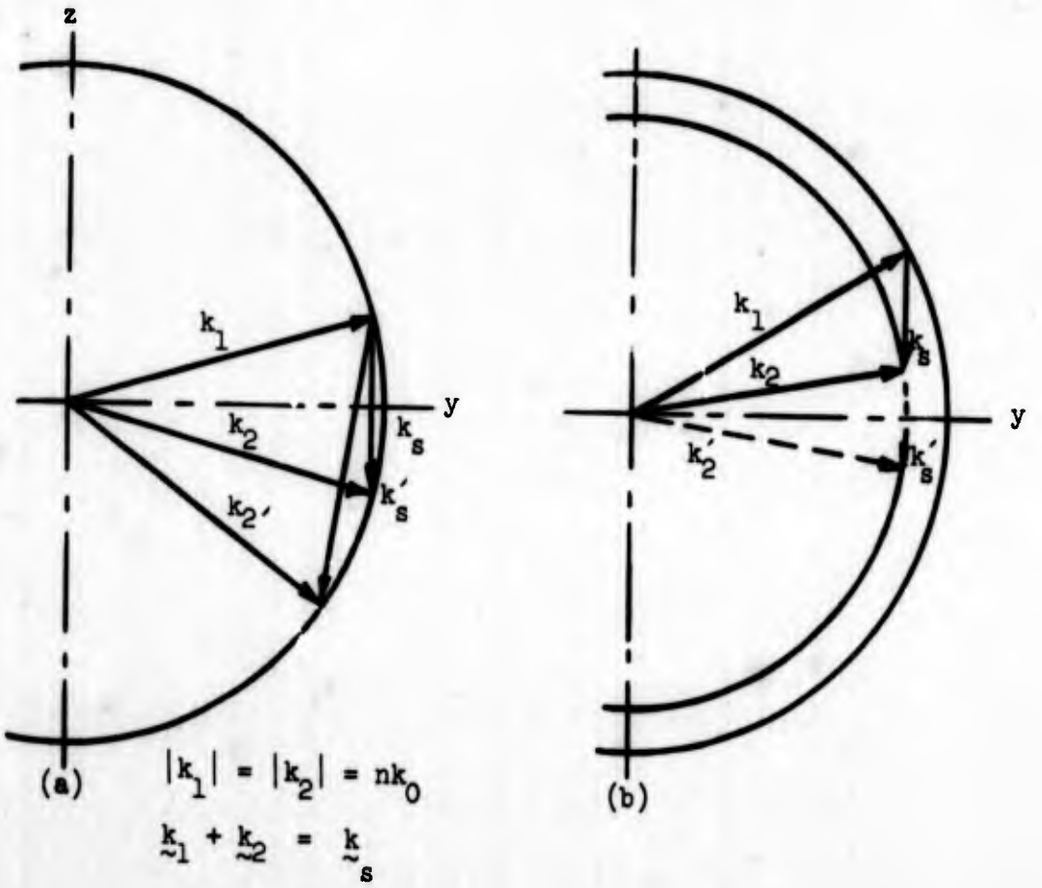

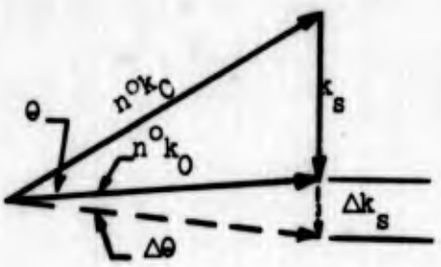

(c)

$n^o = n^o - B$

$k_s = k_0(n^{o2} - n^{o2})^{\frac{1}{2}}$

$\approx k_0(2n^o B)^{\frac{1}{2}}$

FIG.12(a)-The wave vector locus and orientation for acoustic deflection –
(a) an isotropic crystal,
(b) an anisotropic crystal,
(c) the vector triangle for an anisotropic crystal for the special case where the acoustic wave vector is tangent to the locus of the wave vector for the extraordinary ray. The optic axis is normal to the plane of the figure. A preferable orientation would be realized if the optic axis was in the plane of the figure and parallel to the acoustic wave vector.

where $\Delta\theta$ is the angle through which the diffracted light can be varied, and $\Delta\alpha$ given in Eq. (5.4) is the angular spread of the diffracted beam. If the acoustic frequency is varied by an amount Δf the change in the diffracted angle can be found from Eq. (5.3):

$$\Delta\theta = \frac{\lambda \Delta f}{v_s \cos\theta} \quad . \tag{5.7}$$

The number of resolvable spots then, by (5.7), (5.4), and (5.6), is

$$N = \frac{L \Delta f}{v_s \cos\theta}$$

$$= \Delta f \tau \tag{5.8}$$

where

$$\tau = \frac{L}{v_s \cos\theta}$$

is the transit time of the acoustic wave across the light beam of a diameter.

The maximum deflection angle $\Delta\theta$ in which the acoustic frequencies can be varied and the intensity of diffracted light still remains within -4 dB of the maximum intensity, is determined by the equivalent acoustic wave angular spread $\Delta\phi$ given in (5.5). By letting $\Delta\theta = \Delta\phi$, i.e., the maximum deflection angle $\Delta\theta$ is equal to the angular spread of the acoustic wave vectors, we find that

$$\Delta f = \frac{v_s \cos\theta}{W} \frac{\Lambda}{\lambda} \quad , \tag{5.9}$$

where Λ is the acoustic wavelength and λ is the optical wavelength inside the medium.

Gordon,[57] in his review paper of acousto-optical deflection and modulation devices, has used the same result to point out that in order to increase the resolvable spots N , a narrow acoustic beam and a wide light should be used in deflectors.

Bragg deflectors using isotropic crystals have the following limitations. In order to maintain the condition $|k_2| = |k_1|$ in isotropic media, we see from Fig. 5.1a that to increase the angle of the output light beam it is necessary to change both the direction and magnitude of the acoustic wave vector or to narrow the acoustic beam diameter. In the past this has been accomplished in two ways: (1) by acoustic beam steering, whereby the acoustic column is launched from a transducer array which generated an acoustic beam with a direction that varies with frequency, and (2) by using a focused acoustic column such that the acoustic beam contains k_s vectors convering a cone of direction. The acoustic "beam steering" technique has been reported by Koppel, et al.[59] The technique becomes unattractive when the frequency is increased because of the difficulty of fabricating the transducer array. In the second system the light is scattered by a different portion of the acoustic column as the Bragg angle is varied. The fraction of acoustic power available for deflection is equal to N^{-1}, and therefore the system becomes inefficient as N, the resolvable spots, is increased.

5.2.2 In Anisotropic Media

The formulation of Bragg diffraction of light by acoustic waves in anisotropic media has been given by Dixon.[17] The basic requirements for the diffraction process still remain the conservations of frequencies and of wave vectors as given in Eqs. (5.1) and (5.2). For the cases that the polarization of the diffracted light is the same as that of the incident light, the Bragg condition can be reduced the same as that in isotropic crystals [Eq. (5.3)].

However, when the polarization of the diffracted light differs from that of the incident light, the optical birefringence requires $|k_1| \neq |k_2|$ in order to satisfy the phase matching for the lights in the anisotropic crystal. Bragg diffraction with a change in polarization involves the photoelastic constant p_{44}, p_{55} or p_{66} if the diffraction is from shear waves. The physical picture is similar to the isotropic crystal case as discussed in Chapter IV. Later, a simple description of the diffraction mechanism will be given in connection with the calculation of the intensity of the diffraction light.

The Bragg diffraction with the change in polarization can also result from longitudinal waves if some of the photoelastic constants such as

p_{41} , p_{42} are not zero in the crystal. Dixon[17] has derived and verified experimentally the relation for the incident and diffracted angles as a function of acoustic frequency and indices of refraction in both quartz and sapphire.

For the purpose of light deflection we wish to consider the special case of light diffraction by a shear wave column in an uniaxial crystal. The wave vectors of the acoustic wave, the incident and diffracted lights are illustrated in Fig. 5.1b. We have chosen the magnitude of the acoustic wave vector such that it is tangent to the wave vector surface for the extraordinary ray. The sound wave and the diffracted light are normal to each other. From the triangle of Fig. 5.1c we see that

$$k_s \cong k_0\sqrt{2n^oB} \quad , \tag{5.10}$$

where $k_s = 2\pi f_0/v_s$ is the acoustic wave vector at the center frequency f_0 , $k_0 = 2\pi/\lambda_0$ is the optical wave vector in vacuum and B is the birefringence of the crystal. The value of B can range from $n^o - n^e$ for light waves traveling in a plane normal to the optical axis to zero for light waves traveling in a plane containing the optic axis. It is clear from Fig. 5.1b and 5.1c that a change in the direction of the deflected light vector from $\underset{\sim}{k}_2$ to $\underset{\sim}{k}_2'$ can be obtained by a change in the magnitude of the acoustic wave vector from k_s to k_s' . Thus we can deflect the optical beam by varying the frequency of a well-collimated acoustic beam which remains fixed in direction.

The maximum deflection angle $\Delta\theta_m$ and the number of resolvable spots for this deflection system can be found as follows. The basic mechanism for Bragg diffraction by acoustic waves either in anisotropic or isotropic crystals is identical. We can use the same approach as discussed in Chapter III to calculate the intensity of the diffracted light. For simplicity, a two-dimensional case will be considered here. As shown in Fig. 5.2, a column of shear waves with a width W is propagating along the x_1-axis of an uniaxial crystal. Let the shear waves be represented by the strain S_5 (omit the $e^{j\omega_s t}$ term)

$$S_5 = S_0\, e^{-j(k_s+\Delta k_s)\, x_1} \tag{5.11}$$

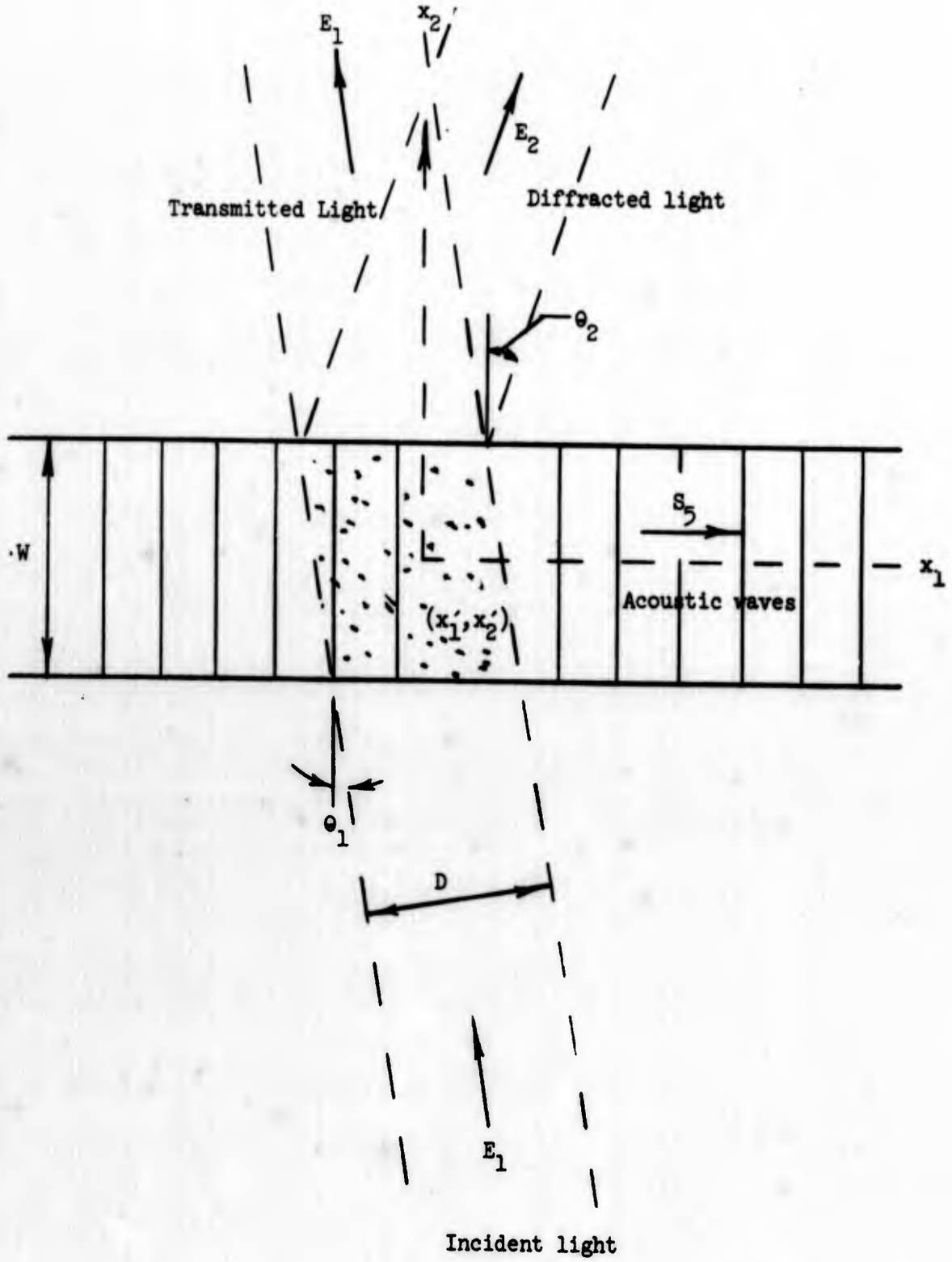

FIG. 5.2--Shear wave diffraction in anisotropic media.

where $k_s = (2\pi/v_s)f_0$, and Δk_s indicates the change in k_s as the acoustic frequency is varied from the center frequency f_0 by an amount Δf . The incident light with the electric field E_1 polarized in the $x_1 - x_2$ plane is incident at an angle θ_1 with respect to the acoustic wave front. Omitting the $e^{jw_1 t}$ term, E_1 can be written as

$$E_1 = A_1 e^{+jk_1 \sin\theta_1 x_1 - jk_1 \cos\theta_1 x_2} , \qquad (5.12)$$

where A_1 is the amplitude of E_1 , $k_1 = (2\pi/\lambda)n^o$ is the wave vector for the ordinary wave in the crystal. Under the small diffraction assumption as discussed in Chapter III, the dipole source for the diffracted light is determined by the product of the incident field E_1 and the change in the dielectric constant by the acoustic waves via the photoelastic effect.

The induced dipole for the diffracted light in this case can be determined geometrically similar to that shown in Fig. 3.2. Due to the natural birefringence of sapphire, the index of refraction of the unstrained crystal seen by the incident light is an ellipse as shown in Fig. 5.3a. The direction of the induced dipole D_1 in the crystal is shown parallel to the ordinary incident light field E_1 . The applied sinusoidal function of shear waves at frequency W_s oscillates the ellipse of the index of refraction seen by the incident light as shown in Fig. 5.3b. A cross polarized dipole D_2 is then produced by the shear waves; D_2 is the dipole source for the extraordinary diffracted light. Because of the natural birefringence in sapphire, the wave vectors of the diffracted and incident light are required to satisfy an extra phase matching condition as illustrated in Fig. 5.1b. The calculation for the change in the dielectric constant due to the shear wave component S_5 is identical to the isotropic case. It is found that

$$\Delta\epsilon_5 = - \epsilon_1 \epsilon_3 p_{55} S_5 .$$

The magnitude of the dipole source at a point (x_1', x_2') within the source region, which is the intersection of the acoustic beam and the incident

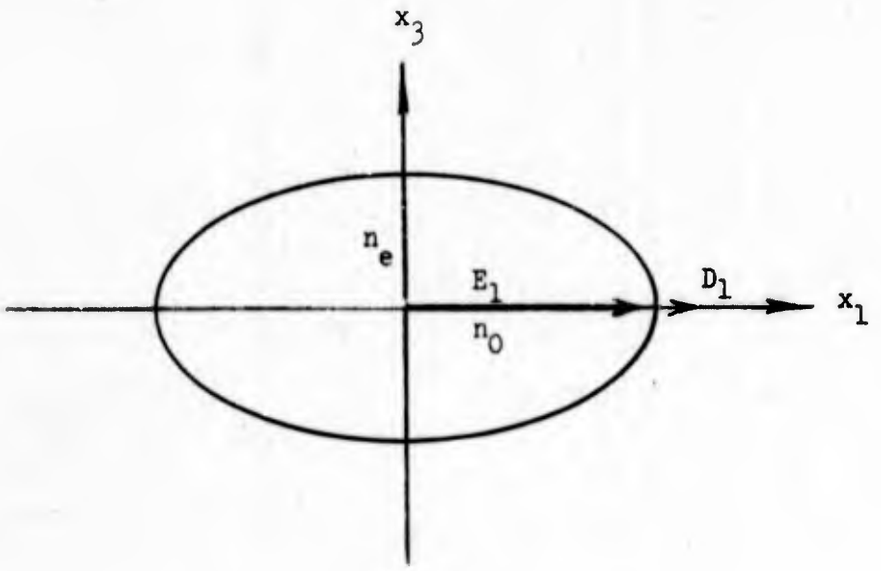

(a) Unstrained uniaxial crystal.

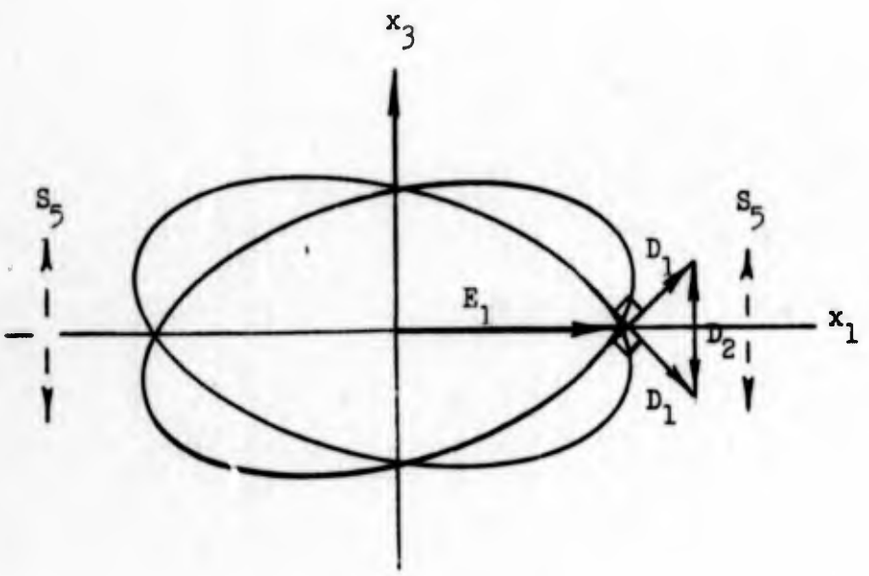

(b) Strained uniaxial crystal.

FIG. 5.3--Induced dipole D_2 in an uniaxial crystal by S_5 .

light beam, can thus be written as

$$dA_2 = -\epsilon_1\epsilon_3\, p_{55}\, S_0\, e^{-j(k_s+\Delta k_s)x_1' + jk_1 \sin\theta_1 x_1' - jk_1 \cos\theta_1 x'_2} \quad . \tag{5.13}$$

In the far field region, the total field of the diffracted E_2 , which is now polarized normal to the incident plane, can be calculated by integrating over the source region:

$$E_2 \int_{-\frac{D}{2\cos\theta_1}}^{\frac{D}{2\cos\theta_1}} dx_1' \int_{-\frac{w}{2}}^{\frac{w}{2}} dx_2'\, dA_2(x_1', x_2')\, e^{-jk_2 \sin\theta_2(x_1-x_1')-jk_s \cos\theta_2(x_2-x_2')} \tag{5.14}$$

where $k_2 = (2\pi/\lambda)n_e$ is the wave vector for the extraordinary wave. Substituting (5.13) into (5.14) yields

$$E_2 = \epsilon_1\epsilon_3\, p_{55}\, S_1 A_1 \left[\int_{-\frac{D}{2\cos\theta_1}}^{\frac{D}{2\cos\theta_1}} dx_1' \int_{-\frac{w}{2}}^{\frac{w}{2}} dx_2'\, e^{-j(k_s+\Delta k_s-k_1 \sin\theta_1-k_2 \sin\theta_2)x_1'} e^{-j(k_1 \cos\theta_1 - k_2 \cos\theta_2)x_2'} \right] e^{-jk_2 \sin\theta_2 x_1 - jk_2 \cos\theta_2 x_2} \quad . \tag{5.15}$$

Let

$$k_s + \Delta k_s - k_1 \sin\theta_1 - k_2 \sin\theta_2 = \Delta k \sin\theta_2 \tag{5.16}$$

$$k_1 \cos\theta_1 - k_2 \cos\theta_2 = \Delta k \cos\theta_2 \tag{5.17}$$

in Eq. (5.15) and we have

$$E_2 = A_{20} LW \frac{\sin(\Delta k \sin\theta_2 \frac{D}{2\cos\theta_1})}{\Delta k \sin\theta_2 \frac{D}{2\cos\theta_1}} \quad \frac{\sin(\Delta k \cos\theta_2 \frac{W}{2})}{\Delta k \cos\theta_2 \frac{W}{2}}$$

$$e^{-jk_2 \sin\theta_2 x_1 - jk_2 \cos\theta_2 x_2} , \qquad (5.18)$$

where $A_{20} = \epsilon_1 \epsilon_3 p_{55} S_0 \ A_1$ is the maximum amplitude when the phase condition is exactly matched at center frequency f_0 , i.e., $\Delta k_s = 0$ and so $\Delta k = 0$. It should be noted that Eq. (5.18) is similar to Eq. (3.27a). The spot diameter of the diffracted beam is determined by

$$\frac{\sin(\Delta k \sin\theta_2 \frac{D}{2\cos\theta_1})}{\Delta k \sin\theta_2 \frac{D}{2\cos\theta_1}}$$

and the bandwidth of the diffracted beam is determined by

$$\frac{\sin(\Delta k \cos\theta_2 \frac{W}{2})}{\Delta k \cos\theta_2 \frac{W}{2}}$$

where Δk is given by Eqs. (5.16) and (5.17) and has a geometrical representation as shown in Fig. 5.4. The bandwidth of the diffracted light can be calculated from this geometrical representation. From Fig. 5.4 at the center frequency f_0 , we have

$$k_s = k_2 \tan\theta_1 \quad . \qquad (5.19)$$

As the acoustic frequency increases to $f_0 + \Delta f$, k_s goes to $k_s + \Delta k_s$

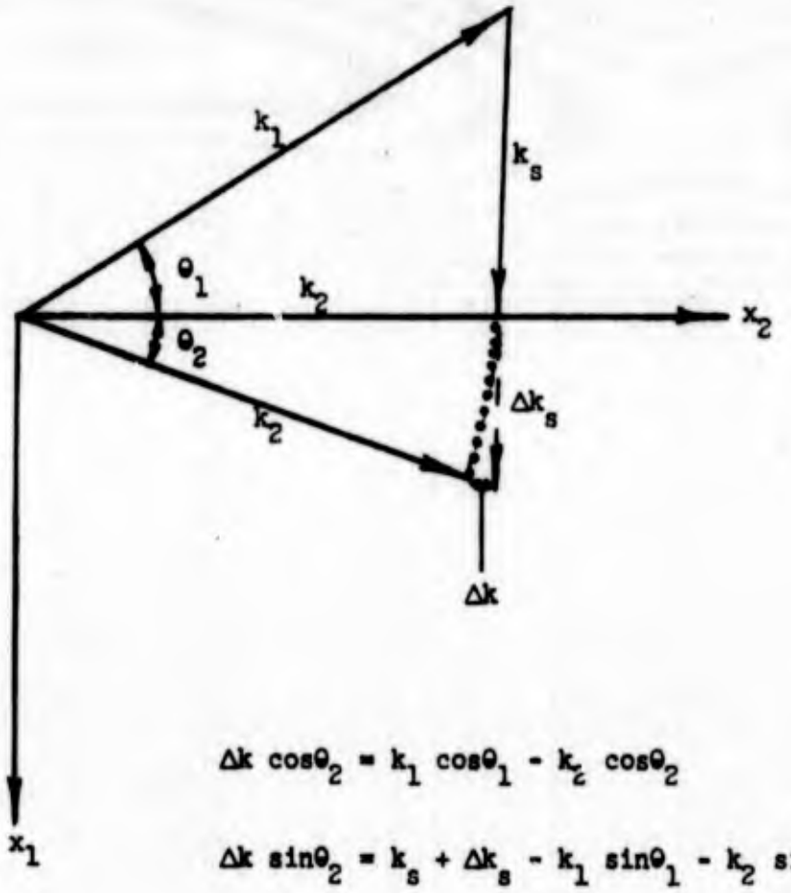

$$\Delta k \cos\theta_2 = k_1 \cos\theta_1 - k_2 \cos\theta_2$$

$$\Delta k \sin\theta_2 = k_s + \Delta k_s - k_1 \sin\theta_1 - k_2 \sin\theta_2$$

FIG. 5.4--Geometrical representation of Eqs. (5.16) and (5.17).

where

$$\Delta k_s^2 = (k_2 + \Delta k)^2 - k_2^2$$

$$\approx 2k_2\Delta k \quad , \tag{5.20}$$

since usually $k_2 \gg \Delta k$. From Eqs. (5.20) and (5.19) we have

$$\Delta k = \frac{\Delta k_s^2}{2k_s} \tan \theta_1$$

$$= \frac{k_s \tan \theta_1}{2} \left(\frac{\Delta k_s}{k_s}\right)^2 \quad . \tag{5.21}$$

Using $\Delta k_s/k_s = \Delta f/f_0$ and Eq. (5.19), Eq. (5.21) can be written as

$$\Delta k = \frac{k_2 \tan^2 \theta_1}{2} \left(\frac{\Delta f}{f_0}\right)^2 \quad . \tag{5.22}$$

In terms of index of refraction and birefringence of the crystal B , we have

$$\tan \theta_1 \simeq \sqrt{\frac{2B}{n_0}} \quad . \tag{5.23}$$

Equation (5.22) can finally be expressed as

$$\Delta k = \frac{2\pi}{2\lambda_0} \frac{n_e B}{n_0} \left(\frac{\Delta f}{f_0}\right)^2 \quad . \tag{5.24}$$

$$\simeq \frac{2\pi B}{\lambda_0} \left(\frac{\Delta f}{f_0}\right)^2$$

From the far field diffraction pattern as shown in (5.18), it is known that the bandwidth of the diffracted light at the -4 dB point is determined by the condition

$$\Delta k \cos \theta_2 \frac{W}{2} = \frac{\pi}{2} \quad . \tag{5.25}$$

From Eqs. (5.24) and (5.25), we obtain the bandwidth of the system as

$$\frac{2\Delta f}{f_0} = 2 \left(\frac{\lambda_0}{2 w B} \right)^{1/2} \quad . \tag{5.26}$$

Substituting $f_0 = (v_s/\lambda_0)\sqrt{2n_0 B}$ from (5.10) into (5.26) we find that

$$2\Delta f \simeq 2 v_s \sqrt{\frac{n_0}{W\lambda_0}} \quad . \tag{5.27}$$

It is noted that the total amount of frequency change Δf is independent of f_0 and is inversely proportional to $\sqrt{W\lambda_0}$. The improvement in the bandwidth for the anisotropic system over that for the isotropic system can be realized by taking the ratio of Eqs. (5.27) and (5.9). Assuming the same acoustic beam width W for both systems, the ratio of bandwidth, becomes approximately

$$\frac{(\text{Bandwidth})_{\text{anisotropic}}}{(\text{Bandwidth})_{\text{isotropic}}} = 2\sqrt{\frac{W \lambda_0}{n_0 \Lambda^2}} \quad . \tag{5.28}$$

For a 1.75 mm wide acoustic beam in sapphire, the bandwidth of scanning a Ne-He gas laser ($\lambda_0 = 6328$ Å) has been improved by a factor of 12.

In the next section we will demonstrate experimentally this scheme in a standard Bragg diffraction cell[3] with shear waves in sapphire and a Ne-He laser as a source of light.

5.2.3 Experimental Results of Continuous Laser Beam Scanning[60]

We have demonstrated the system of continuous deflection of laser beams in a standard Bragg diffraction cell as discussed in Section 4.2 with shear waves in sapphire and a Ne-He laser as a source of light. Sapphire is a negative uniaxial crystal with $n^o = 1.765$ and birefringence $B = 0.008$. The shear waves travel along the x_1-axis of the crystal with a velocity of $5.85 - 10^5$ cm/sec which is the characteristic velocity of the slow shear wave.[61] The light ray was normal to the optic axis with the input wave as the ordinary wave $(k_1 = n_o k_o)$ and the output as the extraordinary wave $(k_2 = n_e k_o)$. The center frequency f_o of the shear waves as given in Eq. (5.10) is 1.56 Gc for sapphire. The angle external to the crystal of the input wave, as given in Eq. (5.19), can be approximated to be $\theta_x = n^o \theta_1 = \sqrt{2n^o B}$; for sapphire $\theta_x = 9.66^o$. The output angle external to the crystal of the diffracted beam at f_o is also θ_x with respect to the transmitted beam. The change in output angle $\Delta\theta_2$ with respect to the change in frequency Δf can be found from the relation that $\Delta k_s = k_2 \Delta\theta_2$ and

$$\frac{n_e \Delta\theta_2}{\Delta f} = \frac{\lambda_o}{v_s} = 1.06 \times 10^{-4} \text{ rod/Mc}$$

in sapphire. The experimental results are shown in Fig. 5.5 where we have plotted (a) the change in angle of the diffracted beam versus acoustic frequency with all other parameters held constant, and (b) the relative intensity of the deflected beam.

The measure value of $n_e \Delta\theta_2/\Delta f$ is 1.07×10^{-4} rod/Mc. The ratio of I/I_{max} is the intensity of the deflected beam relative to the maximum intensity obtained by adjusting the angle of incidence for the input light. The actual intensity of the deflected light did decrease with an increase in acoustic frequency, but this was a result of the decrease in sound intensity at the higher frequencies. The plot in Fig. 2 gives a measure of the scattering efficiency for a constant value of sound power. The ratio of the deflected light intensity to the intensity of the incident beam can be calculated from Eq. (5.18). It depends on the material constants and upon the value of p_{55}; p_{55} in sapphire has been measured to be 0.05.

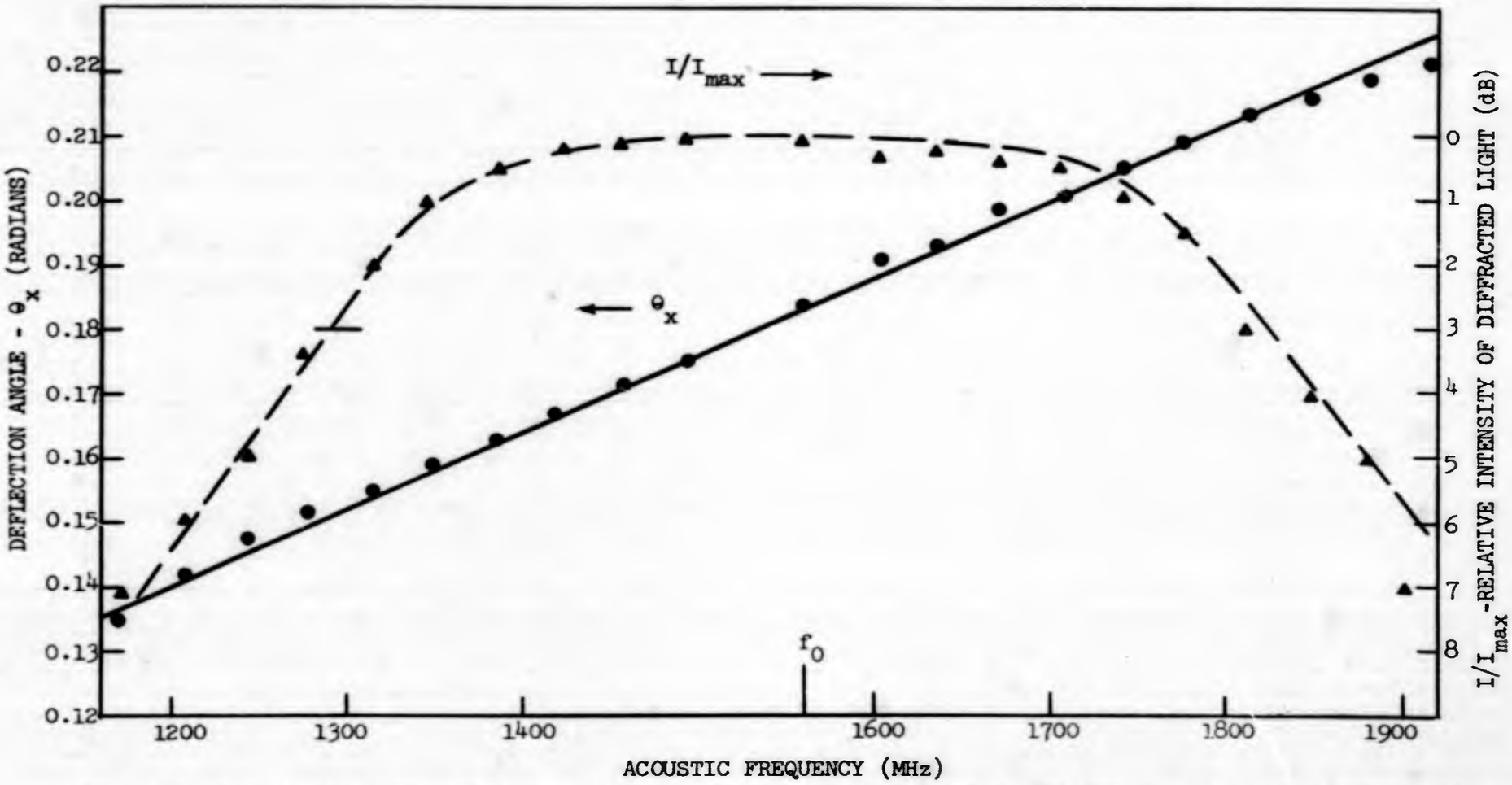

FIG. 5.5--Results for beam deflection in x-cut sapphire. The angle of deflection (θ_x) vs frequencies. The relative intensity of the diffracted beam (I/I_{max}) vs frequencies.

The bandwidth of the system can be estimated from Eq. (5.26). With a beam diameter $W = 1.75$ mm , which was measured by the optical probing technique as discussed in Section 4.4, we have

$$\frac{2\Delta f}{f_0} \simeq 0.4$$

and $2\Delta f = 625$ Mc which is slightly larger than the value shown in Fig. 5.5. The measured value for the bandwidth is 550 Mc about the center frequency $f_0 = 1.56$ Gc. There we see that the acoustic frequency can be varied by ±275 Mc without appreciable degradation of the diffracted light intensity. The value of N can now be calculated. Assuming that we can tolerate an acoustic attenuation of 3 dB across the light beam diameter D , D can be 1.2 cm since the attenuation in sapphire at 1600 Mc (room temperature) is approximately 2.5 dB/cm. From this we have $\tau = 2.1$ μsec and it follows from (5.8) that $N = 1150$.

The ratio of $2\Delta f/f_0$ can approach 0.5 or even more by reducing the acoustic beam width W . The bandwidth $2\Delta f$ can be greatly increased if one can find a material with a high acoustic center frequency f_0 . Ignoring the limitation in the bandwidth of acoustic transducers, and assuming that $2\Delta f = f_0/2$ and that the acoustic attenuation is 3 dB in a distance equal to the diameter of the optical beams, we would like to consider the requirements for a material that would allow one to scan through 10^4 spot diameters.

The constants for $LiNbO_3$ have been measured with $n^o = 2.286$, $B = .086$, and $v_s \approx 3.6 \times 10^5$ cm/sec .[62] The value of f_0 is 3.6 Gc and therefore $\Delta f = 1.8$ Gc . We require a τ of 5.5 μsec, a length of 1.8 cm and a loss 0.55 dB/μsec which is obtainable in $LiNbO_3$ at 77°K.[63] If we tilt the plane of the optical beams so that B is reduced to a value of 6.6×10^{-3} we find that $f_0 = 1$ Gc . The acoustic loss at room temperature is 0.3 dB/μsec and the value of τ for 3 dB total loss is 10 μsec. The crystal length would be 3.6 cm and the system would deflect the beam through 5000 spot diameters.

One of the disadvantages in the acousto-optical deflection devices is that the intensity in the deflected beam is rather weak. For example,

the c-factor of sapphire, which is defined as the ratio of the intensities of the deflected and the incident lights for 1 milliwatt acoustic power in the crystal, is -55 dB. By increasing the acoustic power in the crystal to 1 watt, the intensity of the diffracted light becomes -25 dB below the incident beam. For some practical application, this value may be acceptable. Another practical difficulty is the electronically tunable high Q circuit to drive the transducer, which remains to be solved.

5.2.4 Two-Dimensional Deflection of Laser Beams

A schematic diagram of a two-dimensional beam deflector is shown in Fig. 5.6. Since the bandwidth Δf is determined only by the width of the acoustic column that the light beam travels, the acoustic wave in the y-deflector can be a thin sheet which is wide along the x-direction to collect the deflected spots from the x-deflector. Figure 5.7 shows the relations of k_2, k_{s2} and k_3 in the y-deflectors. The k_2, which is the wave vector of the deflected light in the x-deflector, is the incident wave vector for the y-deflector and is scanning along the z-axis of the y-deflector crystal. The k_{s2} is the acoustic wave vector propagating along the y-axis of the y-deflector crystal as shown in Fig. 5.7. The k_3 is the wave vector of the deflected light in the y-deflector. The resolvable spots for this two-dimensional deflector is

$$N = (\Delta f \, \tau)^2 \quad ,$$

where Δf is the bandwidth and τ is the transit time that the acoustic wave travels across the light beam. Using sapphire as a deflector N is in the order of 10^6 and $\tau = 2$ μsec. Although the resolvable spots N and the transit time τ are quite attractive, yet the intensity of the diffracted light is the major limitation for practical applications.

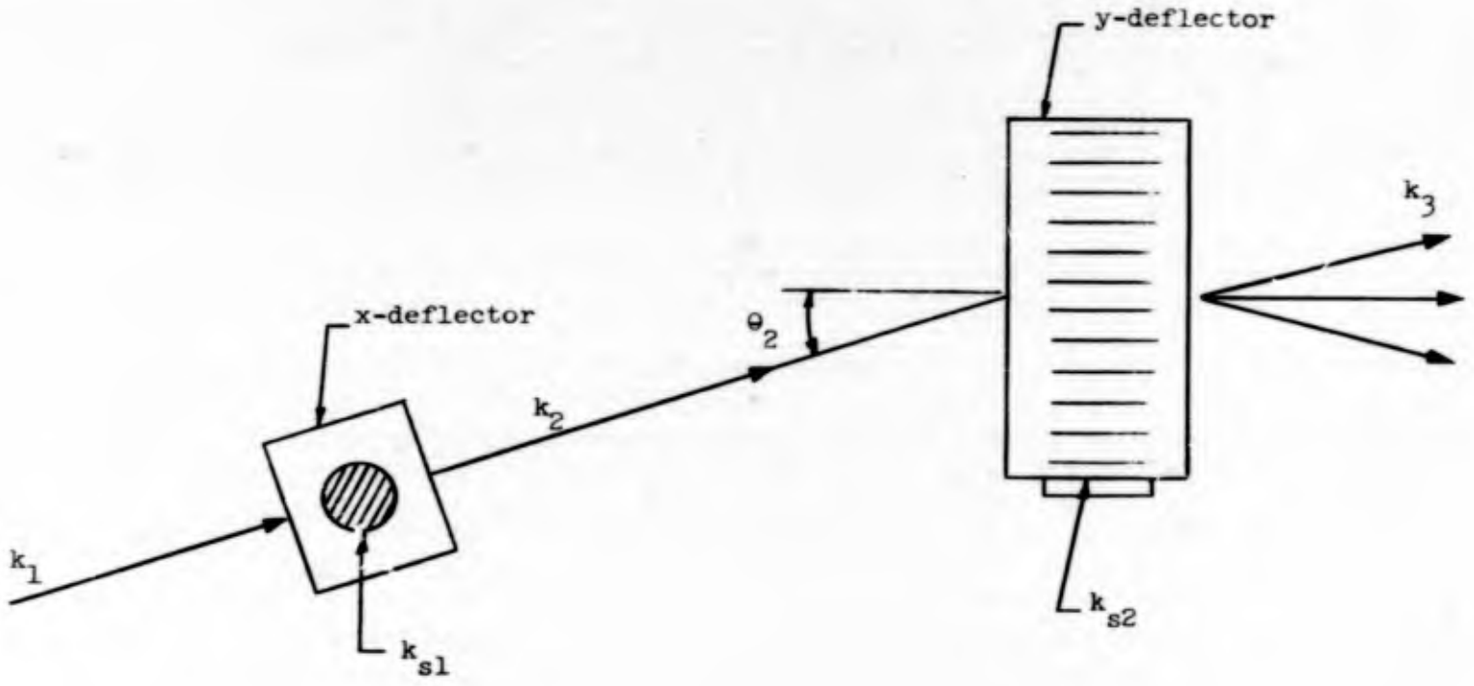

FIG. 5.6--Schematic diagram of two-dimensional deflector.

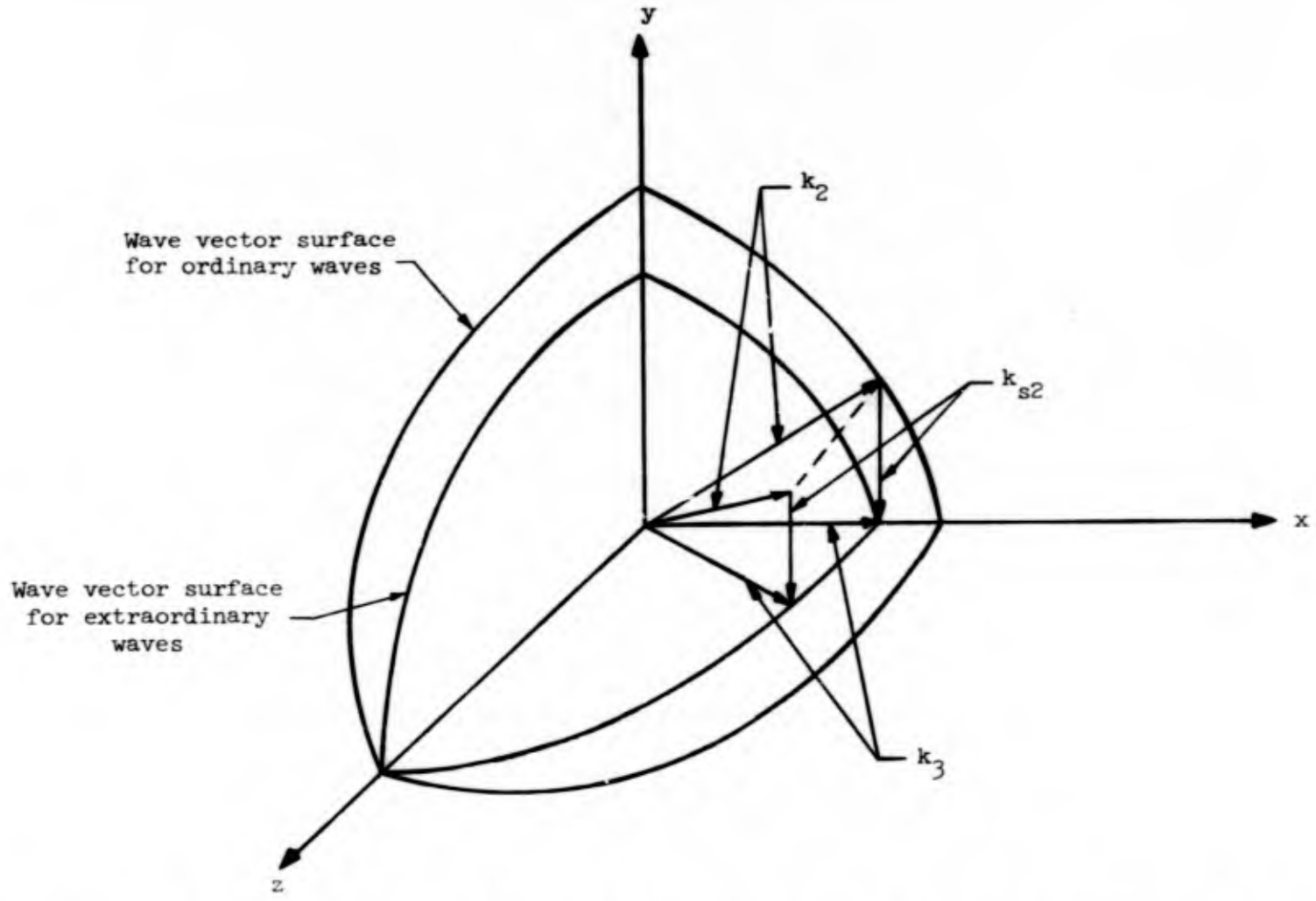

FIG. 5.7--The wave vector surfaces and the relation of k_2 , k_{s2} and k_3 in a negative uniaxial crystal.

CHAPTER VI

CONCLUSIONS

In this study the theoretical and experimental investigations of microwave shear waves in solids have been described.

The difficulty of generating efficient shear waves at microwave frequencies, which was one of the reasons that shear waves have not been extensively utilized in microwave acoustic devices in spite of their potentials, has been overcome. The generation and propagation of microwave acoustic waves in $LiNbO_3$ crystals, where the large piezoelectric effect has to be included, have been studied theoretically. The directions of particle displacements, the velocities and the electromechanical coupling constants for each of their propagating modes have been derived. Experimental measurements of the velocities and the coupling constants on single surface excitations in $LiNbO_3$ rods and on thin disk transducers bonded on delay media have been carried out. The measured values were in good agreement with the calculated values based on published constants. A scheme of efficient microwave shear wave generation by mode conversion, through which virtually the full efficiency available for longitudinal wave generation can be applied to shear waves, has been discussed.

Because of the ability to generate efficient microwave shear waves in solids, the experiments of Bragg diffraction of light from these waves have been successfully accomplished. The unique characteristics predicted by shear wave diffraction theory have been utilized to improve the optical probing techniques of acoustic waves in solids. The experimental results of acoustic beam mapping determined the acoustic energy profile and helped identify the type of acoustic waves generated in the surface of a $LiNbO_3$ rod by normal or tangential electric fields.

The mode conversion efficiency of the YAG mode converter was measured by a laser probe. In addition, Bragg diffraction of light by shear waves has been used to observe directly the acoustic birefringence in a [110] YAG rod. The techniques for experimentally determining the orientation and ellipticity of shear waves generated from an experimental transducer have been demonstrated.

Finally a scheme of continuous laser beam deflection based on Bragg diffraction by shear waves in optically anisotropic media has been described. The experimental demonstration of the continuous deflection of a laser beam through an angle of 4^{o} by tuning only the frequencies of a finite shear wave column in sapphire has shown the possibility for high speed and high resolution optical deflection devices. The improvement of the bandwidth capacity of the anisotropic devices over the corresponding isotropic devices has been shown to be greater than two orders of magnitude. The possible schemes for two dimensional beam deflection have also been included.

APPENDIX

CALCULATIONS ON SHEAR WAVE BONDS

Using the transmission line model as shown in Fig. 4.6, we have derived the expressions for the reflection and transmission coefficients of shear wave bonds between delay media. The calculations are as follows.

The acoustic load rod is represented by a resistor Z_L corresponding to its characteristic acoustic impedance for shear waves. The bond film itself becomes a lossy transmission with (complex) electrical angle θ and characteristic impedance Z_0 .

In the most general case, these shunt impedances are allowed to be parallel combinations of capacitive, inductive, and resistive elements. Also the resistive elements are allowed to be frequency-dependent through a simple power law,

$$R(\omega) = R_0 \left(\frac{\omega}{\omega_0}\right)^{\gamma} \quad .$$

When only the magnitudes of the reflection and transmission coefficients are of interest, the impedances Z_1 and Z_2 are taken to be purely resistive.

The transmission line section itself has an electrical thickness

$$\theta = k_s \ell \quad ,$$

where k_s is the acoustic propagation constant in the bond film. We put

$$k_s = \beta - j\alpha \quad .$$

The real part β is given by

$$\beta = \frac{\omega}{v} \quad ,$$

where v is the shear wave velocity. For convenience, the imaginary part α is specified in terms of a Q (at ω_0) and a power law n,

$$\alpha = \left(\frac{\omega}{\omega_0}\right)^n \cdot \frac{\omega_0}{2vQ} \quad .$$

The characteristic impedance of the transmission line is also complex and is given by

$$Z_0 = \frac{k_s C}{\omega} \quad ,$$

where C is the corresponding elastic stiffness constant. The imaginary part of Z_0, which is small in the case of high Q, may vary with ω. The characteristic acoustic impedances Z_s and Z_L are similarly calculated from acoustic parameters C and v for the corresponding acoustic rods. In the rods, α equals 0 so that Z_L and Z_s are real.

The stress reflection and transmission coefficients are now easily found. The reflection coefficient at $z = 0$ for a stress wave incident from the left is

$$\Gamma = \frac{Z_{in} - Z_s}{Z_{in} + Z_s} \quad ,$$

where Z_{in} is found by the usual impedance transformation,

$$Z_{in} = Z_0 \frac{Z_\ell/Z_0 + j \tan \theta}{1 + j(Z_\ell/Z_0) \tan \theta}$$

with Z_0, θ complex, and

$$Z_\ell = \frac{Z_L Z_2}{Z_L + Z_2} .$$

The stress at $z = \ell$ is easily found by transforming from $z = 0$ through the transmission line and is given by

$$T_\ell = T^+ + T^-$$

where

$$T^\pm = \frac{T_{inc}}{2} (1 + \Gamma) \left(1 \mp \frac{Z_0}{Z_{in}}\right) e^{\pm jk_s \ell}$$

and T_{inc} is the value of the stress wave which is incident from the left of $z = 0$, evaluated at $z = 0$. The stress transmission coefficient at $z = \ell$ is

$$\tau = \frac{T_\ell}{T_{inc}} .$$

For the calculation of reflected and transmitted power (neglecting phase), we have

$$P_R = |\Gamma|^2$$

$$P_T = \frac{Z_s}{Z_L} |\tau|^2 \quad ,$$

where P_R represents the fraction of the incident power reflected at $z = 0$; and P_T represents the fraction of the incident power transmitted to the acoustic load rod.

REFERENCES

1. See, for example, W. H. Haydl and C. F. Quate, Microwave Laboratory Report No. 1446, Stanford University (June 1966).
2. C. Kittel, Phys. Rev. 110, 836 (1958); also H. Bömmel and K. Dransfeld, Bull. Am. Phys. Soc. 5, 58 (1960).
3. C. F. Quate, C. D. W. Wilkinson, and D. K. Winslow, Proc. IEEE 53, 1604 (Oct. 1965).
4. John E. May, Jr., "Thickness-Shear Mode $BaTiO_3$ Ceramic Transducers for Delay Lines," IRE Trans. Ultrasonics Eng. 7 (1960).
5. A. W. Warner, "New Piezoelectric Materials," Proc. 19th Annual Frequency Control Symp. (1966), pp. 5-21.
6. L. Brillouin, "Diffusion de la lumiere et des rayons x par un corps transparent homogene," Ann. Phys. (France) 9th ser. 17, 88 (1922).
7. H. B. Huntington, Solid State Physics, F. Seitz and D. Turnbull, eds. (New York, Academic Press, 1958).
8. M. Born and K. Huang, Dynamical Theory of Crystal Lattices (New York, Oxford Press, 1954).
9. C. V. Ramon and N. S. N. Nath, "The Diffraction of Light by Sound Waves of High Frequency, Part II," Proc. Ind. Acad. Sci. 2A, 413 (1935).
10. G. W. Willard, "Criteria for Normal and Abnormal Ultrasonic Light Diffraction Effects," J. Acoust. Soc. Am. 21, 101 (1949).
11. C. F. Quate, H. J. Shaw, C. D. W. Wilkinson, and D. K. Winslow, "Diffraction of Light Waves by Hypersound," presented at the 1964 Electron Research Device Conference, Cornell University, Ithaca, New York; also see reference 3.
12. L. E. Hargrove, R. L. Fork, and M. A. Pollack, Appl. Phys. Letters 5, 4 (1964).
13. A. E. Siegman, C. F. Quate, J. Bjorkholm, and G. Francois, Appl. Phys. Letters 5, 1 (1964).

14. A. Korpel, R. Adler, P. Desmares, and T. M. Smith, IEEE J. Quant. Elect. QE-1, 60 (1965).
15. C. D. W. Wilkinson and D. E. Caddes, J. Acoust. Soc. Am. 40, 498 (1966).
16. D. E. Caddes and C. D. W. Wilkinson, IEEE J. Quant. Electr. QE-2, 330 (1966).
17. R. W. Dixon, IEEE J. Quant. Electr. QE-3, 85 (Feb. 1967).
18. D. E. Caddes, Microwave Laboratory Report No. 1483, Stanford University (Nov. 1966), Appendix D.
19. N. F. Foster, Proc. IEEE 53, 1400 (1965); also,
J. deKlerk and E. F. Kelly, Appl. Phys. Letters 5, 2 (1964); also,
D. K. Winslow and H. J. Shaw, 1966 IEEE Intl. Conv. Record, Part 5, paper 37.1.
20. N. F. Foster, G. A. Rozgonyi, and F. A. Vannatta, "Cadmium Sulphide and Zinc Oxide Thin Film Transducers," Ultrasonics Symposium, Cleveland, Ohio (1966); also,
R. M. Malbon, D. J. Walsh, and D. K. Winslow, Appl. Phys. Letters 10, 9 (Jan. 1967).
21. A. W. Warner and M. Onoe, "Determination of Elastic and Piezoelectric Constants for Crystals in Class (3m)," Ultrasonics Symposium, Cleveland, Ohio (1966). (Constants recently revised. To appear in J. Acoust. Soc. Am.)
22. E. H. Jacobsen, Phonons and Phonon Interactions, Thor A. Bak, Ed., W. A. Benjamin, Inc., 1964), p. 505.
23. W. H. Haydl, K. Blotekjaer, and C. F. Quate, J. Acoust. Soc. Am. 36, 9 (1964).
24. H. E. Bommel and K. Dransfeld, Phys. Rev. 137, 1245 (March 1960).
25. H. F. Tiersten, J. Acous. Soc. Am. 35, 53 (Jan. 1963).
26. Reference 25; also,
W. P. Mason, Physical Acoustics and the Properties of Solids (D. Van Nostrand, New York, 1958).
27. G. E. Peterson, A. A. Ballman, P. V. Lenzo, and P. M. Bridenbaugh, Appl. Phys. Letters 5, 62 (1964).
28. G. D. Boyd, Robert C. Miller, K. Nassau, W. L. Bond, and A. Savage, Appl. Phys. Letters 5, 234 (December 1964).
29. E. G. Spencer, P. V. Lenzo, and K. Nassau, Appl. Phys. Letters 7, 67-69 (August 1965).

30. Benson Carlin, Ultrasonics (McGraw-Hill, Second Ed., 1960), pp. 259-569.

31. H. Y. Yee, Microwave Laboratory Report No. 1065, Stanford University (July 1963); also,
A. Okaya, "The Rutile Microwave Resonators," Proc. IRE 48, 1921 (Nov. 1960).

32. See, for example, R. Nava, R. Azrt, I. Ciccarello, and K. Dransfeld, Phys. Rev. A134, 581-589 (1964).

33. The Measured Q of the $LiNbO_3$ dielectric resonator is about 3000.

34. D. E. Caddes, Microwave Laboratory Report No. 1483, Stanford University (Nov. 1966). A summary of elastic and photoelastic properties of crystal relevant to microwave acoustic studies is given on pages 59-75.

35. F. E. Terman, Electronics and Radio Engineering (McGraw-Hill, 4th ed.), Fig. 3-11, p. 64.

36. W. P. Mason, Physical Acoustic and the Properties of Solids (D. Van Nostrand Co., Inc., 1958), p. 25.

37. D. L. Arenberg, J. Acoust. Soc. Am. 20, 1 (1948).

38. E. G. Spencer, R. T. Denton, T. B. Bateman, W. B. Snow, and L. G. Van Uitert, J. Appl. Phys. 34, 3059 (1963).

39. M. G. Cohen and E. I. Gordon, Bell System. Tech. J. 44, 693 (1965).

40. G. Benedek, J. B. Lastovka, K. Fritsch, and T. Greytak, J. Opt. Soc. Am. 54, 1284 (1964); also
D. H. Rank, E. M. Kiess, U. Fink, and T. A. Wiggins, J. Opt. Soc. Am. 55, 925 (1965).

41. A. J. DeMaria and R. Gagoz, Proc. IRE 50, 152 (1962); also,
A. E. Siegman, C. F. Quate, J. Bjorkholm, and G. Francois, Appl. Phys. Letters 5, 1 (1964); also,
A. Korpel, R. Adler, P. Desmares, and T. M. Smith, IEEE J. Quant. Electr. QE-1, 60 (1965).

42. See, for example, references 3, 39, and 34.

43. E. G. H. Lean and H. J. Shaw, Appl. Phys. Letters 9, 372 (Nov. 1966).

44. J. F. Nye, Physical Properties of Crystals (Oxford University Press, London, 1957), Section 2.6.

45. J. C. Slater, "Interaction of Waves in Crystals," Rev. Mod. Phys. 30, 197 (1958).

46. N. Bloembergen, Nonlinear Optics (Benjamin, New York, 1965).

47. B. A. Auld and D. A. Wilson, "Bragg Scattering of Infrared Radiation from Coherent Spin Waves," Microwave Laboratory Report No. 1472, Stanford University (Sept. 1966).

48. Reference 44, pp. 250.

49. C. D. W. Wilkinson and R. B. Thompson (unpublished).

50. See references 34 and 3; also,
C. S. Tsai, Microwave Laboratory Report No. 1395, Stanford University, (Dec. 1965).

51. H. Van de Vaart and Henry I. Smith, Appl. Phys. Letters 9, 439 (Dec. 1966).

52. R. W. Dixon and E. I. Gordon, "Carrier Frequency Modulation Using Acoustic Waves," presented at the 1966 Conference on Electron Device Research, C.I.T., Pasadena, California.

53. E. G. H. Lean and H. J. Shaw, "Bragg Diffraction by Microwave Transverse Acoustic Waves," presented at Ultrasonic Symposium, Cleveland, Ohio, 1966.

54. B. A. Auld, C. F. Quate, H. J. Shaw, and D. K. Winslow," Acoustic Quarter Wave Plates at Microwave Frequencies," Appl. Phys. Letters 9, (Dec. 1966).

55. H. van de Vaart, and H. I. Smith, Appl. Phys. Letters 9, 439 (1966).

56. I. P. Kaminow and E. H. Turner, Proc. IEEE 54, 1381 (Oct. 1966).

57. E. I. Gordon, Proc. IEEE 54, 1391 (Oct. 1966).

58. V. J. Fowler and J. Schlafer, Proc. IEEE 54, 1437 (1966).

59. A. Korpel, R. Adler, P. Dismaves, and W. Watson, Proc. IEEE 54, 1429 (1966).

60. E. G. H. Lean, C. F. Quate, and H. J. Shaw, Appl. Phys. Letters 10, 48 (1967).

61. J. B. Wachtman, Jr., W. E. Tefft, D. G. Lam, Jr., and R. P. Stinchfield, J. Res. Natl. Bur. Std. 64A, 213 (1960).

62. R. C. Miller and A. Savage, Appl. Phys. Letters 9, 169 (1966); also, E. G. Spencer, P. V. Lenzo, and K. Nassau, Appl. Phys. Letters 7, 67 (1965).

63. M. I. Grace, R. W. Kedzie, M. Kestigian, and A. B. Smith, Appl. Phys. Letters 9, 155 (1966).

UNCLASSIFIED
Security Classification

DOCUMENT CONTROL DATA - R & D

(Security classification of title, body of abstract and indexing annotation must be entered when the overall report is classified)

1. ORIGINATING ACTIVITY (Corporate author)	2a. REPORT SECURITY CLASSIFICATION
Stanford University Microwave Laboratory Stanford, California 94305	UNCLASSIFIED
	2b. GROUP

3. REPORT TITLE

STUDIES OF MICROWAVE SHEAR WAVES IN SOLIDS

4. DESCRIPTIVE NOTES (Type of report and inclusive dates)

Scientific Interim

5. AUTHOR(S) (First name, middle initial, last name)

E G H Lean

6. REPORT DATE	7a. TOTAL NO. OF PAGES	7b. NO. OF REFS
May 1967	139	63

8a. CONTRACT OR GRANT NO. AF 49(638)1429	9a. ORIGINATOR'S REPORT NUMBER(S)
b. PROJECT NO. 9768-02	M. L. Report No. 1543
c. 6144501F	9b. OTHER REPORT NO(S) (Any other numbers that may be assigned this report) AFOSR 68-2637
d. 681305	

10. DISTRIBUTION STATEMENT

1. This document has been approved for public release and sale; its distribution is unlimited.

11. SUPPLEMENTARY NOTES	12. SPONSORING MILITARY ACTIVITY
TECH, OTHER	AF Office of Scientific Research (SREE) 1400 Wilson Boulevard Arlington, Virginia 22209

13. ABSTRACT

Due to the slower velocities and the transverse wave nature, microwave shear waves have interesting theoretical properties and important practical application. Theoretical and experimental investigation of microwave shear waves in solids were conducted with emphasis on the efficient generation of microwave shear waves and on the theory and application of the parametric interaction of microwave shear waves and light. For the generation of efficient microwave shear waves two schemes were used: mode conversion in a YAG converter, and surface excitation from lithium niobate ($LiNbO_3$) rods and thin disk transducers. The typical conversion loss from electromagnetic to acoustic energies for shear waves in an x-cut $LiNbO_3$ disk transducer is 10 dB at 1 GHz. These efficient shear wave transducers make possible the study of the interaction of light and microwave shear waves in solids. In microwave frequencies, the interaction of light and microwave shear waves is in Bragg diffraction region. We have used a laser as an optical probe to map the energy distribution of shear waves, to measure the attenuation, to estimate the mode conversion efficiency of a YAG mode converter, and to determine the reflection and transmission coefficients of shear wave bonds. We have also demonstrated the second feature of shear wave diffraction in measuring quantitatively the acoustic birefringence in a (110) oriented YAG rod. We have demonstrated a scheme of continuous deflection of an optical beam through an angle of 4° by tuning the shear wave frequencies from 1.2 to 1.8 GHz. The system should be capable of resolving 1000 diffracted spots. The possible extension to two-dimensional deflection schemes will also be included.

DD FORM 1 NOV 65 1473

UNCLASSIFIED
Security Classification

14 KEY WORDS	LINK A		LINK B		LINK C	
	ROLE	WT	ROLE	WT	ROLE	WT
Acoustic-Optical						
Laser						
Crystal						
Brillouin Scattering						
Bragg Diffraction						
Shear Waves						